CREEP AND FATIGUE INTERACTION CHARACTERISTICS OF PWA1484

THESIS

Christian J. Pierce, Captain, USAF

AFIT/GMS/ENY/09-M02

DEPARTMENT OF THE AIR FORCE
AIR UNIVERSITY

AIR FORCE INSTITUTE OF TECHNOLOGY

Wright-Patterson Air Force Base, Ohio

The views expressed in this thesis are those of the author and do not reflect the official policy or position of the United States Air Force, Department of Defense, or the U.S. Government.

AFIT/GMS/ENY/09-M02

CREEP AND FATIGUE INTERACTION CHARACTERISTICS OF PWA1484

THESIS

Presented to the Faculty

Department of Aeronautical and Astronautical Engineering

Graduate School of Engineering and Management

Air Force Institute of Technology

Air University

Air Education and Training Command

In Partial Fulfillment of the Requirements for the

Degree of Master of Science (Materials Science)

Christian J. Pierce, BS

Captain, USAF

March 2009

AFIT/GMS/ENY/09-M02

CREEP AND FATIGUE INTERACTION CHARACTERISTICS OF PWA1484

Christian J. Pierce, BS
Captain, USAF

Approved:

_____//signed//_____	_____
Anthony N. Palazotto, PHD (Chairman)	Date
_____//signed//_____	_____
Andrew H. Rosenberger, PHD (Member)	Date
_____//signed//_____	_____
Tommy J. George, PHD (Member)	Date

Abstract

One of the main methods for predicting the service life of jet engine turbine blades is through creep analysis. A sample of the turbine blade material will be mechanically tested to characterize its creep performance. This characterization will be used to determine safe operating conditions for the material. While methods for modeling creep behavior are generally well developed, this constant load creep testing does not fully represent the loading conditions present in a jet engine due to cyclic loading caused by the mission profile and throttle movements. As the industry seeks to become more accurate in physics based modeling of materials that are used in turbine blades, incorporation of these cyclic loads into the characterization of turbine blade materials is needed. It will be important to understand what effect pre-existing creep will have on fatigue life and what effect pre-existing fatigue loading will have on creep life. This research gives microstructural observations as well as data analysis of samples of PWA1484 tested at 871°C in creep-fatigue environment. This research resulted in the conclusion that prior fatigue cycling results in a non-linear reduction in the amount of primary creep, and an earlier transition to tertiary creep in PWA1484.

AFIT/GMS/ENY/09-M02

To my Wife

Acknowledgments

I would like to express my sincere appreciation to Dr. Anthony Palazotto, Dr. Andy Rosenberger, and Dr. Tommy George for their assistance and guidance during my research. Andy, this thesis would not have been possible without the support you provided in everything from teaching me about the test equipment, to your depth of materials science knowledge that pointed me in the right direction many times. I would also like to thank Phil Blosser, Mark Ruddell, and Dave Maxwell from UDRI whose excellent support kept the test equipment operational. I would also like to thank my wife Rebecca for her love and support during the past year and a half. Without her patience and encouragement, this work would not have been possible.

Christian J. Pierce

Table of Contents

Page

Page

List of Figures

Figure Page

Figure Page

List of Tables

CREEP AND FATIGUE INTERACTION CHARACTERISTICS OF PWA1484

I. Introduction

1.1 Background

"Superalloys are high temperature materials which display excellent resistance to mechanical and chemical degradation at temperatures close to their melting points [1]." The objective of this research is to describe through test data and microstructural analysis, the effect that prior fatigue cycling will have on creep behavior and what effect prior creep deformation will have on fatigue behavior of Pratt and Whitney Alloy 1484 (PWA1484). Superalloys were first developed in the 1940's in order to fill the need for parts that could withstand the high temperature operating environment of a gas turbine jet engine [1]. Superalloys are typically used in the high pressure turbine section of a jet engine, located just after the combustion chamber in a jet engine. Figure number 1 is a cut away view of the inside of the F-100 jet engine manufactured by Pratt and Whitney.

The most extreme environment in the jet engine is the location that is just behind the combustors in the engine. This location is annotated on Figure 1 below. This location is one of the hottest areas of the jet engine [1]. The highest temperature that turbine blades will have to withstand is the temperature of the gases that are produced by the combustion in the jet engine and then flow into the turbine section of the engine. The temperature of these gases is called the turbine entry temperature and this temperature is seen by experts as the most extreme environment in the engine. This is the reason that turbine entry temperature is used as a benchmark for what turbine blade material will need to withstand during operation.

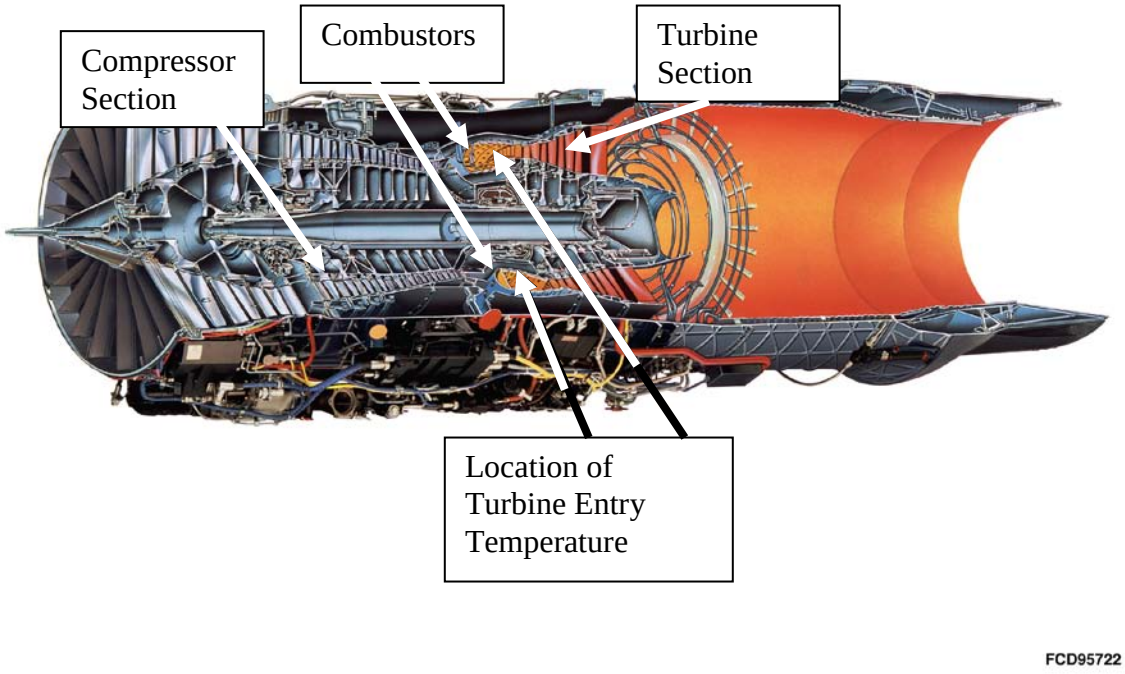

Figure 1: F-100 Jet Engine [16]

Additionally, thermodynamics of a jet engine are such that an engine that operates at a higher turbine entry temperature can operate more efficiently than an engine that operates at a lower turbine entry temperature [1]. The drive for more efficient engines has also increased the demand for superalloys that can withstand these higher temperatures.

The first generation of superalloys were wrought, polycrystalline alloys. In the years following the development of this first generation of superalloys, methods for the casting of turbine blades were introduced which allowed for improvements in the overall temperature and stress resistant qualities of the superalloys. These casting developments included vacuum induction which improved the purity of the alloys and the development

of casting techniques of directional solidification that allow all of the grain boundaries in the superalloy to form in a single direction [1]. This directional solidification allowed further improvements in the high temperature creep life of these superalloys because there were no grain boundaries that were oriented perpendicular to the direction of loading [1].

The final step forward in casting technology that brings us to the present day techniques was the ability to cast turbine blades that are single crystals. A single crystal turbine blade is one in which there are no grain boundaries present. This is achieved by suppressing any columnar grains that are not growing in the desired direction and only allowing a grain that has been oriented in the proper direction to grow, resulting in a turbine blade that is a single crystal [17]. Growth mentioned in the previous sentence is defined as solidification that results in an increase in size of a grain. To better understand how a single crystal casting is produced, let us talk about how a directionally solidified alloy is produced.

A directionally cast superalloy is produced by producing a large thermal gradient on one side of the casting mold by using a water cooled chill plate and slowly drawing the mold out of the casting furnace. This thermal gradient causes the direction that is normal to the chill plate to be the preferred direction of growth for the grains. Although grains will begin to grow in random directions, the grains growing in the preferred direction will crowd these random grains out [17]. A single crystal casting is made in the same way that a directional casting is made except that a grain selector is added above the chill plate that only allows one grain to grow and results in a single crystal casting [17].

A single crystal nickel based superalloy consists of a gamma matrix in which there are contained gamma prime precipitates. These precipitates and the gamma matrix can be seen in figure number 2 which is an SEM image of a sample of PWA1484.

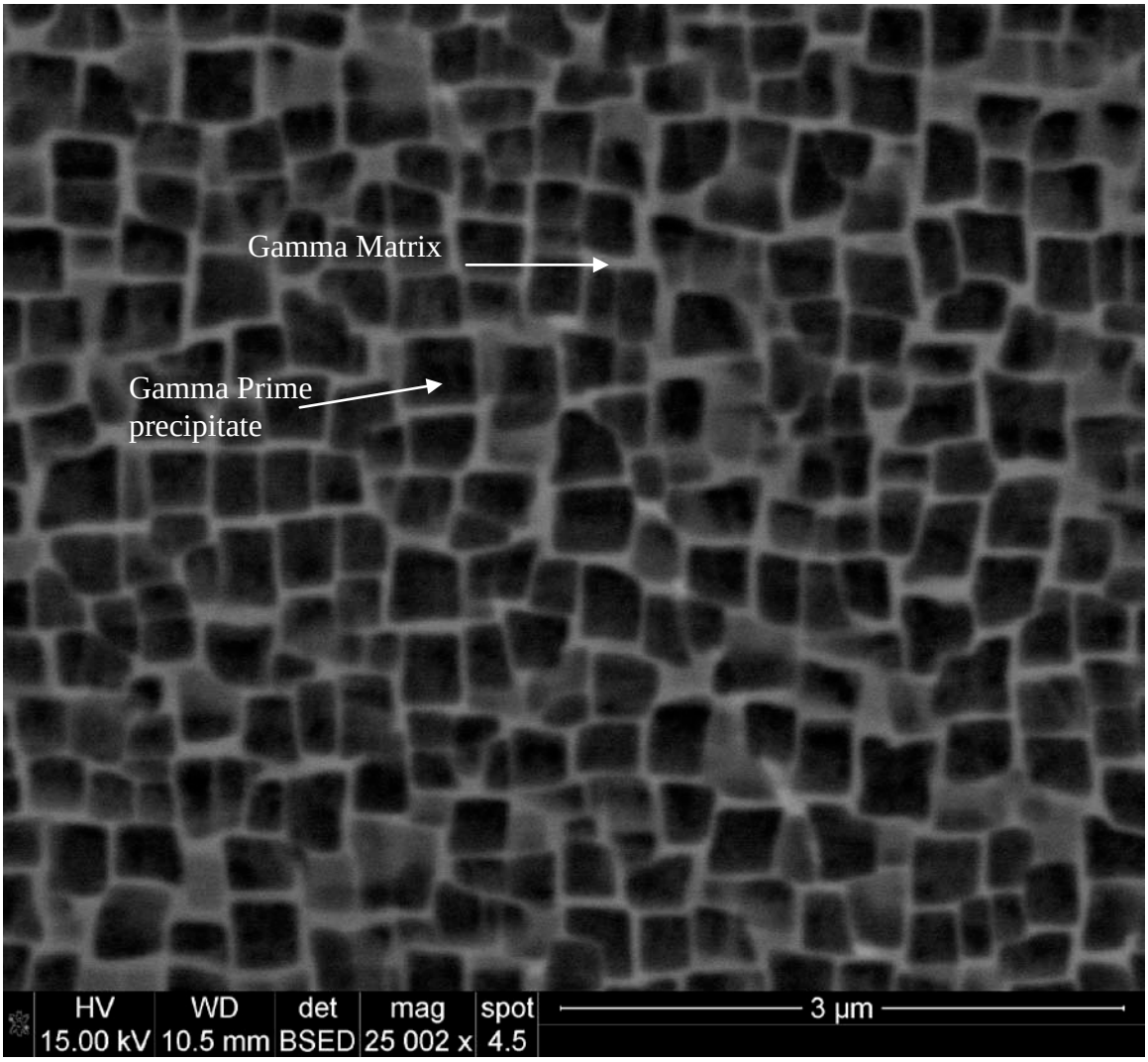

Figure 2: Microstructure of PWA1484

A single crystal turbine blade will not require any grain boundary strengthening materials such as boron and carbon to be added to it. When boron and carbon are not in the material, more extreme heat treatments can be applied that will improve the fatigue life of

the turbine blade [1]. Currently, single crystal turbine blades have been shown to have longer creep rupture lives at higher temperatures than their polycrystalline predecessors. Within the single crystal class of superalloys, there have also been further developments that mainly involved changing the chemical composition of the superalloys in an attempt to achieve even longer creep rupture lives at higher temperatures. The creep properties of a superalloy are important because of the tight tolerances of the inside of a jet engine. A turbine blade made from a material that cannot resist creep will become unusable in an aircraft jet engine and could cause damage to the engine.

Pratt and Whitney Alloy 1484 is a second generation nickel-based, single crystal superalloy that was developed by Pratt and Whitney. PWA1484 has a chemical composition that consists of 5% Cr (chromium), 10% Co (cobalt), 2% Mo (molybdenum), 6% W (Tungsten) , 5.6% Al (aluminum) , 9% Ta (tantalum) , 3% Re (rhenium) , .1% Hf (hafnium) , and 59.3% Ni (nickel) by weight [1]. The alloy was invented by David Duhl and Alan Cetel from Pratt and Whitney in the first half of the 1980's with a patent being filed on 10 June 1985. PWA1484 was the first single crystal superalloy that contained rhenium as one of its alloys [3]. The reason that rhenium was introduced into the superalloy was that it was a refractory material that could enhance the creep performance of the superalloy [3, 15].

1.1.1 Previous Single Crystal Superalloy Research: Creep

There has been a large amount of research done in order to determine the creep properties of single crystal nickel based superalloys [3]. Some of the research involving first generation single crystal superalloys looked at the behavior of the gamma prime

precipitates during creep testing in an attempt to determine the relationship between the morphology of the microstructure of the superalloy and its creep performance. Through examination of past research, it is clear that in order to understand the fatigue and creep behavior of PWA1484; one must understand the behavior of the gamma prime precipitates under the given test conditions. The reason for this is that due to the lack of grain boundaries in PWA1484, evolution of the gamma prime precipitates is one of the driving factor in creep and fatigue performance in the material.

Nathal and Ebert discovered during testing performed in 1983 on NASAIR 100, a first generation single crystal superalloy, that the gamma prime precipitates coarsened into plate type rafts perpendicular to an applied stress when the superalloy was placed under tension as shown in Figure 3 by the dark plates of gamma prime precipitates.

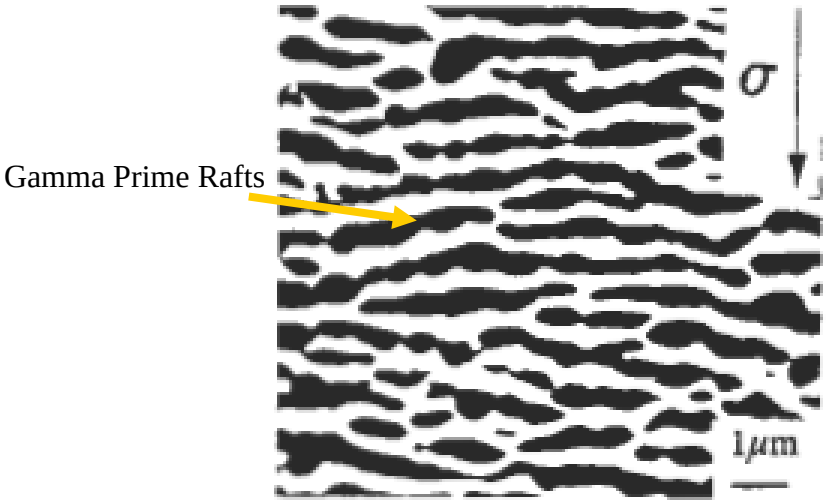

Figure 3: Plate Type Rafts of Black Gamma Prime Precipitates [5]

The same research showed that the gamma prime precipitates formed needle type rafts parallel to an applied stress when the test specimen was placed into compression as illustrated in Figure 4 [4].

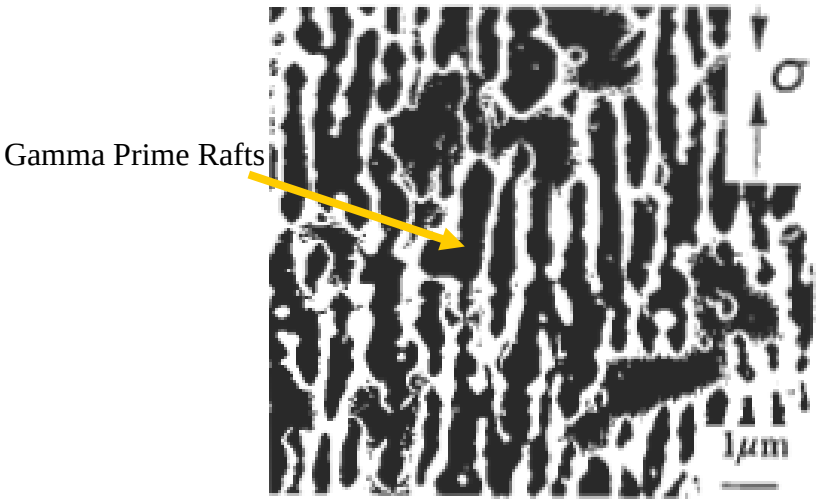

Figure 4: Needle Type Rafts of Gamma Prime Precipitates [5]

Nathal and Ebert's results gave evidence that this rafting of gamma prime precipitates is a general phenomenon of single crystal nickel based superalloys. This evidence was further corroborated by work done by MacKay and Ebert [24].

Work by Hael Mughrabi sought to determine the effect that the rafting behavior of the gamma prime precipitates had on the creep performance of second generation single crystal superalloys [5]. He examined what factors governed the coarsening of the gamma and gamma prime phases of material and stated that the elastic constants of the gamma and gamma prime phases as well as the lattice misfit between the two phases were the most relevant material constants in coarsening [5]. The misfit factor of a superalloy is defined as

$$\delta = \frac{2(a_{\gamma'} - a_{\gamma})}{a_{\gamma'} + a_{\gamma}} \qquad (1)$$

This represents the difference of the gamma prime lattice constant, $a_{\gamma'}$, and the gamma lattice, a_{γ}, constant divided by one half of the sum of the gamma prime lattice constant and the gamma lattice constant. This misfit factor makes use of research done by J. D. Eshelby concerning elastic inclusions and in-homogeneities in 1961 [6]. Mughrabi further states that there is a tensile stress present in the gamma prime phase and a compressive stress present in the gamma phase as a result of a negative lattice misfit between the two phases [5]. He confirmed earlier research and stated that rafting (coarsening) in the gamma prime phase would not occur in random directions but would be perpendicular to a tensile stress and parallel to a compressive stress [5].

Mughrabi states that during deformation of a single crystal superalloy there are dislocations that first move through the softer gamma matrix and will initially go around the harder gamma prime precipitates, and that there will be a buildup of dislocations at the gamma/gamma prime interfaces. Mughrabi found that it is this buildup of interface dislocations that are responsible for higher stresses in the gamma prime precipitates. With these increasing dislocations, there will be a point when the dislocations will not be able to travel around the gamma prime precipitates and there will be dislocations that begin to enter the gamma prime precipitates as illustrated in Figure 5 [5].

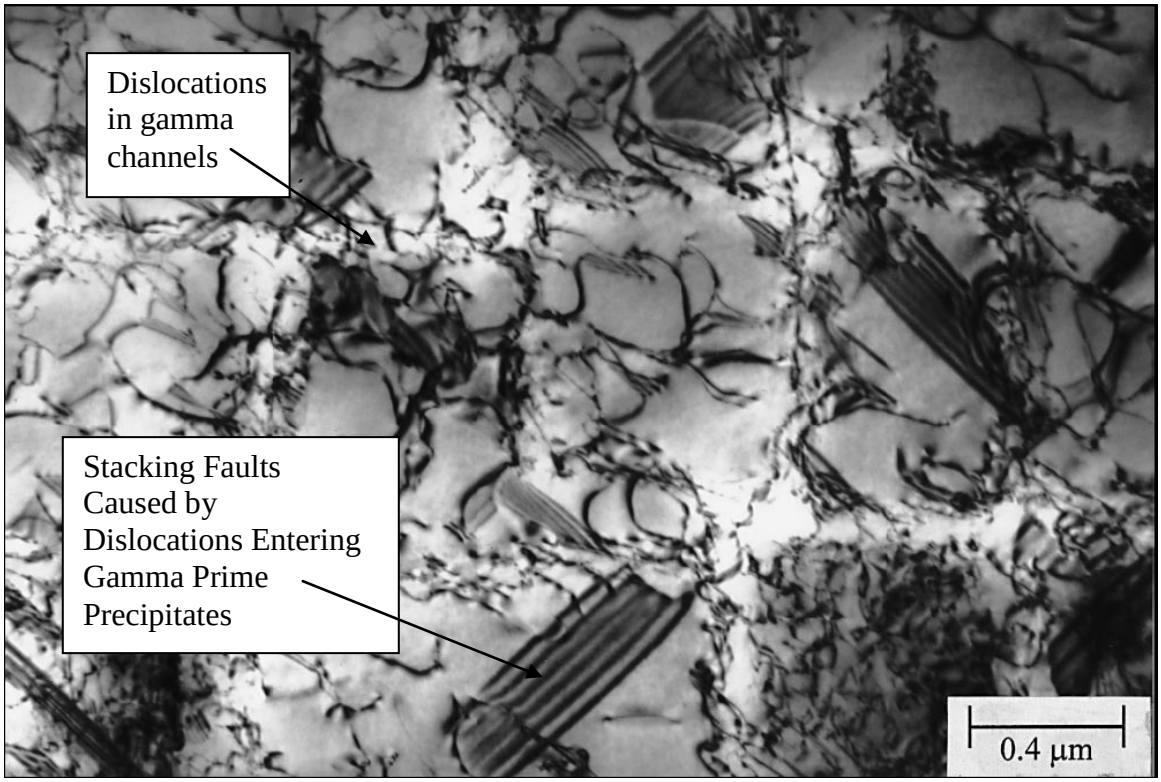

Figure 5: Image of Dislocation Structure During Creep [22]

In Mughrabi's discussion of the effect of rafting on creep performance he finds that in most cases rafting will reduce the creep life of a specimen, but under limited circumstances of high temperature and low stress, creep life would be lengthened by rafting [5]. Mughrabi explained this by stating that dislocations gliding through the gamma channels and climbing over gamma prime precipitates was believed to be the rate controlling process for creep and that for a high temperature and low stress environment, dislocations are able to travel freely around the gamma prime rafts resulting in lower stresses inside the gamma prime precipitates and longer creep life for the specimen [5]. He also examined rafting situations involving negative connectivity meaning that the gamma prime rafts begin to connect with one another, and as a result, islands of gamma

material are surrounded by gamma prime material so that instead of gamma prime islands in a gamma matrix, the relation is inverted. Mughrabi predicted that these situations would result in a large number of trapped interface dislocations and high internal stresses in the gamma prime rafts which would cause a shortened creep life [5]. MacLachlan and Knowles found through their research that at temperatures below 850°C, a single crystal superalloy (CMSX-4) will show a primary stage of creep, but at higher temperatures, the creep would begin almost immediately in a steady state behavior [8].

1.1.2 Previous Single Crystal Superalloy Research: Fatigue

Research has been undertaken to determine the effects of rafting of the gamma prime precipitates on the fatigue behavior of single crystal superalloys [8]. In his examination of the effects of rafting on the fatigue performance of single crystal superalloys, Mughrabi found that gamma prime rafts that were perpendicular to the applied cyclic load caused a reduction in fatigue life and rafts parallel to an applied load caused an increase in fatigue life. He states that rafts parallel to the applied cyclic load act as barriers to crack propagation [5]. The reason for this is that the gamma prime precipitates are harder than the gamma matrix and provide more resistance to crack growth, which is enhanced by a needle type raft that a crack is forced to go around.

Further research by Ott and Mughrabi also validated the statements of Mughrabi. The testing performed by Ott and Mughrabi compared pre-rafted specimens in fatigue to non-rafted specimens in fatigue [9]. This research confirmed that specimens with rafts perpendicular to the stress axis reduced creep life and specimens with rafts parallel to the stress axis increase creep life as compared to specimens without any pre-rafting. Ott and

Mughrabi also observed that crack propagation during fatigue of single crystal superalloys favored the gamma phase and tended to go around the gamma prime phase [9].

One of the most recent mathematical models to explain the fatigue behavior of single crystal nickel based superalloys was proposed by Sakaguchi and Okazaki in 2007 [10]. Sakaguchi and Okazaki included micro structural factors and gamma/gamma prime shape changes in their proposed model. Sakaguchi and Okazaki's model produced results that confirmed the earlier research of Ott and Mughrabi which stated that a single crystal superalloy that has gamma lattice constants that are larger than the gamma prime lattice constants (negative misfit) will have a fatigue life that is shortened when plate type gamma prime rafting is present, and prolonged when needle type gamma prime rafting is present [10].

1.1.3 Creep and Fatigue Interaction Research

Creep fatigue interaction occurs in modern Air Force jet engines due to long missions at high temperatures that contribute to creep damage, and throttle changes that occur during the mission that will cause fatigue cycling of the turbine blades. Wright, Jain, and Cameron examined high cycle fatigue in PWA1484 and determined that there is an interaction of creep and fatigue during fatigue loading at elevated temperatures [12]. Wright and colleagues examined creep and fatigue interaction and found that at high mean stresses ($R>0$) or lower fatigue cycling frequencies, creep rupture was the dominant failure mode. They also determined that at higher frequencies and R values of less than zero, a fatigue failure mode is dominant [12]. Wright, Jain, and Cameron had the greatest

success in modeling their fatigue testing results when they used a linear combination of fatigue and creep damage models [12]. There has also been research done involving steels that sought to quantify creep and fatigue interaction through the use of thermodynamic descriptions of the internal energy of the material [20]. There has not been a large amount of additional research done to determine the creep fatigue interaction behaviors of nickel based single crystal superalloys, specifically PWA1484. This is an area that needs to be looked into especially in the area of high temperature turbine blade applications for PWA1484.

1.2 Problem Statement

"The FAA and DOD are adding damage tolerance to the design, certification, and management requirements for aircraft engine structures. The move to damage tolerance as a complement to traditional safe life is driven by the observation that airfoil cracking often slows down and even stops outside the crack initiation zone especially in highly plastic or crept region. Thus the damage tolerance considerations require development of non-linear crack propagation methodology [25]." A method for predicting the creep and fatigue behavior, including creep-fatigue interaction behavior of PWA1484 is needed as part of the solution to meet these requirements. A model that predicts the creep behavior of PWA1484 currently exists, however, there are still unexplained behaviors resulting from creep and fatigue interaction.

1.3 Research Objectives

The objective of this research is to provide and interpret data on the behavior of PWA1484 in creep-fatigue interaction environments. This data will include test data

acquired during elevated temperature creep and fatigue testing as well as microstructural observations which will be acquired using scanning electron microscopy. This research will seek to provide data to aid in the explanation of how creep affects the fatigue life of PWA1484 and how fatigue affects the creep life. Can creep and fatigue damage be linearly summed or is there a non-linear interaction of these two loading scenarios? How does the microstructure of PWA1484 behave under circumstances of creep-fatigue interaction? This research seeks to establish a foundation of data and observations for creep-fatigue interaction that can be used in future research to develop a model that can accurately describe the behavior of PWA1484 in loading scenarios that consist of both creep and fatigue.

1.4 Research Focus

The research is focused on examining the high temperature creep, fatigue, and creep-fatigue interaction behavior of PWA1484 using experimental data as well as microstructural characterization. Each test will be conducted in load control at a maximum stress of 517MPa and the temperature for each test will be 871°C for each testing scenario. The reason for this test temperature is to remain consistent with previous testing performed by Pratt and Whitney on PWA1484. The test stress level of 517MPa is chosen to minimize primary creep during testing while providing data at an intermediate stress level compared to previous testing conducted by Pratt and Whitney.

1.5 Assumptions/Limitations

This research assumes that the test specimens have been manufactured and machined properly and that these processes did not introduce any flaws or defects into the specimens that would skew test results. A limitation of this research is that we are performing testing in standard atmospheric conditions. These tests are being done in air so the effects of oxidation will be present, but are not being considered during this research.

1.6 Thesis Layout

The following chapters will go step by step through the research performed for this thesis. Chapter two will be a discussion of the theory that describes creep and fatigue including derivations of key equations. The chapter will conclude with a discussion of creep and fatigue interaction and the method that will be used in this research to tie creep and fatigue together. Chapter three is a description of test material and the experimental methods used in this research. Each test that will be conducted will be described as well as the data that will be collected during testing. Chapter four will include the experimental setup used during testing. Test equipment will be described and test equipment calibration and setup will be described. Chapter five will contain test results and data analysis. This chapter will discuss the results of each test and will contain numerical analysis of data and post test microstructural analysis of test specimens. Chapter six will make conclusions about test results and make recommendations for future research involving creep and fatigue interaction of PWA1484.

II. Theory

2.1 Chapter Overview

This chapter will describe fatigue and creep theory separately, and then discuss the possibility of numerical characterization of the interaction of creep and fatigue. The first section of this chapter will discuss a stress based approach to fatigue that will include development of a power law relationship of fatigue cycles to failure. The second section will discuss creep, giving a description of the stages of creep including microstructural behavior with a development of the total strain equation. The final section of this chapter will discuss a creep and fatigue interaction model for Pratt Whitney Alloy 1484 that was proposed in 2004 by P.K. Wright, et al. [12].

2.2 Creep and Fatigue

Two of the main reasons for the failure of turbine blades in a jet engine are excessive creep that causes the turbine blades to be unusable or causes creep rupture of the blades, and fatigue that can also cause cracking and failure of the turbine blades. Since these are the failure modes that will be examined in this research, the following is a discussion of some of the relevant theory that is used in the examination of creep and fatigue data. For this research we will base our mathematical calculations involving creep on the total creep equation derived in "Elastic and Inelastic Stress Analysis" by Shames and Cozzarelli [11]. Additionally, the time temperature Larsen Miller parameter as discussed in "Mechanical Behavior of Materials" by Norman E. Dowling will be considered for estimating creep rupture lives [2]. For fatigue analysis of test data we will use the stress based approach to fatigue discussed by Norman E. Dowling [2]. Creep and

fatigue interaction is an active area of current research, but a linear summation method of creep and fatigue will be attempted using creep and fatigue interaction models as proposed by Wright et al. in “High Cycle Fatigue in a Single Crystal Superalloy: Time Dependence at Elevated Temperature” [12].

2.1.1 Fatigue

Our discussion of the theory considered in this research will begin with fatigue. We have already established that turbine blades endure loading that does not remain constant over their service life. The loading of these components will vary depending on what type of mission is being flown and will also vary during a given mission due to acceleration and deceleration of the aircraft. These circumstances make fatigue behavior of turbine blade material an area that cannot be ignored when evaluating the properties of a material for use in jet engines. Fatigue failure of a material occurs under conditions of variable loading that cause material failure after a given number of cycles of loading [2]. There are several approaches to modeling the fatigue behavior of a material, but our focus will be the explanation of the stress based approach to fatigue life prediction. The reason we will focus on the stress based approach is that the loads for this research will be elastic loads and should not produce significant plastic deformation. The stress based approach to fatigue life prediction allows us to predict the number of cycles to failure for a material based on the stress applied during those cycles. The stress based approach to fatigue life prediction has several terms and definitions that are useful to mention before discussing the method of analysis. The following is a list of these terms.

1. Constant Amplitude Stressing- cycling between maximum and minimum stress levels that remain constant.

2. Stress Range ($\Delta\sigma$) - the difference between the maximum and minimum stress values. $\Delta\sigma = \sigma_{\max} - \sigma_{\min}$

3. Mean Stress (σ_m) - the average of the maximum and minimum stress values.

   $$\sigma_m = \frac{\sigma_{\max} + \sigma_{\min}}{2}$$

4. Stress Amplitude (σ_a) - half of the stress range; the variation of the stress about the mean stress value. $\sigma_a = \frac{\Delta\sigma}{2}$

5. Stress Ratio (R) - $R = \frac{\sigma_{\min}}{\sigma_{\max}}$

6. Amplitude Ratio (A) - $A = \frac{\sigma_a}{\sigma_m}$

7. Completely Reversed Stressing- a term describing a loading condition where $\sigma_m = 0$

8. Zero to Tension Stressing- a loading condition where $\sigma_{\min} = 0$

The above terms will be used in equations and descriptions throughout the rest of this section.

Stress life (S-N) curves consist of data from fatigue testing of a material at a constant cyclic stress. The stress amplitude of the test is plotted versus the cycles to failure (N_f) of the test. This will represent one point of data on the S-N curve. Additional testing at different stress levels are used to complete the S-N curve. Figure number 6 is an example of SN curves at 1038°C from research involving PWA1484 tensile specimens oriented in the <001> plane [12].

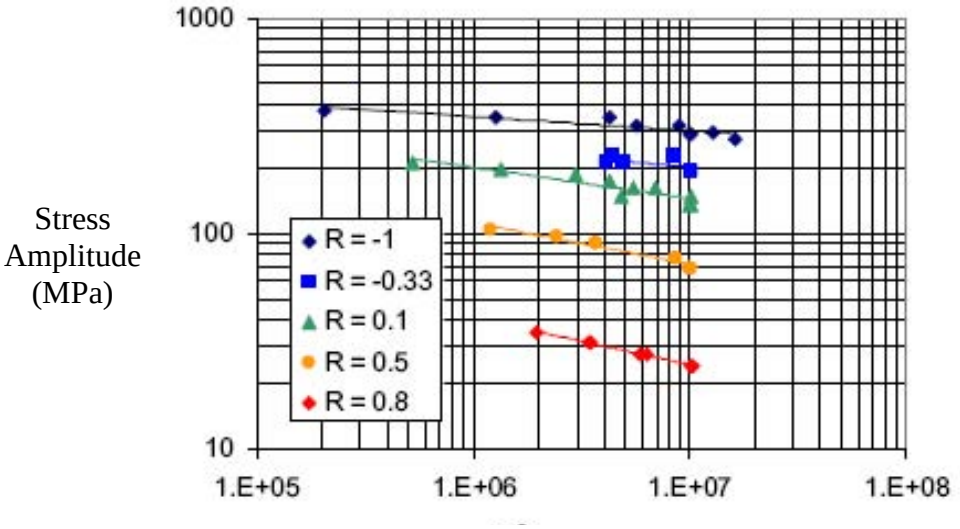

Figure 6: PWA1484 S-N Curves at 1038°C [12]

The stress and cycle data in the S-N curve is usually plotted on a log-log scale as in the figure above. At lower applied stresses, the S-N curves of many materials will flatten out and approach an approximate asymptotic value. Theoretically there will be no fatigue damage that will occur at stresses below this asymptotic value. This stress value is called the fatigue limit of the material. For some types of material such as PWA1484 displayed above, the S-N curve will not flatten out to an asymptotic value and their fatigue limits

are defined as the stress amplitudes that will result in a virtually infinite life of 10^8 cycles. If the data points of the S-N curve form an approximate straight line when they are plotted on a log-log scale, then the data can be modeled using the fitting equation

$$\sigma_a = AN_f^{\ B} \qquad (2)$$

which relates the stress amplitude to the number of cycles to failure, N_f. The fitting constants A and B can be found by performing a least squares regression on the log data or by through algebraic manipulation using two points that are a large distance apart in the S-N data curve. This is accomplished by setting the each stress value from the two points equal to the fitting equation in which N_f will be a known value. This will result in two equations

$$\sigma_1 = AN_1^{\ B} \qquad (3)$$

and

$$\sigma_2 = AN_2^{\ B} \qquad (4)$$

with two unknowns. We can then solve for B by dividing the second equation into the first equation which results in the equation

$$\frac{\sigma_1}{\sigma_2} = (\frac{N_1}{N_2})^B \qquad (5)$$

Through algebraic manipulation we can solve for B and then plug the value for B into either equation for sigma and solve for the value of A. We can now estimate the fatigue strength for a certain number of cycles to failure for our material of interest. The stress based approach is appropriate in situations when yielding will not dominate material behavior. This translates to low stress loading situations corresponding to high cycle

fatigue of the material. The cycles to failure for a high cycle fatigue situation are above 10^5 cycles. This number will vary depending on the material that is being considered [2]. For times during testing or for a situation in which we have load data for which our mean stress is not equal to zero, it is possible to solve for the completely reversed stress equivalent, σ_{ar}, for any combination of mean stress and stress amplitude. This is accomplished by using the equation

$$\sigma_{ar} = \frac{\sigma_a}{1 - \frac{\sigma_m}{\sigma_f'}} \qquad (6)$$

We can then use the completely reversed stress equivalent value in our fitting equations with material constants that were derived in a test in which the mean stress was equal to zero.

It is also possible to have cyclic loading data where the stress amplitude varies during the time period of interest. This situation can be handled by using the Palmgren-Miner rule. With the Palmgren-Miner rule, each different load value is solved for separately and a value for number of cycles to failure is determined for each stress amplitude. Then the number of cycles that the material spends at each stress amplitude is divided by the number of cycles to failure calculated for that stress amplitude. The Palmgren-Miner rule states that material failure will occur when the sum of each of the cycles divided by cycles to failure is equal to unity

$$\frac{N_1}{N_{f1}} + \frac{N_2}{N_{f2}} + \frac{N_3}{N_{f3}} + ... = \Sigma \frac{N_i}{N_{fi}} = 1 \qquad (7)$$

If the sequence of loading as defined in the Palmgren-Miner rule is repeated multiple times, it is also possible to determine the number of repetitions, B_f, of the loading sequence that will result in failure. This is done by finding the multiple of the sum of the loading sequence ratios that will equal unity,

$$B_f \left[\Sigma \frac{N_j}{N_{fj}} \right]_{one-repetition} = 1 \qquad (8)$$

The stress based approach to fatigue life prediction is limited to small yielding conditions, but is still a useful tool in making fatigue life predictions for materials that have well defined material constants and axial loading conditions [2]. This research will have axial application of loads below the yield strength of PWA1484 which will allow the use of the stress based approach to fatigue.

2.1.2 Creep

Creep is a time dependant deformation which is affected by temperature, stress, material properties, and loading conditions and occurs slowly over relatively long periods of time [2]. Creep occurs in three stages which are primary, secondary, and tertiary as illustrated in Figure 7.

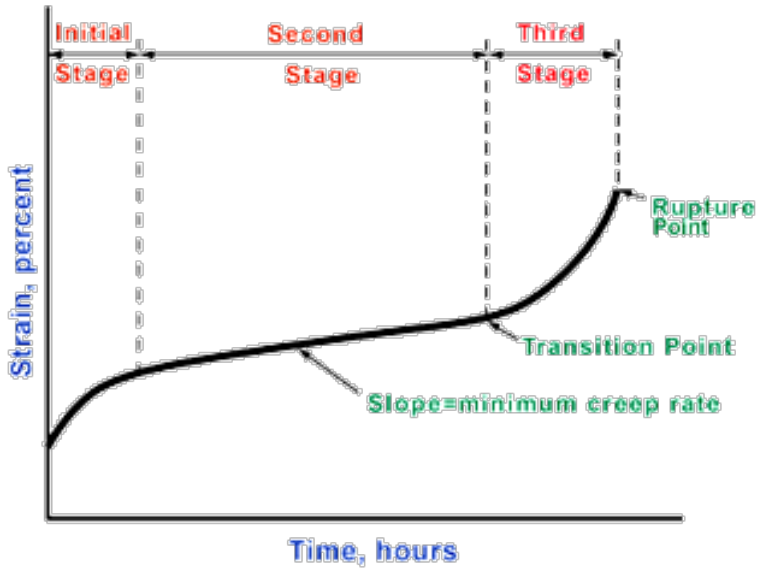

Figure 7: The Three Stages of Creep

The first stage of creep is called primary or transient creep. This stage of creep is a non-linear deformation that occurs during the beginning of a material's creep life. Before the beginning of primary creep there is an instantaneous elastic strain that occurs when the material is first placed under an applied load. After this instantaneous elastic strain, there will be a period of non-linear strain that will span the rest of the primary stage of creep [2]. During this non-linear strain, the material experiences hardening and the strain rate decreases for the rest of primary creep. Primary creep behavior is illustrated in Figure 8.

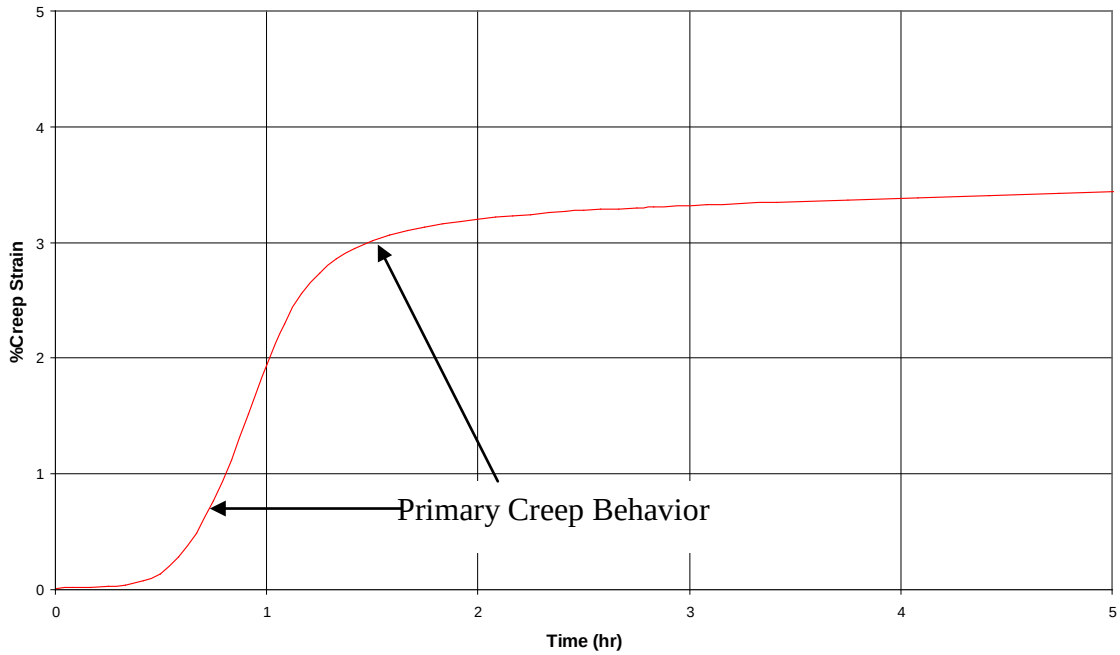

Figure 8: Example of Primary Creep

A microstructural description of primary creep in a single crystal superalloy is that mobile dislocations move through the gamma matrix and shear the gamma prime precipitates [1]. This shearing of precipitates allows the dislocations to move a greater distance through the material before they encounter another dislocation that will make it more difficult to move. Primary creep behavior will continue in the material until enough dislocations have built up at the gamma/gamma prime interfaces to stop dislocations from entering the gamma prime precipitates [1]. This transient creep behavior takes the mathematical form of

$$\varepsilon_t = f(\sigma)g(t) \qquad (9)$$

Where ε_t represents transient creep which is the product of some function of stress and a function of time [11]. First, we will examine the transient creep stress function, $f(\sigma)$. This stress function takes the form of the power law function

$$f(\sigma) = \left(\frac{\sigma}{\mu_c}\right)^p \qquad (10)$$

In this function, p is a positive, odd integer and μ_c is the transient creep constant for the material being considered. The time function in the transient creep function can have the form

$$g(t) = 1 - \exp\left(\frac{-t}{t_\varepsilon}\right) \qquad (11)$$

in which t_ε is the retardation time for the material which is the ratio of the tensile viscosity of a material to its elastic modulus, or the form

$$g(t) = t^{\frac{1}{q}} \qquad (12)$$

where q is a fitting constant. The first time function can be used for all values of time, but becomes less accurate at small values of time, while the second function is desirable because of ease of calculations, but it will become inaccurate for data that includes very large time values [11].

Following the primary stage of creep, there is a linear, or nearly linear, stage of creep called secondary or steady state creep. During steady state creep, the increase in strain with respect to time ($\dot{\varepsilon}$) decreases and becomes almost constant [2]. This steady

state creep region can be modeled using a power law relationship between steady state creep and stress. This power law relationship is represented by the equation

$$\varepsilon_s(t) = A\sigma^n t \qquad (13)$$

In this equation, A is a reciprocal viscosity coefficient and n represents the stress power term. This power law relationship is a widely used and accepted representation for steady state creep.

Combining the transient and steady state creep equation yields an expression for total creep during the primary and secondary regions of creep. This combination results in a summation of the strain equations

$$\varepsilon_c(t) = \varepsilon_s(t) + \varepsilon_t(t) \qquad (14)$$

which is equivalent to

$$\varepsilon_c(t) = A\sigma^n t + \left(\frac{\sigma}{\mu_c}\right)\left[1 - \exp\left(\frac{-t}{t_\varepsilon}\right)\right] \qquad (15)$$

By examining this equation for total creep strain, one can see that at values of time that are smaller than the retardation time, the transient term will be dominate; but as time gets large, the secondary creep term will become dominate.

The final stage of creep is called tertiary or unstable creep. During the tertiary stage, the strain rate increases in a rapid non-linear manner just before creep rupture of the material occurs [2]. Microstructurally, tertiary creep is caused by formation of voids which coalesce into larger voids and form micro-cracks in the material. To model the tertiary stage of creep, a model that includes a damage variable to describe the formation of voids in the material before creep rupture must be used [11,14]. Active research

continues to be performed to better describe the tertiary region of creep, and this research is beyond the scope of this theory discussion [14].

Another method to physically describe the creep behavior of materials and the equations derived above is through the use of rheological models. Rheological models are springs and dashpots arranged in a specific configuration to represent the creep behavior of materials. To describe the time dependent behavior of materials, rheological models represent elastic strain with an elastic spring and steady state creep with an oil filled dashpot. Linear viscoelastic models are appropriate for use when the strain rate of a material is proportional to the stress applied to that material. When a material exhibits linear viscoelastic behavior, the stress-strain relationship during individual time steps will be linear [2]. Many materials will behave in a linear viscoelastic manner at low stresses, but will become non-linear at higher stress levels. Some rheological models can also model the creep recovery behavior of materials. Recovery is defined as the time-dependent disappearance of creep strain after the removal of some or all of the applied stress [2]. One such rheological model is the Standard Linear Solid (SLS) model of a material. This model consists of a spring in series with a Kelvin-Voigt (KV) model, a second spring in parallel with an oil filled dashpot. Figure 9 below is an example of the SLS model.

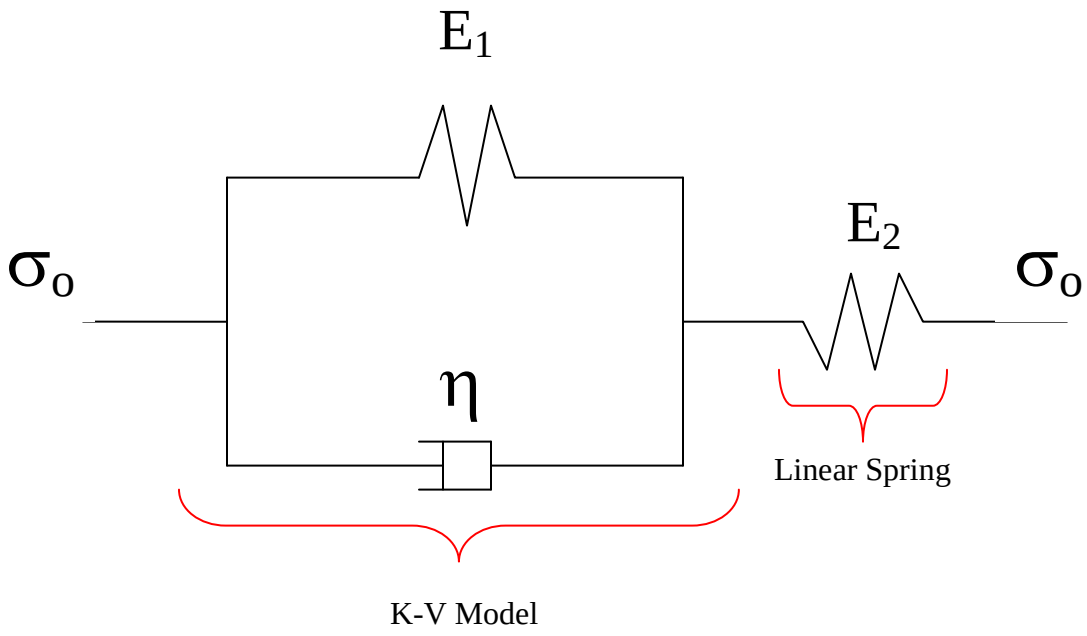

Figure 9: Standard Linear Solid (SLS) Model

The SLS model is able to represent instantaneous elastic strain when a load is applied and recovery behavior after an applied load is removed. Now let us consider the stress and strain relationships of the components of the SLS model.

Due to the spring portion and K-V portion of the SLS model being in series, the statement can be made that the stress in the spring and K-V portions of the model are equal,

$$\sigma = \sigma_{e2} = \sigma_{K-V} \qquad (16)$$

The strain in the SLS model is the added strains of the spring portion and the Kelvin-Voigt portion,

$$\varepsilon = \varepsilon_{e2} + \varepsilon_{K-V} = \frac{\sigma}{E_2} + \varepsilon_{K-V} \qquad (17)$$

The strain rate of the SLS model can then be said to equal

$$\dot{\varepsilon} = \frac{\dot{\sigma}}{E_2} + \frac{\sigma_c}{\eta} \qquad (18)$$

In order to use this equation, we must first solve for σ_c. We do this by remembering that the stress in the K-V portion of the model is equal to σ overall and equal to the sum of the stress in the spring portion and dashpot portion of the model internally. This will result in the equation $\sigma_c = \sigma_{K-V} - \sigma_{e1} = \sigma - E_1\varepsilon_{K-V} = \sigma - E_1(\varepsilon - \frac{\sigma}{E_2})$. Through algebraic manipulations this equation for the stress in the dashpot portion of the K-V model is written as $\sigma_c = \sigma\left(1 + \frac{E_1}{E_2}\right) - E_1\varepsilon$. This equation is then placed back into equation (18), which is the slope of the curve of strain with respect to time, and equation (18) becomes

$$\varepsilon = \frac{\dot{\sigma}}{E_2} + \frac{\sigma}{\eta}\left(1 + \frac{E_1}{E_2}\right) - \frac{E_1}{\eta}\varepsilon \qquad (19)$$

The strain rate equation is the governing equation for the SLS model.

The first behavior that we are interested in modeling is the creep behavior under an applied stress. To find this behavior we must solve the governing differential equation for strain with respect to time. The first step in this process is to separate the strain and stress variables into the form

$$\dot{\varepsilon}+\frac{E_1}{\eta}\varepsilon=\frac{\dot{\sigma}}{E2}+\frac{\sigma}{\eta}(1+\frac{E_1}{E_2}) \qquad (20)$$

We then multiply the equation by the integrating factor $e^{(\frac{E_1}{\eta})t}$. After this multiplication, the differential equation is easily solved giving

$$\varepsilon(t)=\frac{\sigma}{E_1}(1+\frac{E_1}{E_2})+Ce^{-(\frac{E_1}{\eta})t} \qquad (21)$$

The next step will be to solve for C. This step is accomplished by remembering that at time equal to zero, the only strain response that is present in the model is the instantaneous response of the linear elastic spring E_2, which makes the initial condition for strain $\varepsilon(0)=\frac{\sigma}{E_2}$. When we substitute this value into the strain equation while setting t=0, the value of C is found to be $-\frac{\sigma}{E_1}$. Placing this value into the strain equation and performing algebraic manipulation, we find that the equation for strain as a function of time of the SLS model is

$$\varepsilon(t)=\sigma(\frac{E_2+E_1}{E_2E_1})-\frac{\sigma}{E_1}e^{-(\frac{E_1}{\eta})t} \qquad (22)$$

The strain rate with respect to time will be

$$\dot{\varepsilon} = \frac{\sigma}{\eta} e^{-(\frac{E_1}{\eta})t} \qquad (23)$$

For the SLS model it can be noted that as time approaches infinity, strain will approach an asymptotic value of $\sigma(\frac{E_2 + E_1}{E_2 E_1})$. The retardation time for the SLS model is calculated by first solving for the initial strain rate at t=0 which we find to be $\dot{\varepsilon} = \frac{\sigma}{\eta}$. Next we again solve this simple differential equation to give us strain behavior that simulates the strain rate remaining at the initial value, remembering that we already have solved for C. The solution for this modified strain equation is

$$\varepsilon(t) = (\frac{\sigma}{\eta})t + \frac{\sigma}{E_2} \qquad (24)$$

The retardation time is found by setting strain equal to the asymptotic value and solving for time,

$$\sigma(\frac{E_2 + E_1}{E_2 E_1}) = (\frac{\sigma}{\eta})t_c + \frac{\sigma}{E_2} \qquad (25)$$

.

The retardation time for a SLS model is found to be

$$t_c = \frac{\eta}{E_1} \qquad (26)$$

When considering creep behavior, the standard linear solid equation for strain as a function of time, (7), accounts for the elastic strain as well as the primary region of creep strain. We contrast this with the total creep equation developed above, (15), and we see

that this equation accounts for the primary and secondary creep, but leaves out the initial elastic strain. This discussion of rheological models was undertaken simply to highlight the similarities of the SLS model with the generally accepted equation for total creep as a function of time, and to give a physical description of this behavior that is more easily visualized. The total creep equation (15) will be used to obtain a fit of the creep data collected during testing.

To meet the objectives of this research it will be necessary to calculate the amount of creep damage caused by dwell time at given stress. In order to estimate this damage, we will need to have an estimate for the rupture time at a given stress and a given temperature. Time-temperature parameters produce life estimates for a material relative to creep at a given temperature. One of the time-temperature parameters that are used in the analysis of creep in superalloys is the Larsen-Miller parameter (LMP). Before we discuss the LMP, we will quickly define the activation energy, Q. The activation energy of a material is defined as the energy barrier that atoms must overcome to move past other atoms in a solid [13]. The activation energy, Q, will depend on material properties and creep mechanisms, but this value can often be determined through analysis of test data. This analysis consists of plotting $\log \dot{\varepsilon}$ vs. 1/T at a constant level of stress [2]. The activation energy will have a value approximately equal to the slope of the plot. This value of Q should be correct for a range of stresses and temperatures, but large changes in either stress or strain can result in a change in activation energy for the material. The Arrhenius rate equation is also a foundation of the LMP. The Arrhenius rate equation was developed by Svante Arrhenius who determined through experimental observations

that the rate of many reactions could be related to the temperature at which they occur [13]. This relationship takes the form of the equation (27) used below.

The LMP begins with the Arrhenius rate equation,

$$\dot{\varepsilon} = Ae^{\frac{-Q}{RT}} \qquad (27)$$

The first step in the derivation of the LMP is to write the above Arrhenius equation in differential form with the A coefficient represented as a function of stress

$$d\varepsilon = A(\sigma)e^{\frac{-Q}{RT}}dt \qquad (28)$$

After integrating the equation, the constant of integration is thrown out so that only steady state strain is left in the equation. This equation will take the form

$$\varepsilon_{sc} = A(\sigma)te^{\frac{-Q}{RT}} \qquad (29)$$

From this equation, a new quantity theta is defined that is of the form

$$\theta = te^{\frac{-Q}{RT}} \qquad (30)$$

Theta is called the temperature compensated time term. From experimental results it has been documented that the creep strain at rupture is constant at a given value of theta, θ_r [2]. We can now say that the equation for the LMP is

$$LMP = .217Q = T(\log t_r + C) \qquad (31)$$

Where

$$C = -\log \theta_r \qquad (32)$$

It can be seen from this equation that we can predict service life based on the Larsen Miller parameter for a given stress, and the temperature or max temperature allowed for a desired service life. The LMP makes the assumption that the activation energy, Q, will vary with stress and that θ_r will not change with stress, but will be a material constant [2]. For many metals, including superalloys, a good estimate for the value of C is 20.

2.1.3 Creep and Fatigue Interaction

The area of creep fatigue interaction is not completely understood and research is still continuing in this area of superalloy behavior. In order to tie the fatigue and the creep theory discussed above together, we will consider a linear damage summation of creep and fatigue as proposed by Wright et al. [12]. This theory allows creep to be associated with fatigue loading through means of damage terms. The use of this approach during this research is to allow for observations to be made about creep and fatigue interaction. Research by Wright and colleagues modeled the creep and fatigue interaction of PWA1484 during fatigue tests at varying frequencies and R values at 1038°C. It was found that the fatigue behavior of PWA1484 was linear when plotted on log-log coordinates. This allowed Wright to invoke a power law relationship to predict the cycles to failure for a specified cyclic load. The equation used to describe fatigue took the form of the equation

$$N_f = \left(\frac{\sigma_{eq}}{A} \right)^{\frac{1}{B}} \qquad (33)$$

where the stress term represents an equivalent stress calculated using the Walker equation to account for the effects of different values of mean stress in the data used to perform the power law fit to the fatigue data [12]. A and B are material constants for PWA1484 during fatigue at a given temperature. The Walker relationship calculates an equivalent stress for any value of R used in fatigue loading with the equation

$$\sigma_{eq} = \sigma_a (1-R)^w \qquad (34)$$

Where w is the Walker constant that is solved for by performing a multiple linear regression fit of the cycles to failure, stress amplitude, and the stress ratio. The damage term for a certain number of fatigue cycles would be given by

$$D_{fatigue} = \frac{N_{obs}}{N_f} \qquad (35)$$

This fatigue damage term in equation (35) can also be related to time by multiplying the number of cycles in the numerator and the denominator by 1 over the frequency of fatigue loading.

$$D_{fatigue} = \frac{N_{obs} * \frac{1}{frequency}}{N_f * \frac{1}{frequency}} = \frac{t_{obs}}{t_{failure}} \qquad (36)$$

The power law relationship for fatigue behavior at 871°C was developed by leveraging fatigue data in Table 1. This fatigue data was from previous fatigue testing and also included fatigue data generated during this research [26]. Data from 15 fatigue tests was used to determine the power law relationship and the walker coefficient. The Walker coefficient was solved for by means of a multiple linear regression fit to the data

performed in Excel. The Walker coefficient for this test data at 871°C was found to be 0.232. This coefficient can be placed into equation number (34) to give the result

$$\sigma_{eq} = \sigma_a (1-R)^{.232} \qquad (37)$$

Table 1: PWA1484 Fatigue Data at 871°C

Stress (MPa)	N_f	R	Frequency (Hz)
827.37	3.00E+03	0.05	0.17
792.90	1.30E+04	0.05	0.17
758.40	1.60E+04	0.05	0.17
758.40	1.80E+04	0.05	0.17
758.40	2.40E+04	0.05	0.17
758.40	5.60E+04	0.05	1.00
758.40	8.00E+04	0.05	1.00
689.50	3.00E+03	0.05	0.17
689.50	2.30E+04	0.05	1.00
689.50	3.30E+04	0.05	0.17
689.50	4.00E+04	0.05	0.17
689.50	3.00E+05	0.05	1.00
620.53	1.80E+05	0.05	0.17
517.10	1.77E+05	-1	0.50
517.10	9.00E+04	-1	0.50

The constants A and B were also solved using a multiple linear regression fit in Excel with A and B equaling 2244 MPa and -0.111 respectively. These constants are added to Equation number (2) to finish the power law fatigue relationship for PWA1484 at 871°C

$$\sigma_{eq} = 2244 N_f^{-0.111} \qquad (38)$$

This power law relationship provided a reasonable fit to the data from Table 1, and this fit is illustrated in Figure 10.

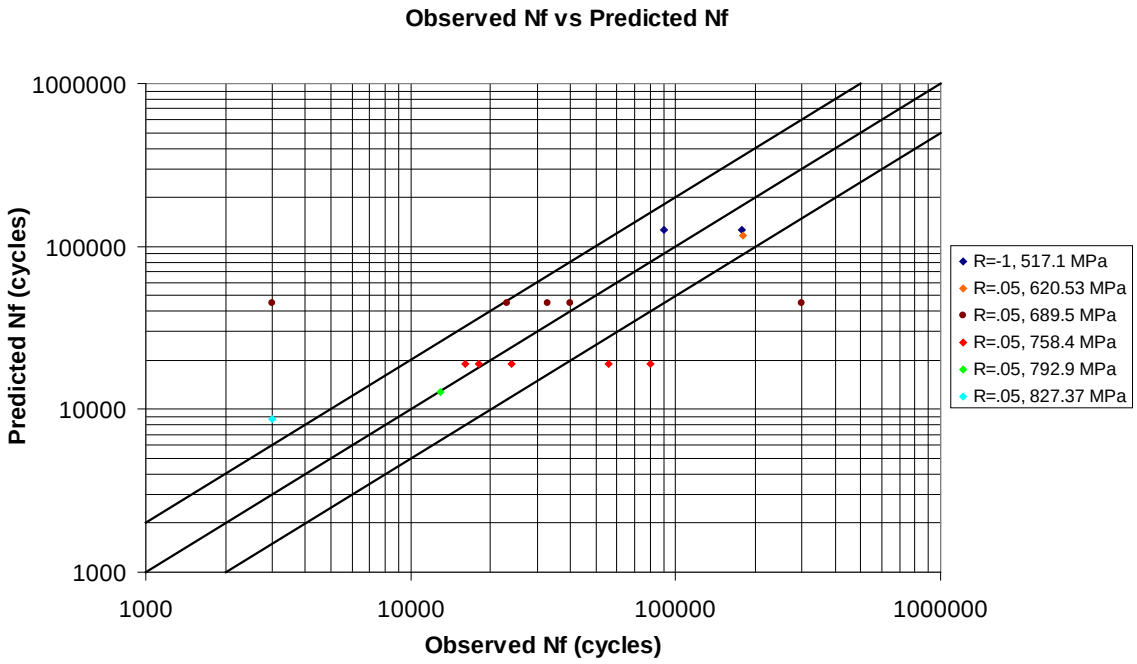

Figure 10: Predicted vs. Observed Fatigue Behavior for PWA1484 at 871°C

To include creep effects during fatigue loading, a rupture damage term is calculated that can be added to the fatigue damage term from Equation (35) [12]. The first step in developing this rupture term is developing a relationship between an applied stress and the rupture time at that stress. Wright et al. developed an equation for rupture time as a function of applied stress by first determining that the rupture behavior of PWA1484 behaved linearly on a log-log plot of rupture time vs. applied stress [12]. This allows a power law relationship to be applied to relate applied stress to rupture time. It is then possible to relate this rupture function to fatigue cycling by dividing each fatigue cycle into 200 discrete stresses and 200 blocks of time that represent the dwell time at each stress. One can then divide the time spent at each stress value by the rupture time for that stress. This produces a damage term for each stress during the cycle. The sum of

the damage terms of one cycle represents the cumulative rupture damage caused by that fatigue cycle. This research will be different than the procedure used by Wright et al., because not enough rupture tests were performed to develop a power law fit to the rupture data at 871°C. In order to estimate the rupture times for this research, previous rupture testing data will be used to develop a Larsen Miller relationship to estimate the rupture life of a given stress at 871°C. The steps for developing the Larsen Miller relationship and dividing the plot of time vs. stress into discrete values are as follows. The Larsen Miller relationship takes the form of Equation (31). A Larsen-Miller plot was developed for creep rupture data as well as creep to 5% creep strain data. The data in Table 2 is creep rupture data from previous PWA1484 testing performed by Wright and Cetel [3, 12].

Table 2: PWA1484 Creep Rupture Data

Stress (MPa)	Temperature (°K)	Rupture Time (hrs)	LM Parameter
206.8	1310.9	70.7	28643.1
227.5	1310.9	42.4	28352.0
241.3	1310.9	34.4	28232.9
248.2	1255.4	350.0	28301.1
275.8	1310.9	16.2	27804.2
413.7	1144.3	1266.0	26435.2
551.6	1144.3	370.0	25823.9

From this data, the Larsen-Miller plot in Figure 11 was produced. It was found that the Larsen-Miller coefficients displayed a linear relationship with stress when plotted on log log coordinates. A power law relationship was used to develop an equation for the LMP

as a function of stress. The Equation illustrated on Figure 11 was used to solve for the LMP for each stress level in the time vs. stress plot for one fatigue cycle.

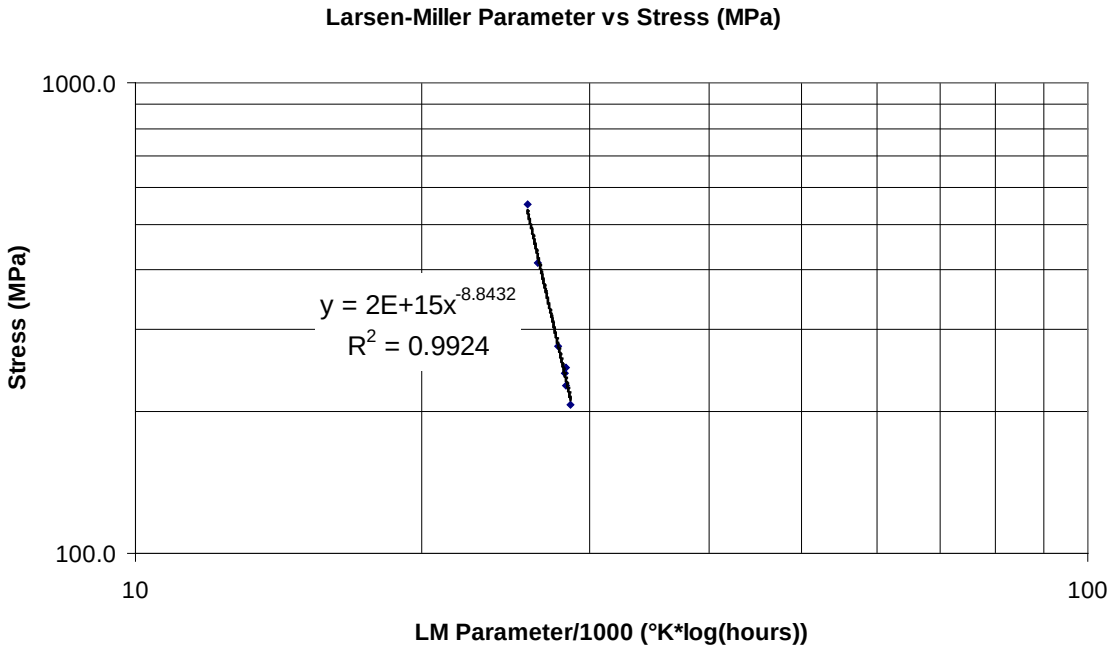

Figure 11: Larsen-Miller Plot for Creep Rupture

Creep data representing the time to 5% creep strain at a range of stresses and temperatures was also used to solve for the LMP at 5% creep strain. The data in Table number 3 was from previous PWA1484 testing conducted by Pratt and Whitney [14]. This data will be used during testing in this research that is interrupted at 5% creep strain. The LMP at 5% creep strain allows the time to 5% creep strain to be estimated for a given applied stress. The data in Table number 3 was plotted on log-log coordinates and found to display a linear relationship with stress which allowed for a power law relationship to be fit to the data.

Table 3: Creep Data to 5% Creep Strain

Stress (MPa)	Temperature (°K)	Time to 5% Creep (hrs)	LM Parameter
413.7	1144.3	333.2	25772.7
248.2	1310.9	20.0	27924.2
186.2	1310.9	130.0	28989.8
137.9	1310.9	740.0	29980.0
517.1	1144.3	139.5	25340.0
344.7	1255.4	35.0	27045.8
448.2	1199.8	55.0	26084.5
344.7	1199.8	285.0	26941.8

The Equation in Figure 12 was used to estimate the Larsen-Miller parameters for the testing that was interrupted at 5% creep strains.

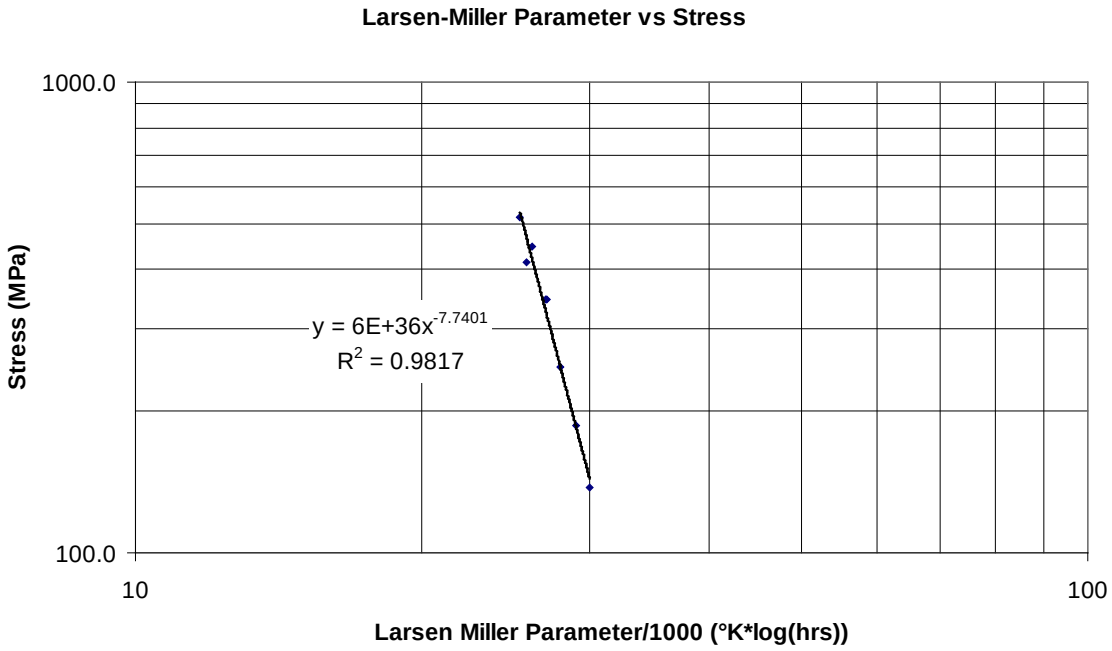

Figure 12: Larsen-Miller Plot for 5% Creep Strain

To use the LMP to estimate creep times to rupture or 5% creep strain the fatigue cycle was separated into distinct stress values. A sine function with a period of 2 seconds was used to approximate the shape of the fatigue cycle. The stress as a function of time was

$$\sigma = \sigma_{alt} * \sin(\pi * t) \qquad (39)$$

From the LMP that corresponded to each stress, a rupture time, or time to 5% creep strain was estimated for each stress. For a test that had an end state of failure, the LMP for failure was used, and for a test that had an end state of 5% creep strain, the LMP for 5% was used. The estimated time was then applied to solve for a damage term using the equation

$$D_{\Delta t} = \frac{\Delta t}{t_r} = \frac{\Delta t}{10^{\left(\frac{PLM}{^\circ K}\right)-C}} \qquad (40)$$

Equation number (41) represents the damage that occurs during one time step as part of one cycle of loading. The damage that occurred in one cycle could be calculated as the sum of all of the damage in the individual time steps

$$D_{cycle} = \Sigma D_{\Delta t} \qquad (41)$$

Equation number (42) represents a numerical integration of the fatigue loading cycle. The damage at failure was set to a value of 1. The number of cycles to failure could then be calculated using the simple formula

$$D_{failure} = 1 = N_f * D_{cycle} \qquad (42)$$

Also, the damage coefficient at a specific number of cycles could also be calculated. This rupture damage in equation number (43) can be added to the fatigue damage coefficient as a simple analysis of creep and fatigue interaction [12]. For this relationship we set the damage at failure equal to one and set it equal to the sum of the rupture and fatigue damage

$$1 = D_{fatigue} + D_{Rupture} \qquad (43)$$

This fatigue and creep interaction model will use data from this research to assess the applicability of a linear summation of creep and fatigue data to describe creep and fatigue interaction. It will be the goal of this research to attempt to first be able to quantify creep and fatigue interaction through observation and numerical analysis of test results, and then attempt to describe it through microstructural characterization via scanning electron microscopy.

III. Material and Experimental Setup and Methods

3.1 Chapter Overview

The purpose of this chapter is to describe the material and test specimens used for this research.

3.2 Material Description

The material used for this testing is Pratt and Whitney Alloy 1484 (PWA1484). This material is a second generation, single crystal, nickel based superalloy. Material for testing was acquired from existing material stock at the Air Force Research Laboratory, which was remnant material from the research of Wright et al. [12]. The material used in this research consists of two slabs of PWA1484 with serial numbers of Z175T and A2LPT. Each of the material slabs were known to have an orientation within 6° of the <001> plane.

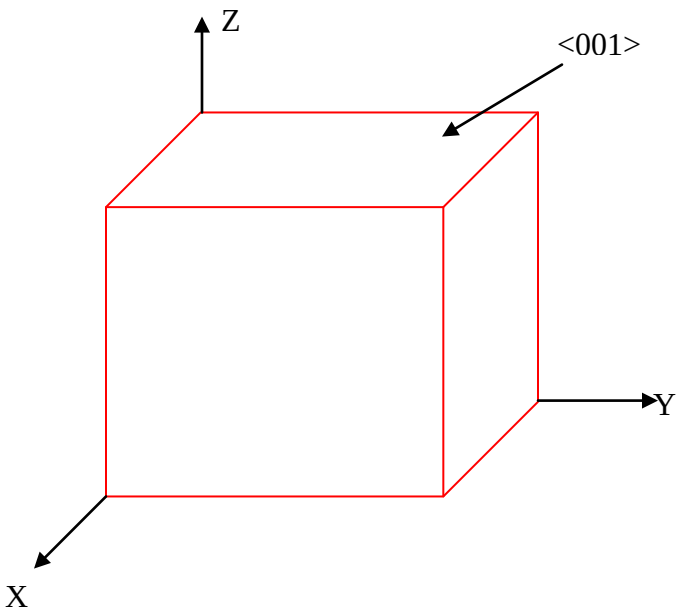

Figure 13: <001> Plane Illustration

The slabs were both spot polished and the microstructure was examined in order to determine which direction the structure was offset from the <001> plane. After this was determined, the specimens taken from each slab were machined at an angle that would make the specimens within 2° of the <001> orientation.

3.3 Test Specimen Configuration

The test specimen geometry used for testing was similar to the configuration used by Pratt and Whitney during earlier testing of PWA1484. Figure 14 is an image of one of the test specimens used during this research. The test specimens were machined and polished according to usual mechanical test specimen preparation specifications.

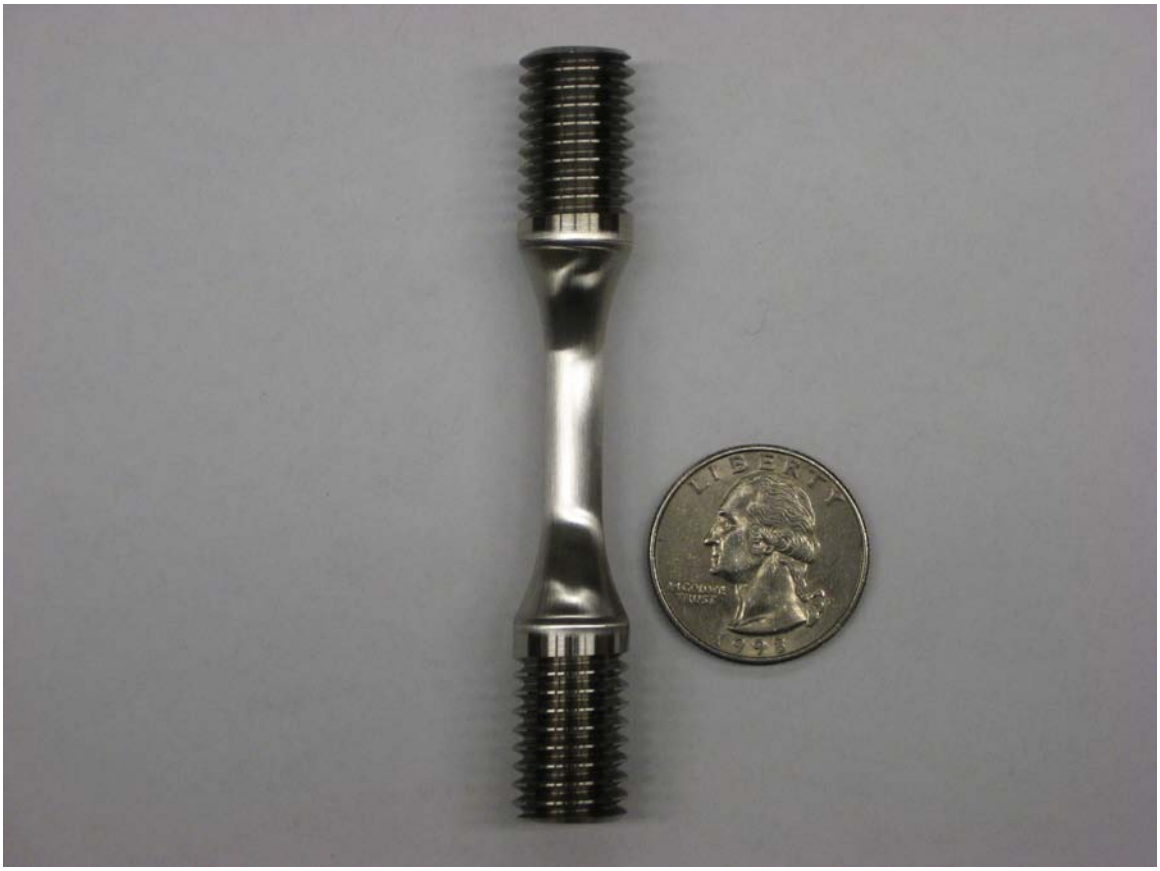

Figure 14: PWA1484 Test Specimen

3.4 Experimental Methods

In order to acquire more data of the creep and fatigue interaction behavior of PWA1484, 4 test conditions were used.

Test Condition #1 was a Fatigue test. This test was conducted at a constant temperature of 871°C. Testing was conducted at a frequency of 0.5Hz and a maximum stress level of 517MPa under fully reversed loading conditions, R=-1. The specimen was cycled until failure. Data collected included number of cycles at failure (N_f), load, time elapsed, temperature, and stress strain hysteresis loops at specified cycles during testing.

Test Condition #2 was a constant stress creep test. This test was conducted at a constant temperature of 871°C and a constant stress of 517MPa. The specimen was loaded into the test fixture, brought to temperature, and ramped to a constant stress of 517MPa. This stress was applied until the specimen reached 5% creep strain (the strain that was considered failure for the purpose of this research) which was the strain accumulated after any elastic strain that was accumulated during initial loading of the specimen. Data collected included load, strain, elapsed time, and temperature.

Test Condition #3 was a two part test that included fatigue followed by creep. This test was conducted at a constant temperature of 871°C. The specimen was placed under fatigue loading at the same maximum applied stress and frequency as test Test Condition #1 above. The specimen was cycled until the number of cycles was equal to $.5N_f$. At that time, the test was transitioned to a constant creep test of the same format as Test Condition #1 above. The specimen was loaded with the same load as Test Condition #2 and held at that load until a creep of 5% was reached. Data collected during both portions of this test included strain, temperature, elapsed time, applied stress, and stress strain hysteresis loops in the fatigue portion of testing.

Test Condition #4 was a combined constant creep then fatigue test. This test was conducted at a constant temperature of 871°C. The specimen was loaded at a constant load identical to Test Condition #2 and held until the specimen reached 2.5% creep strain. Then the test was transitioned to a low cycle fatigue test with the same load profile as Test Condition #1. The specimen was then cycled until failure. Data collected during both portions of this test included strain, temperature, time elapsed, applied stress, and

stress strain hysteresis loops during the fatigue portion of the test. Additional tests would either repeat these four test conditions to assess material variability or modify the functional damage in Test Conditions 3 and 4 to assess the mechanisms of damage accumulation. After each of the tests, fractography was performed on the fracture surfaces of the specimens tested to failure, and samples were cut from all four test specimens and used for microstructural analysis in the scanning electron microscope. Figure numbers 15 and 16 on the following pages are flow charts for each test condition.

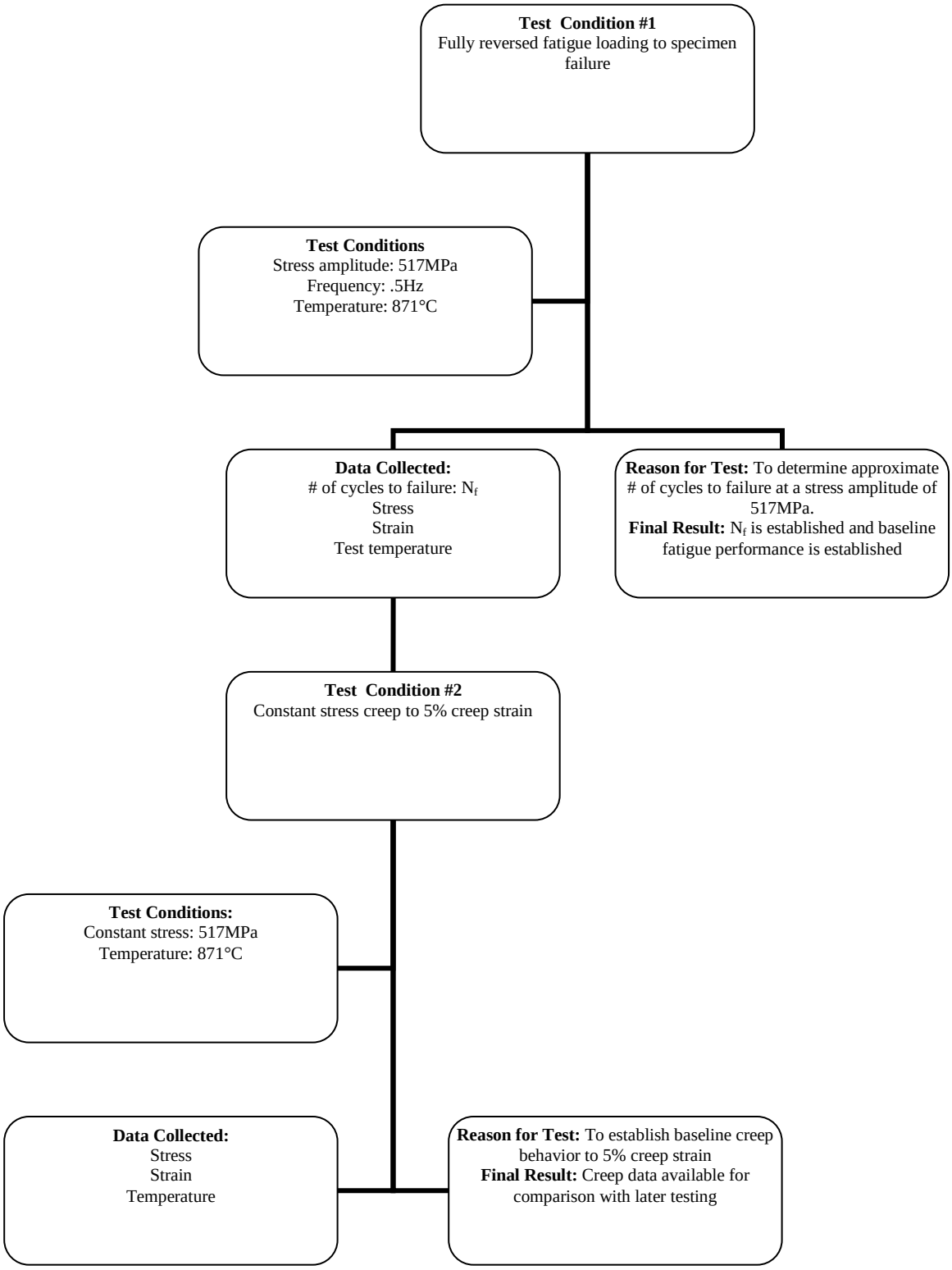

Figure 15: Test #1 and #2 Flow Chart

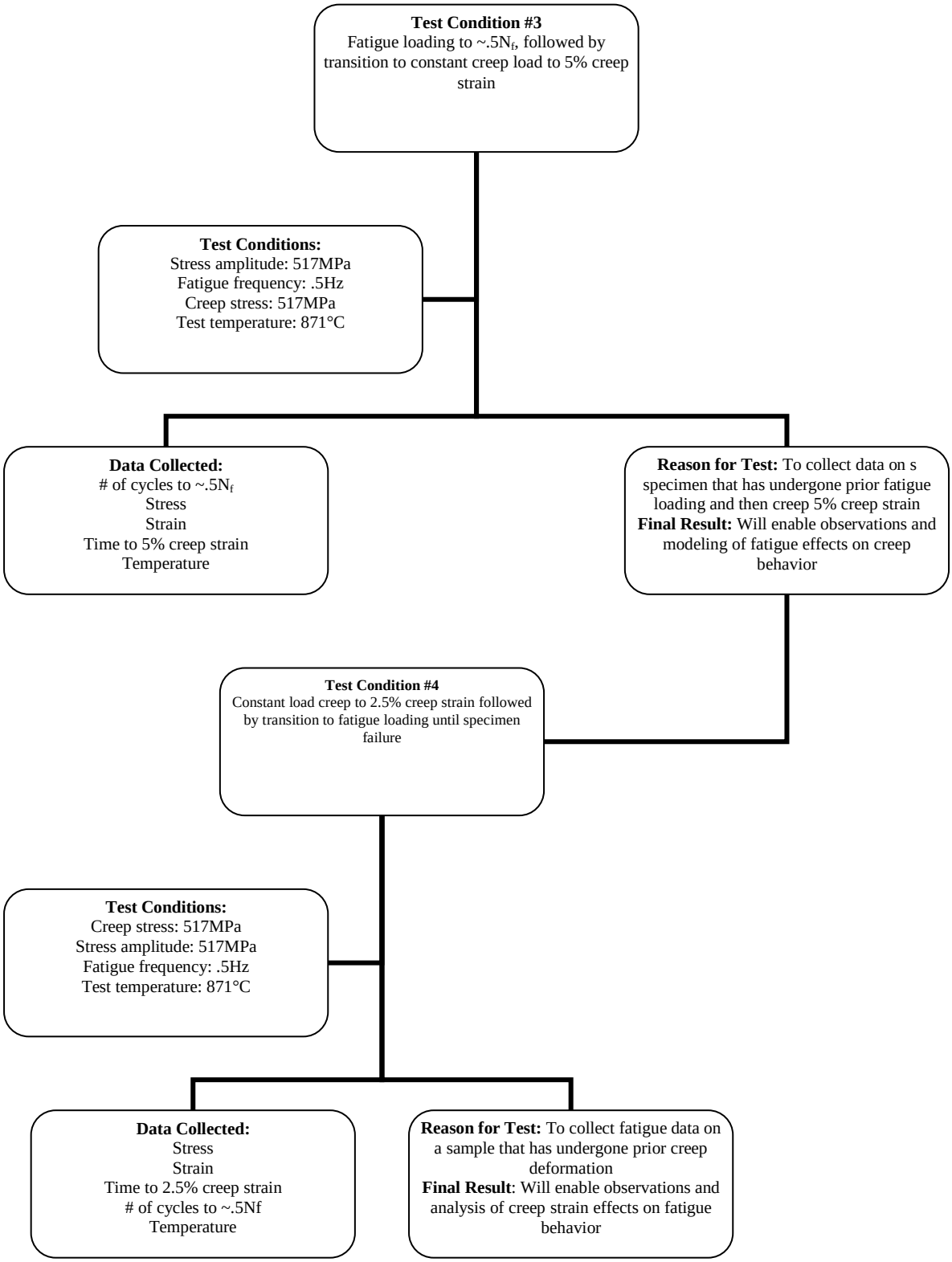

Figure 16: Test #3 and #4 Flow Chart

3.5 Summary

Ten identical specimens were cut from two slabs of PWA1484, and four tests were conducted in order to gather data to describe the creep and fatigue interaction behavior of PWA1484.

IV. Experimental Setup

4.1 Chapter Overview

The purpose of this chapter is to describe the equipment and test setup used in this research. All testing and SEM work was performed at the Air Force Research Lab Materials and Manufacturing Directorate.

4.2 Test Equipment

The test equipment used for performing the creep and fatigue testing consisted of a servo-hydraulic test rig, a temperature conditioning furnace, and a digital test controller with a computer interface. Figure numbers 17 and 18 show the test equipment.

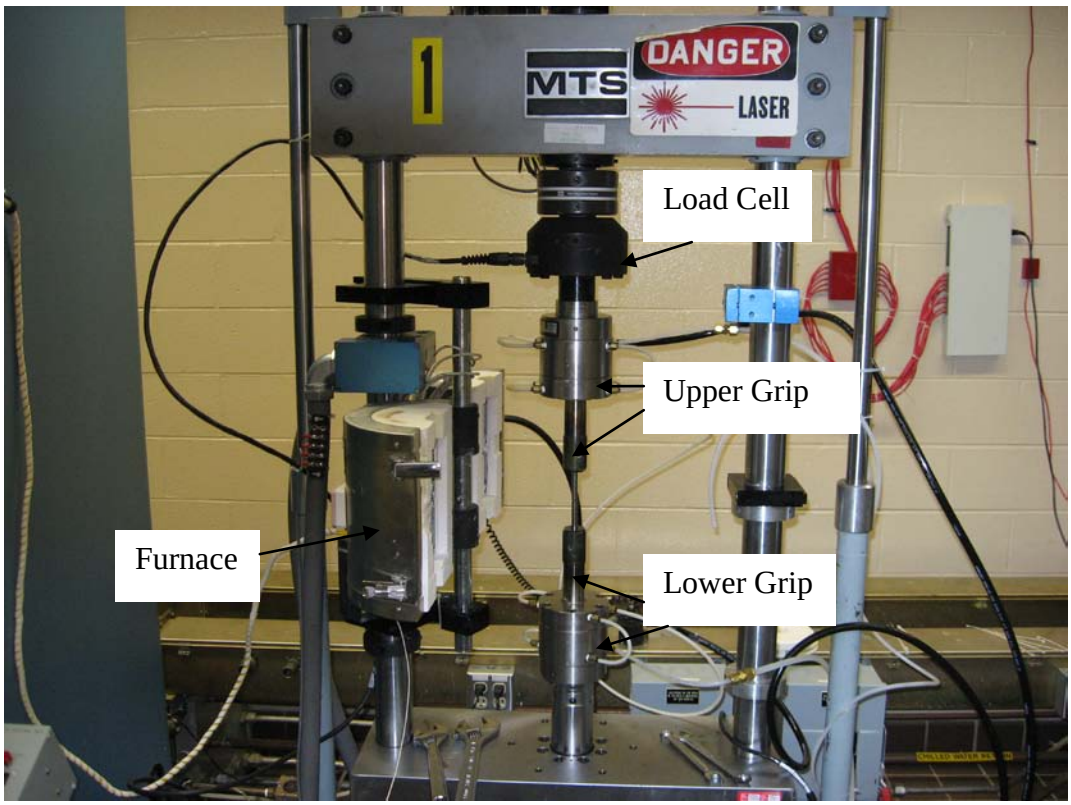

Figure 17: Servo Hydraulic Test Rig with Furnace

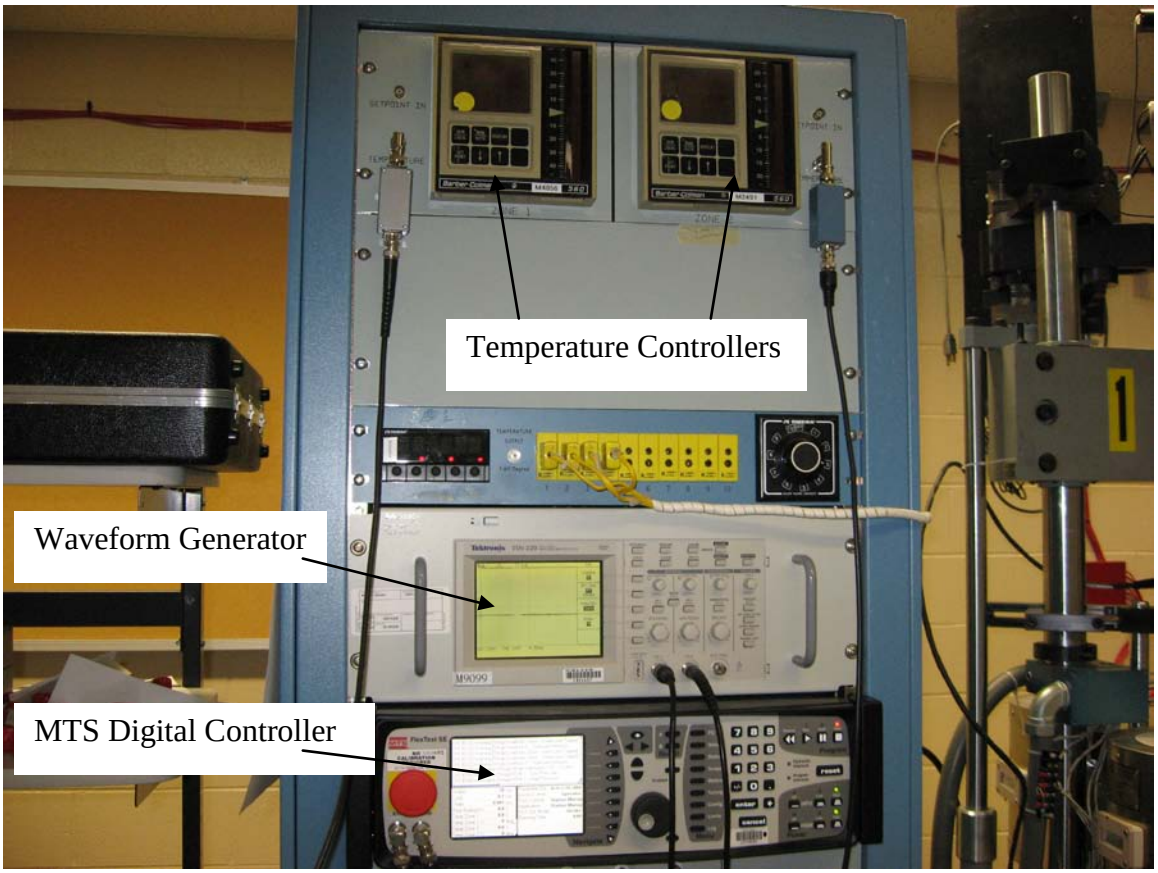

Figure 18: MTS Flex Test Controller (bottom) and Barber Colman Furnace Temperature Controllers (top)

The test rig is an MTS servo-hydraulic test unit that is capable of running fully reversed fatigue loading as well as constant load creep tests. All testing will be performed at 871°C and this temperature is achieved through the use of an ATS furnace that is rated at 1000°C (1832°F). The ATS furnace is divided into two temperature zones each of which is controlled by a separate temperature control unit that monitors the temperature inside the furnace through a thermocouple mounted on the test specimen. The temperature controllers automatically adjust the power of the furnace in each zone to maintain a pre-set temperature. The test rig is controlled through a MTS flex test SE controller with a

software user interface. Through this controller, settings are specified for each phase of the test. These settings include loading frequencies and load levels, data acquisition rates, times during the test when data is to be acquired, and what parameters in the test will be considered to be interlocks. An interlock is a test condition such as maximum load or maximum displacement of the servo-hydraulic piston actuator that, when met, will stop the test. The flex test controller maintains proper loads for each test through the use of a load cell that is installed in line with the test specimen. The load cell used in this research is a 50KN, full wheatstone bridge load cell. The load cell provides feed back to the flex test controller and lets the controller know what load is being applied to the specimen. The controller is then able to maintain the pre-set testing load.

Pre- and post-test microstructure analysis is accomplished through the use of a Quanta scanning electron microscope (SEM). The SEM is shown in Figure number 19. Backscatter imaging was performed for the pre- and post-test microstructure analysis. Secondary electron imaging was used to perform fractography analysis on the specimens from Test numbers 1 and 4 that failed during fatigue cycling.

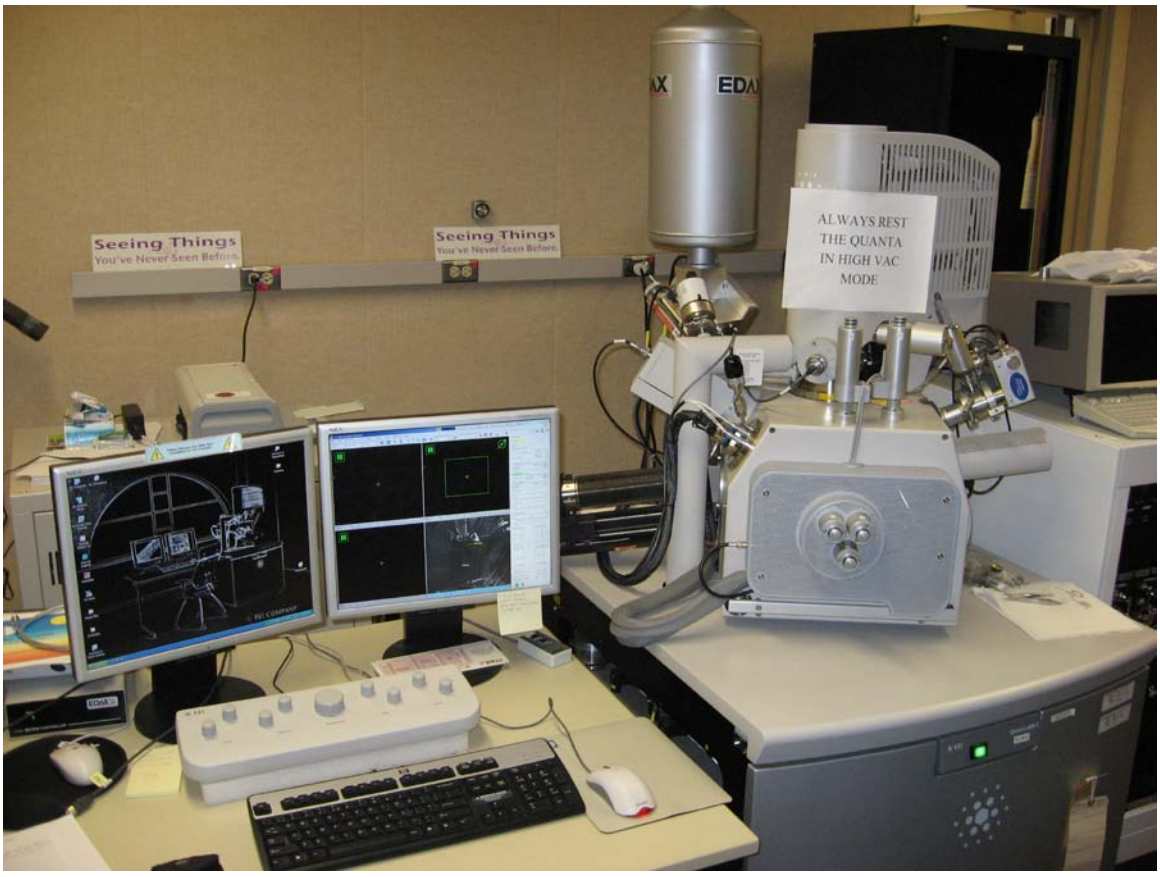

Figure 19: The Quanta Scanning Electron Microscope

4.3 Test Setup

The test equipment mentioned above is permanently configured to perform tensile and fatigue testing. The test setup will include installing high temperature grips and performing alignment procedures on the test unit. The grips used for this research are model 680 high temperature grips that are rated for temperatures up to 982°C. The grips are installed on the upper cross member and the lower piston of the MTS machine. After the grips are installed, a two piece alignment specimen is installed in the grips. Adjustments are made to the top grip using an adjustment collar that allows adjustments

to be made to the angular and concentric alignment of the top grip with the lower grip. The upper grip is adjusted until alignment is achieved between the top and bottom portions of the alignment specimen. The next step in the alignment process is the installation of a steel dummy specimen that has twelve strain gages that are installed in 3 locations with four strain gages in each location at 0, 90, 180, and 270°. Figure number 20 is an image of the alignment specimen.

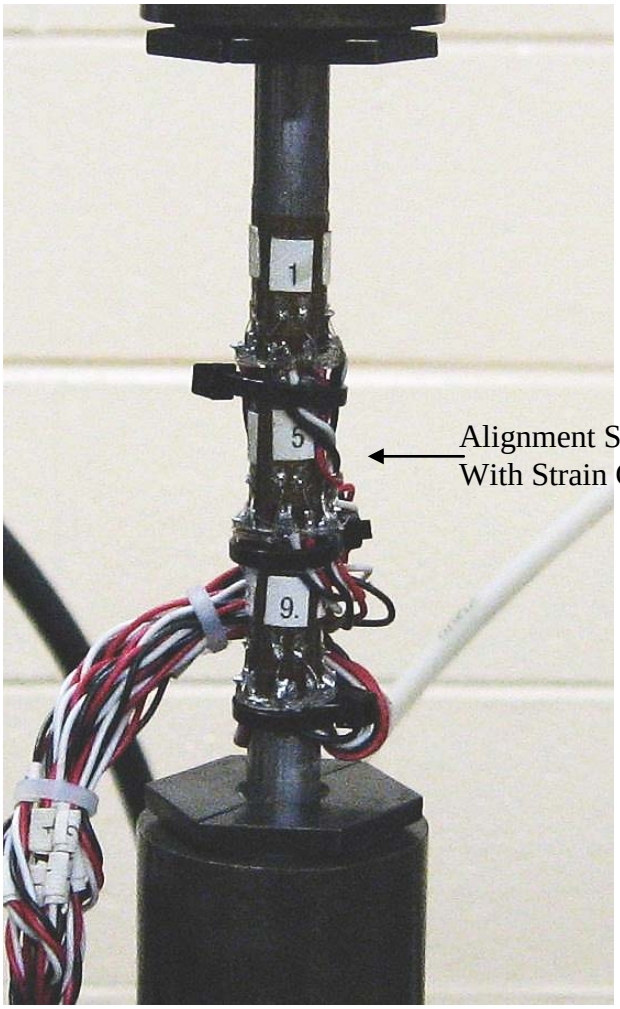

Figure 20: Instrumented Steel Alignment Specimen

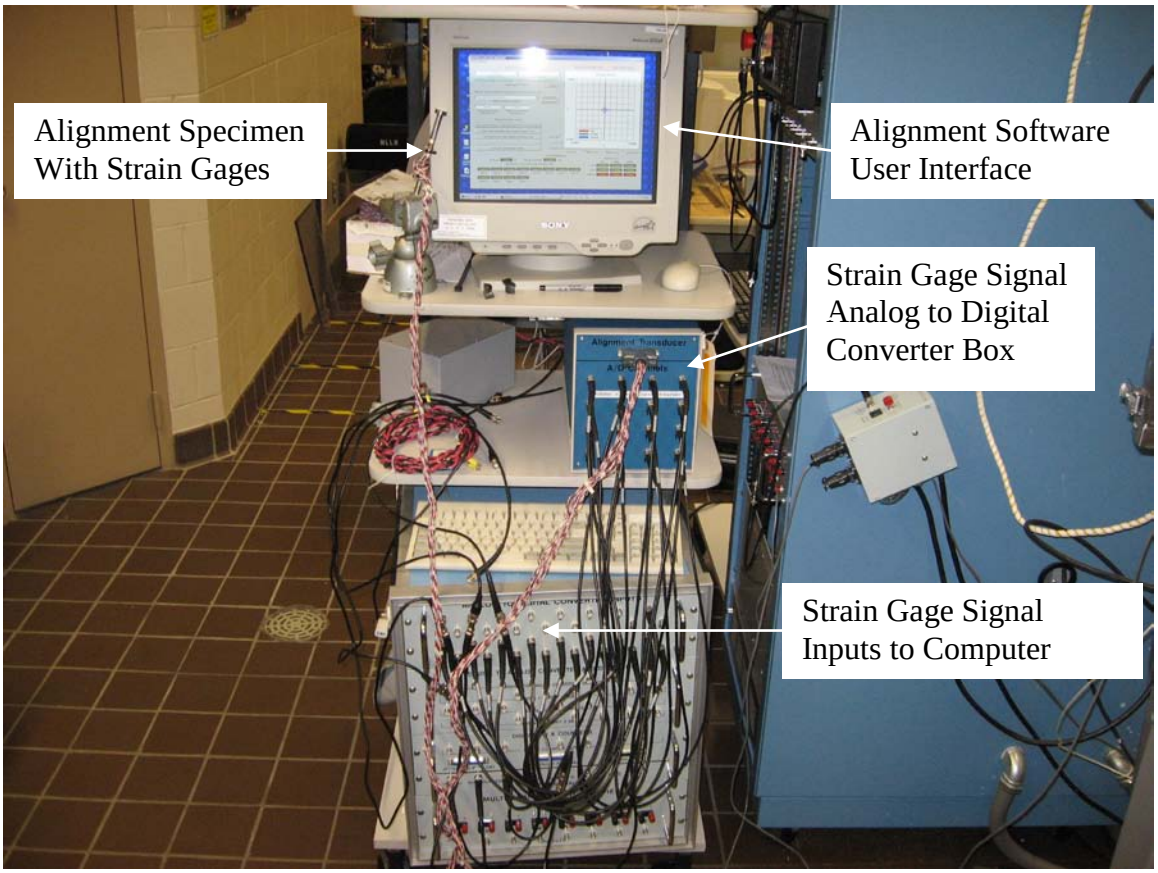

Figure 21: Data Collection Unit for Alignment Specimen

This instrumented test specimen allows the top, middle, and bottom portions of the gage section to be examined for bending strains. The upper grip can then be adjusted further until the bending strains in the test specimen are within the acceptable parameters of 5% bending at 5,000με. After this is accomplished the test rig is considered to be in alignment and the upper grip will not be adjusted for the remainder of this research. The grips are assumed to maintain alignment at elevated temperatures.

After the grips are aligned, the test specimen is threaded into the grips and hydraulic pressure is applied to the grips to ensure no movement of the specimen during

creep or fatigue testing. Four thermocouples are then welded to the specimen, two on the upper shoulder of the specimen and two on the lower shoulder. These are K-type thermocouples that serve as temperature inputs into the two temperature controllers. One thermocouple on each shoulder is used as the controller input and the other thermocouple is used for a backup so that testing will not be interrupted if one thermocouple goes bad. A fifth beaded thermocouple is secured on the center of the gage section of the test specimen with thermocouple wire, and serves as a monitor for the temperature of the gage section of the test specimen (see Figure 22). The fifth thermocouple is not welded to the gage section of the specimen because the welding process could result in a change in material properties at the weld site as well as the possibility of a notch at the weld site that would degrade the performance of the specimen. The temperature of the beaded thermocouple in the center of the gage section of the specimen is considered to be the test temperature of the specimen.

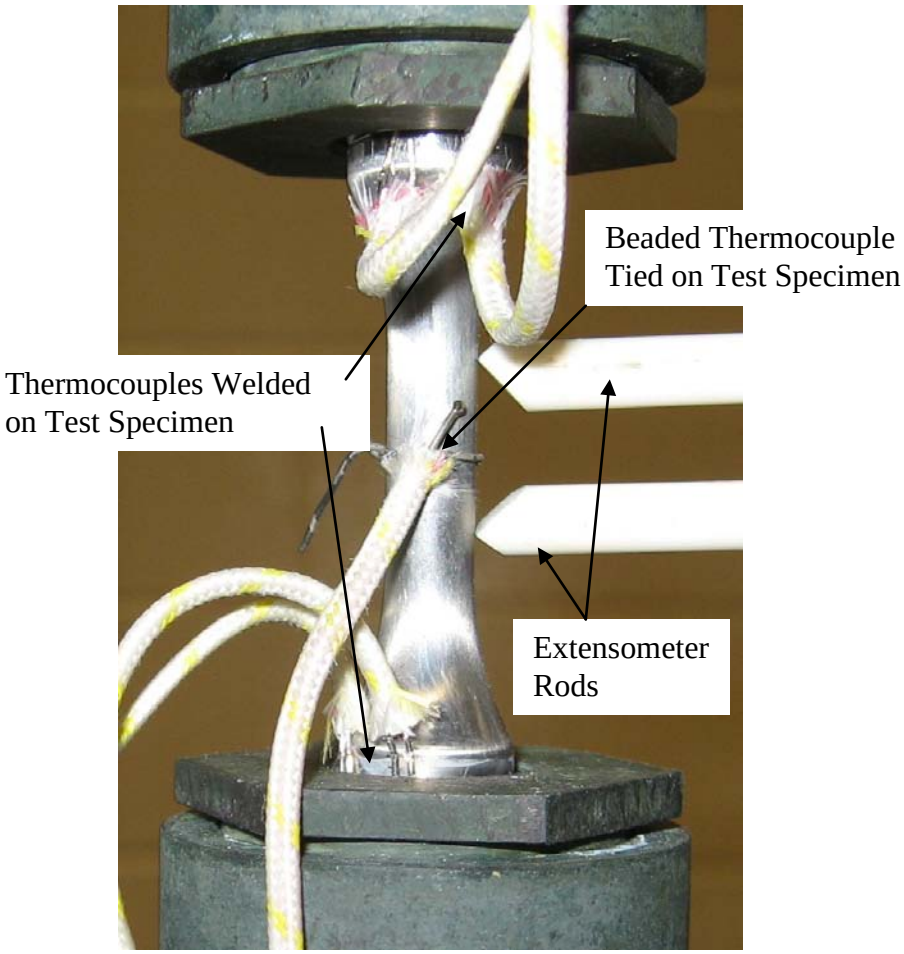

Figure 22: Specimen with Thermocouples Attached and Extensometer Mounted

After the thermocouples are installed on the specimen, the extensometer is installed, furnace power is turned on and the temperature controller set points are adjusted until the desired test temperature in the gage section is achieved. After the test specimen has reached test temperature, the test interlocks are enabled and the test profile is loaded using the MTS flex test controller software. Testing is then started and the test runs to completion.

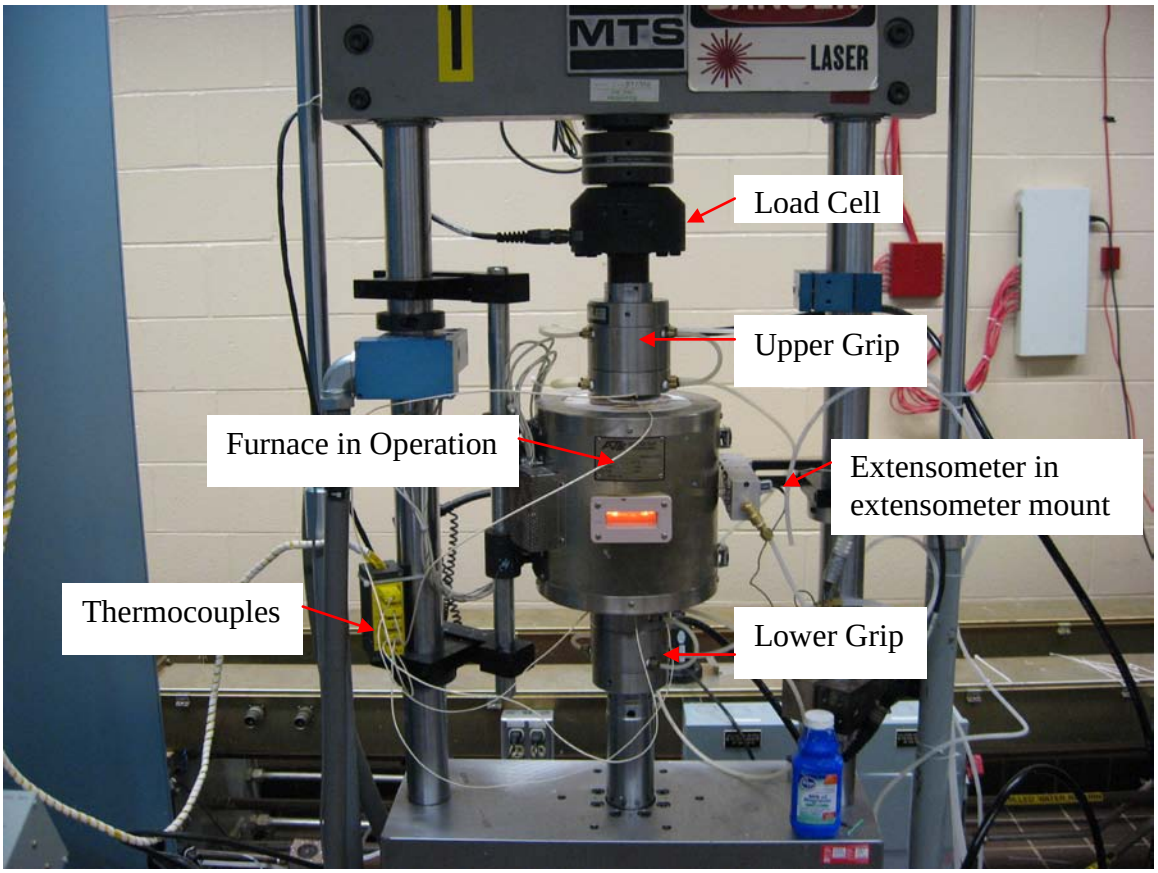

Figure 23: Test Equipment in Test Configuration

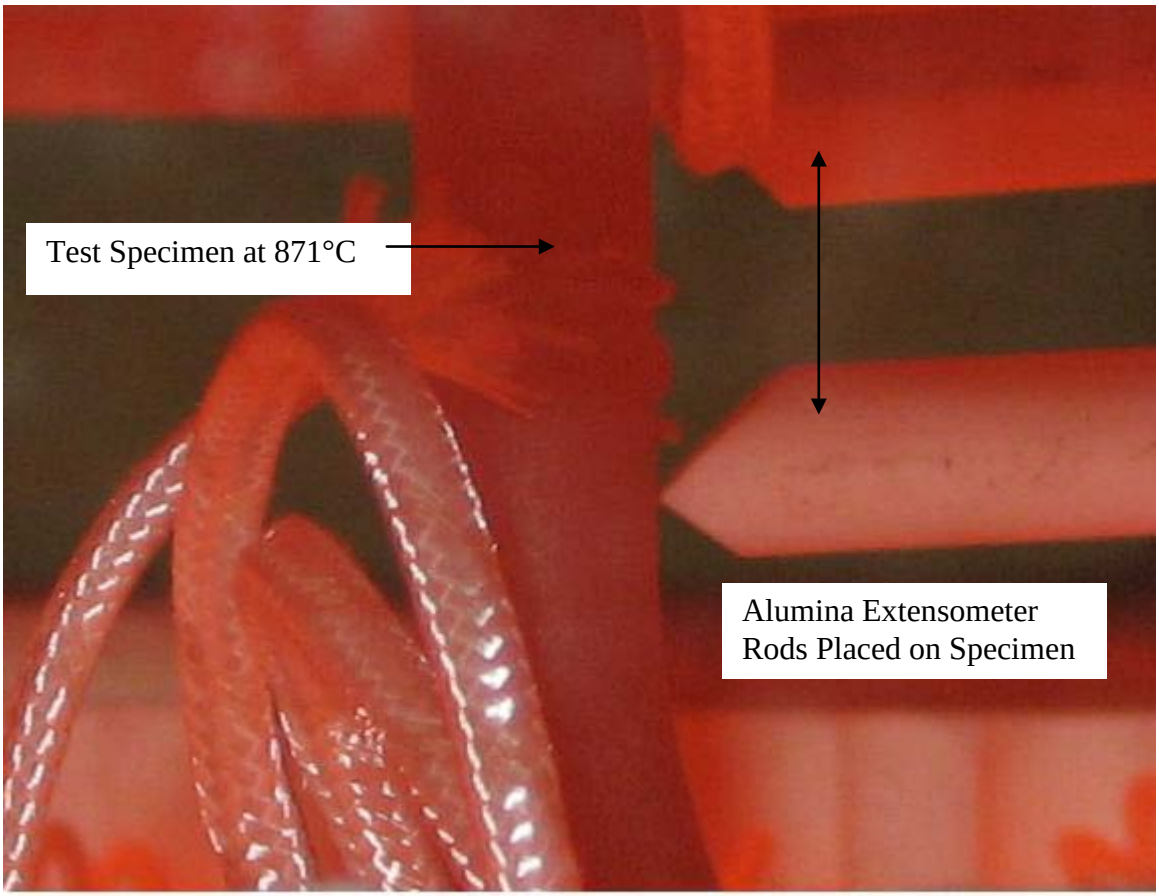

Figure 24: Test Specimen at Test Temperature with Extensometer

4.4 Chapter Summary

Each test will be configured in an identical manner with the only differences being the load profile (creep, fatigue, or both) chosen for each test. Test rig alignment will only need to be performed before the beginning of the first test.

V. Analysis and Results

5.1 Chapter Overview

This Chapter will explain the results of each test conducted during research and discuss the post test data analysis performed. Pre- and post-test microstructure analysis will also be explained.

5.2 Pre-Test Microstructure Analysis

Test specimens were taken from two slabs of PWA1484 with serial numbers of A2LPT and Z175T. It was necessary to perform a pre-test microstructure characterization of each slab. This pre-test characterization is necessary because it will provide images for comparison with the images that will be taken of the post-test microstructure. Two material samples were taken from each slab, one from each end of the material that the specimens were machined from. This was done to check that the microstructure of the test specimens did not vary in the length of the specimen. The specimens were mounted in a conductive thermosetting plastic and then polished and cleaned in preparation for SEM imaging. Six images were taken of each specimen. The specimen was divided into six imaginary segments and each image was taken in a different segment of the specimen. Figures 25 and 26 are examples of the images that were taken. The images were taken at a magnification of 25,000x using a 15.0kV beam with a spot size of 4.5 and a 30 micron aperture. The distance between the electron source and the specimen is the working distance of the image and a distance of 10±1mm was used for all images. Image Pro image correlation software was used to determine the

pre-test volume fraction of the gamma prime precipitates. Through examination of Figures 25 and 26, it can be seen that the pre-test gamma prime precipitates are cuboidal and uniform in the gamma matrix. It can be seen that the gamma prime precipitates of the A slab are noticeably larger than the Z slab. This also corresponds to wider gamma channels in between the gamma prime precipitates in the A slab. Research suggests that this will have an effect on the creep performance of the material, and this will be discussed later in the test results section [22].

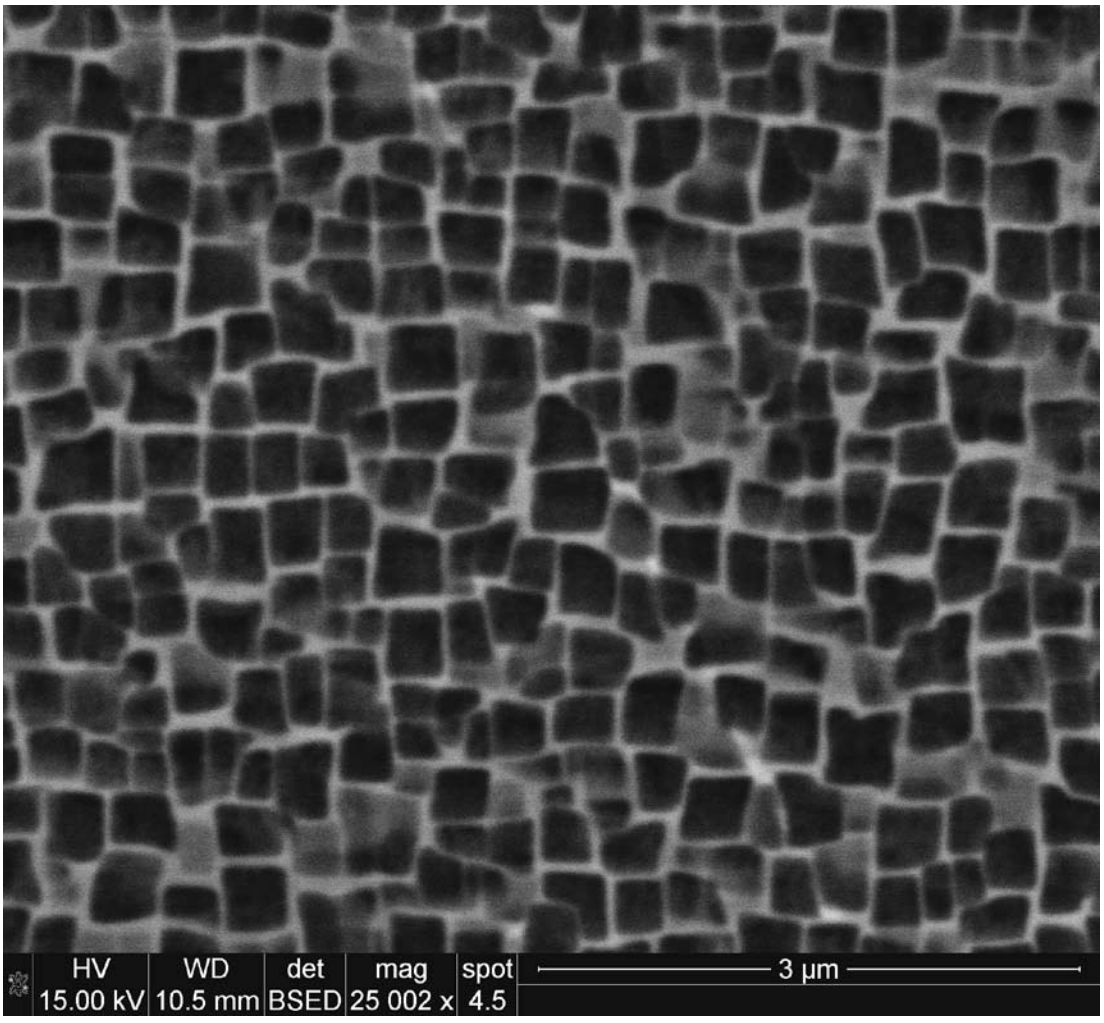

Figure 25: Image #1 of Slab Z175T Pre Test Microstructure

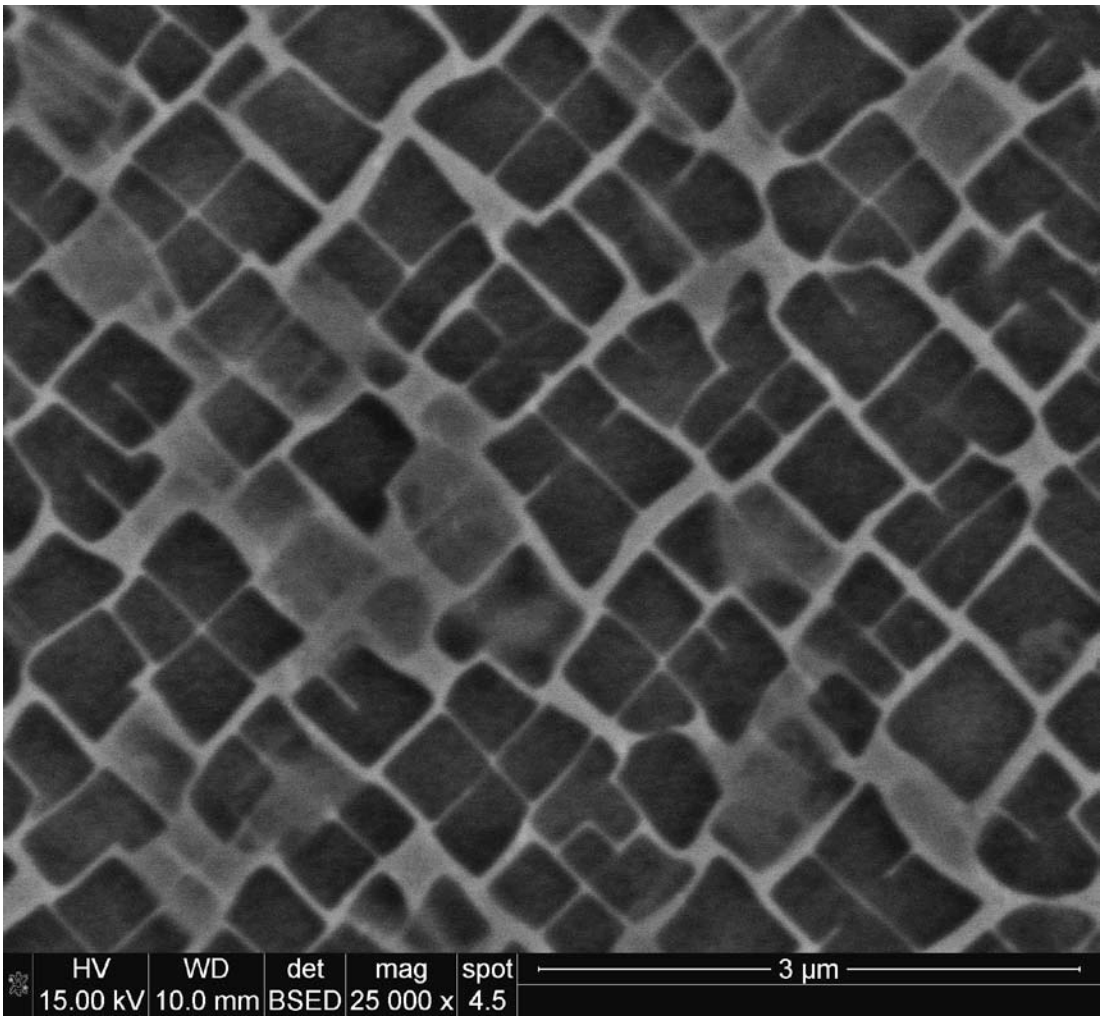

Figure 26: Image of A2LPT Pre Test Microstructure

After SEM imaging, the images were analyzed to determine the initial volume fraction of the gamma prime microstructure. The analysis software creates a binary image of the SEM image that makes gamma prime one color and the gamma channels a different color, and performs the image analysis on the binary image. Figure 27 is an example of a binary image.

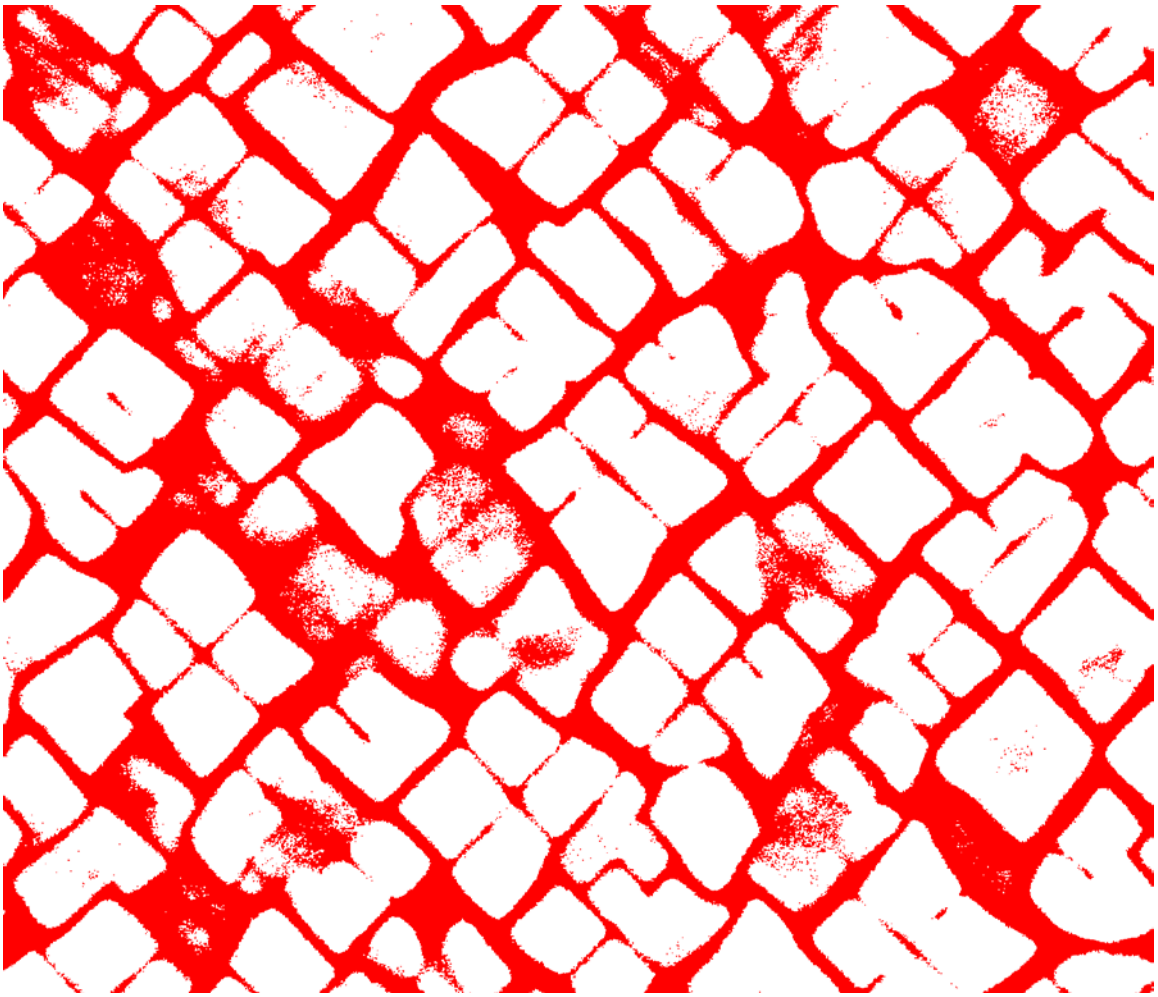

Figure 27: Binary Image of A2LPT Microstructure

The volume fraction of gamma prime in both slabs was determined to be about 67%. Simple statistical calculations were performed in order to determine the gamma prime precipitate size distribution of each plate of material. This size distribution can be illustrated in the form of a probability density function. This function is represented by the equation

$$f(x;\mu,\sigma) = \frac{1}{\sqrt{2\pi}\sigma} e^{-\left(\frac{(x-\mu)^2}{2\sigma^2}\right)} \qquad (44)$$

In which x is the measured size of a gamma prime precipitate, μ represents the mean of all of the measurements, and σ represents the standard deviation of the measurements. Graphically, this equation takes on the form of Figure 28 which is the gamma prime size distribution of plate Z175T.

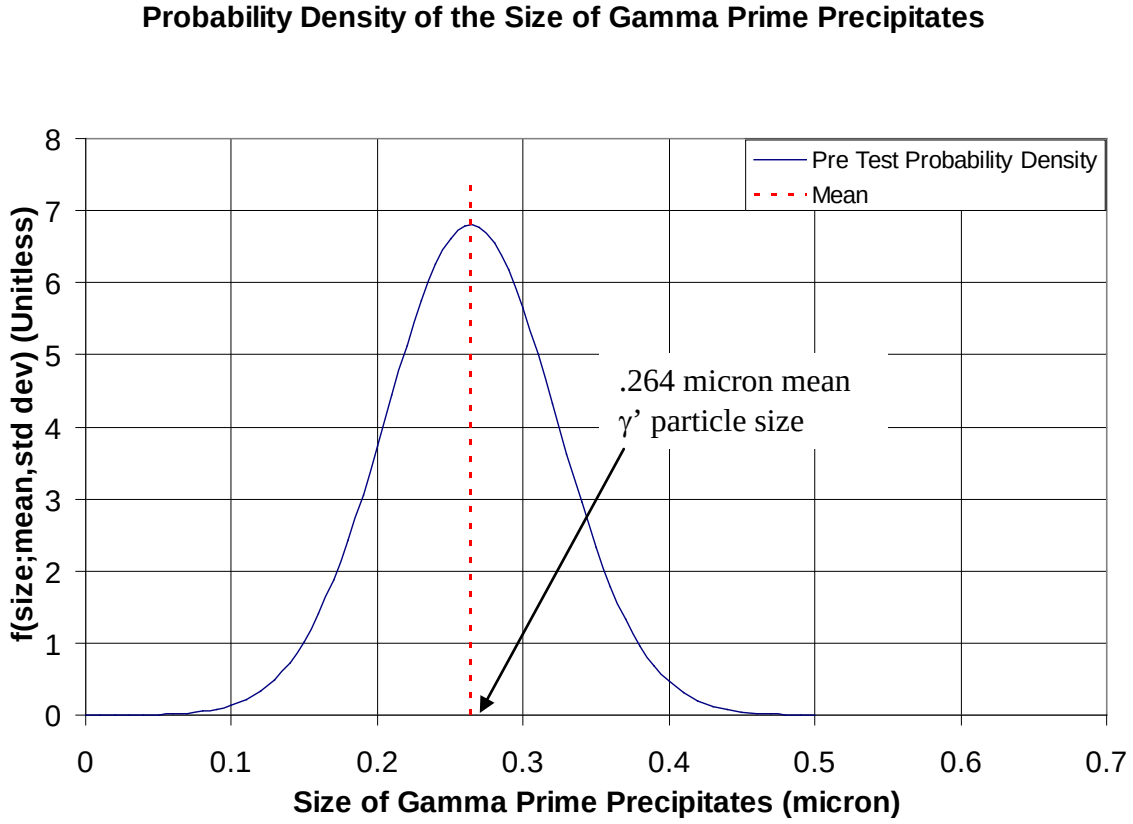

Figure 28: Probability Density Function for Gamma Prime Size of the Z175T Plate

Figure 29 is the size distribution of the gamma prime particles in the A2LPT plate of material.

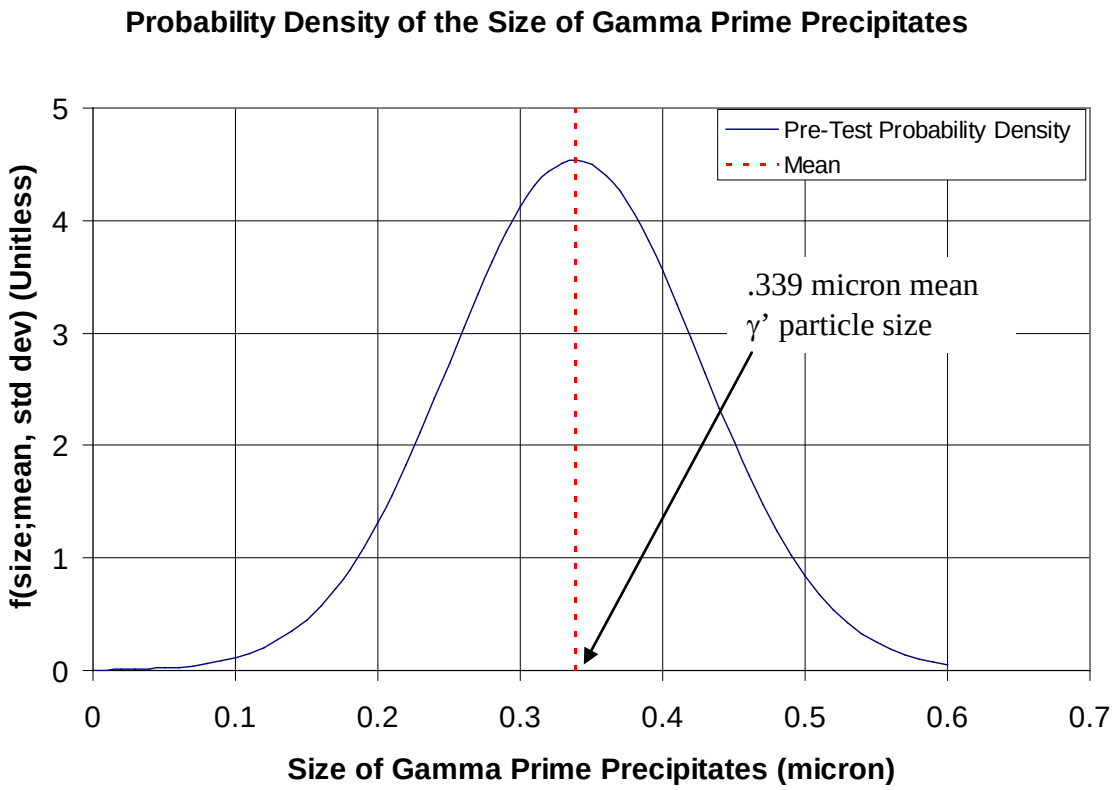

Figure 29: Probability Density Function for Gamma Prime Size of the A2LPT Plate

The A2LPT plate of material had a mean γ' particle size of .339 microns. The definite integral of both of these probability density functions represents the probability that the gamma prime precipitate sizes will be in between the bounds of the integral function.

5.3 Experimental Results and Observations

The first test performed used Test Condition #1 and was a fatigue test that was run to failure on specimen 09-144. The test ran for 98.2 hours and the specimen failed at 176,824 cycles. This number of cycles was subsequently used as a value for N_f to be used in Test Condition #3. Modulus of elasticity values were calculated at specific cycles by using hysteresis loop data collected during testing. The hysteresis loops consist of 200 data points collected during one fatigue cycle during testing. Hysteresis loops were collected at specified cycle numbers during each fatigue test. The modulus of elasticity was calculated from a hysteresis loop by using the data points in the tensile stress region of the hysteresis loop and performing a linear fit of the data points. Figure 30 is an example of the hysteresis loops collected during testing.

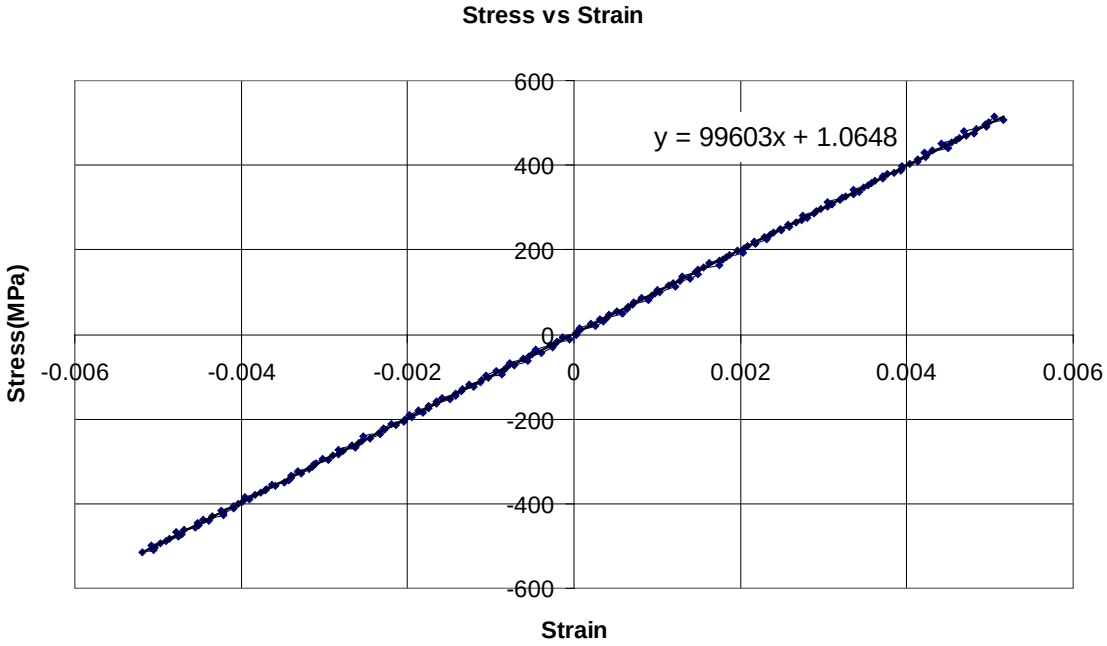

Figure 30: Example Hysteresis Loop

The modulus of elasticity decreased during Test #1 as a result of fatigue cycling. It was noted that the modulus of elasticity decreased by about 5GPa before the specimen failed. This softening of the material began after 20,000 cycles and continued at an increasing rate until specimen failure. This decrease in modulus is an indication of microstructural damage occurring inside the material in the form of voids and micro-cracking. Figure 31 illustrates the softening that occurred in the specimen during testing.

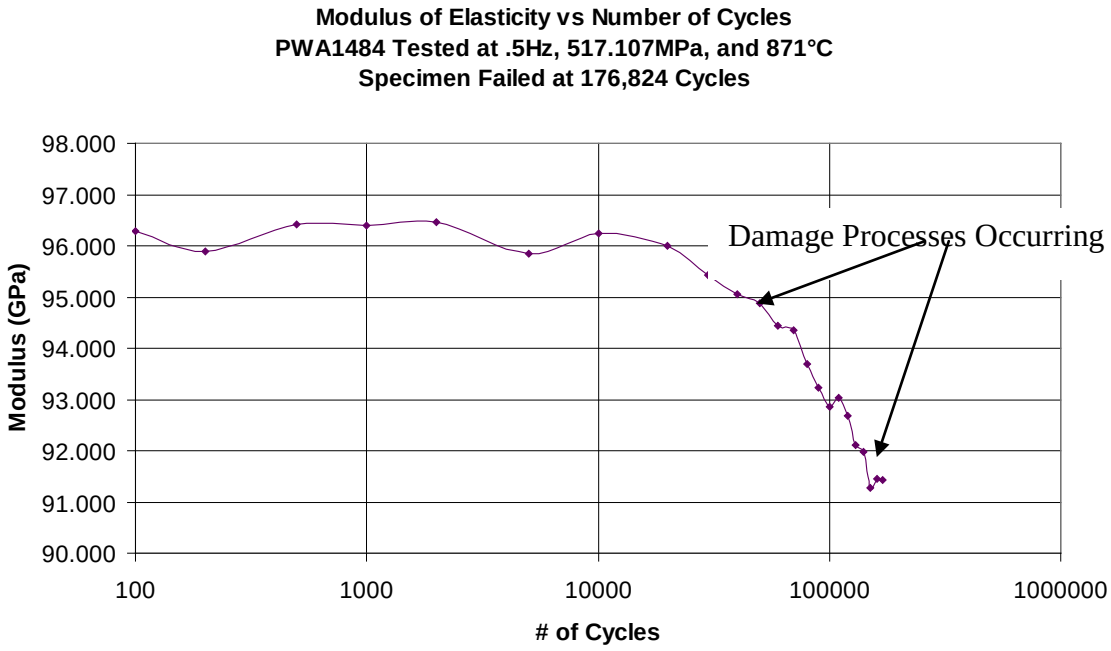

Figure 31: Test #1: 09-144 Modulus Tracking

The second test that was conducted was a creep test to 5% creep strain at a load of 517MPa and a temperature of 871°C using specimen 09-150. This specimen took 38.16 hours to reach 5% creep strain. Figures 32 and 33 are plots of time vs. % creep strain of the specimen. From examination of these Figures we see that the specimen displayed an initial increase in strain rate followed by a typical region of primary creep characterized

by a continuously decreasing strain rate until the onset of secondary creep. This initial stage of increasing strain rate is known as incubation creep, and is still not completely understood in PWA1484. This region is highlighted in Figure 32. There was a region of primary creep of about 3.25% during the first four hours of creep before transitioning to a region of secondary creep from 4 hours to the end of the test at 38.16 hours.

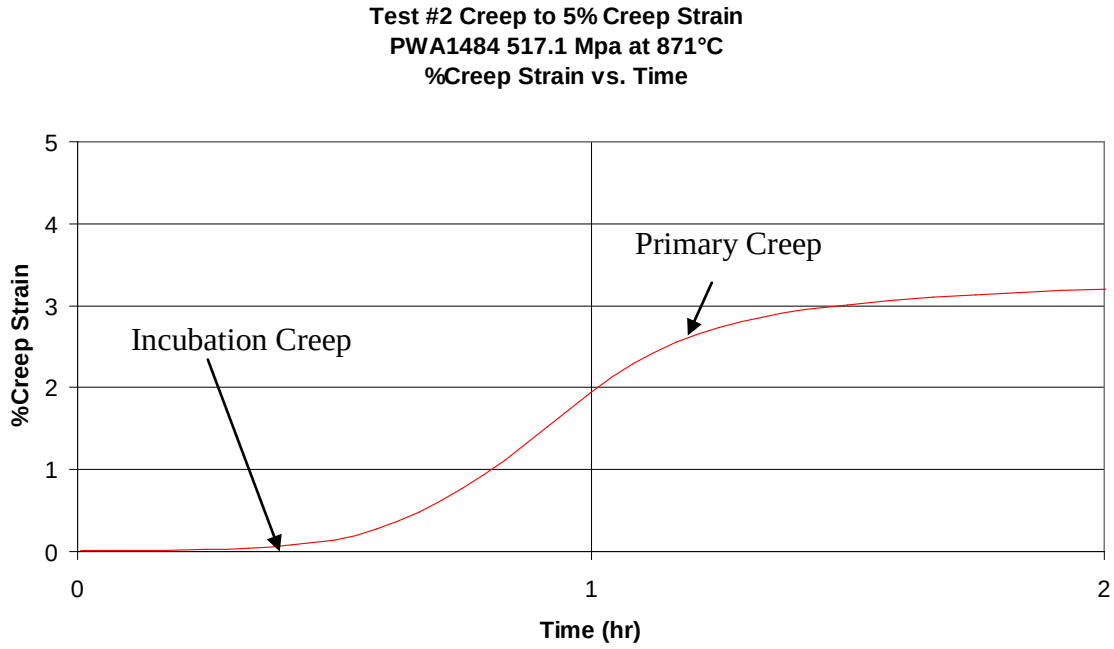

Figure 32: Test #2: 09-150 Initial Region of Increasing Creep Strain Rate

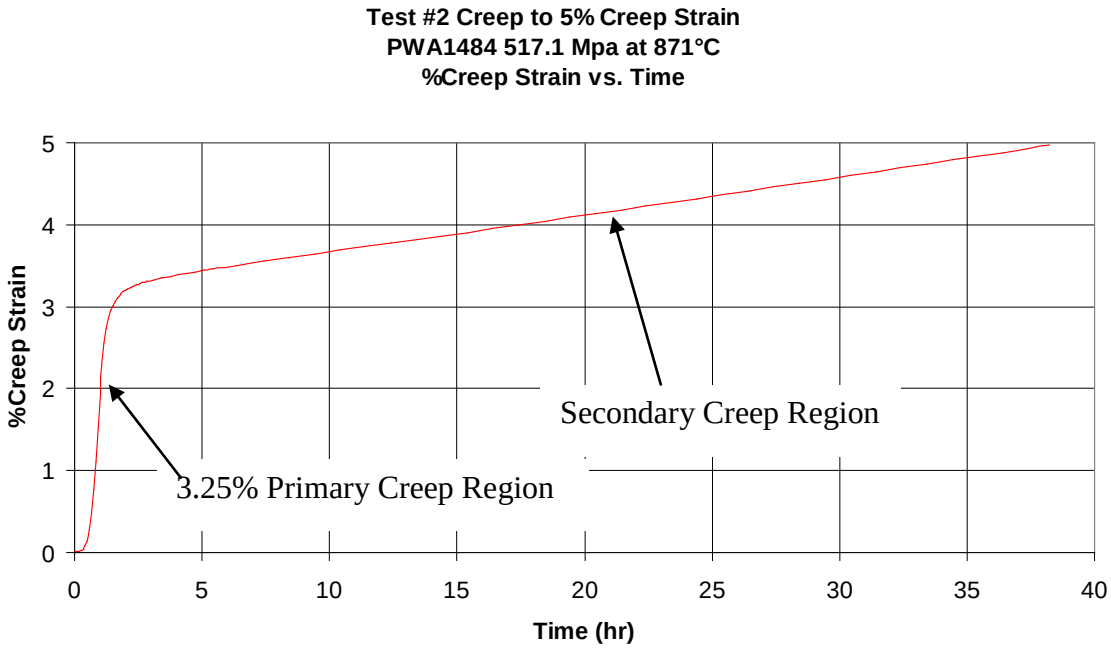

Figure 33: Test #2: 09-150 Creep to 5% Creep Strain

Figure 34 is a plot of the strain rate vs. % creep strain of test number 2. In this Figure, the incubation creep is represented by the initial increase in strain rate up to the maximum strain rate, the primary region of creep is represented by the decreasing strain rate after the maximum strain rate is reached, and the secondary region of creep is represented by the straight line, constant strain rate portion of the plot. Figure 34 illustrates the large region of primary creep and the region of secondary creep for the rest of the test. It can also be seen from Figure 34 that the specimen did not enter the tertiary creep regime by the time it reached 5% creep strain.

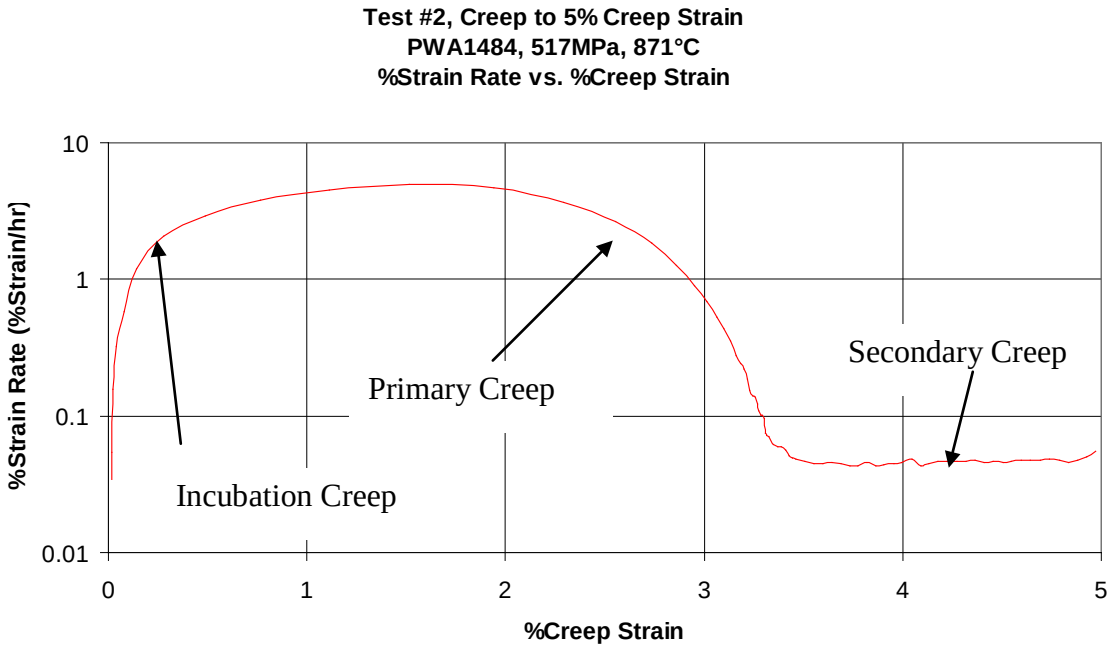

Figure 34: Test #2: 09-150 %Creep Strain vs. %Strain Rate

Test #3 was a fatigue test that was run to approximately .5N_f, then transitioned to a creep test and allowed to creep to 5% creep strain, using specimen 09-148. Figure 35 is a plot of # of fatigue cycles vs. modulus of elasticity of the specimen. Of note in Figure 35 is the softening that occurred during the fatigue loading of the specimen. Again, this occurred after 20,000 cycles and is an indication of damage processes occurring as a result of the fatigue loading.

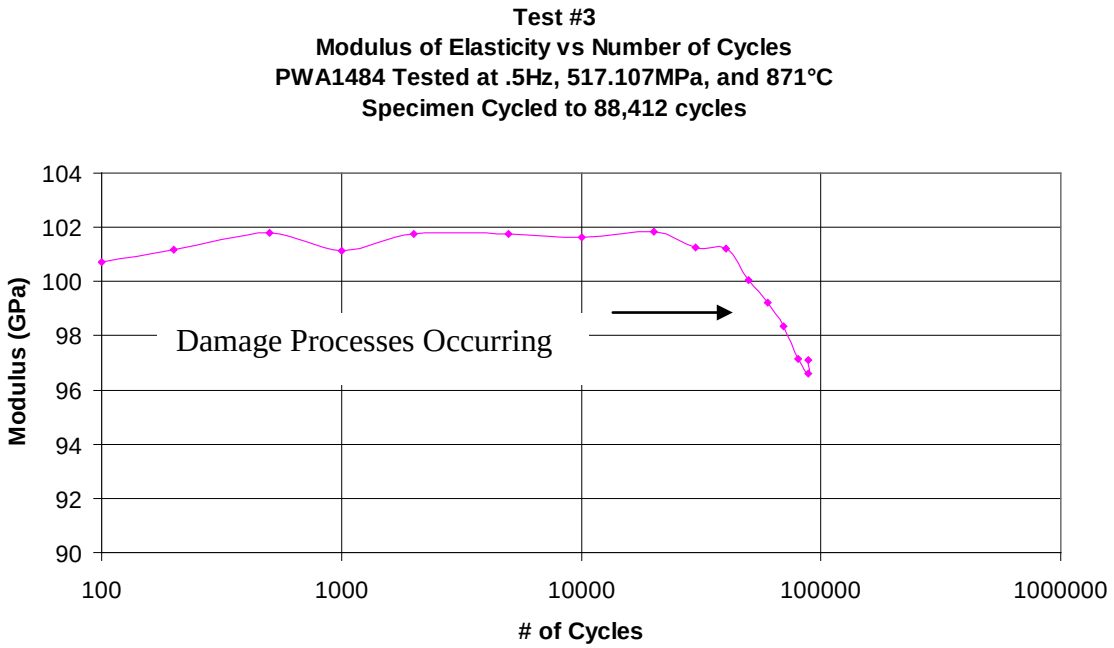

Figure 35: Test #3: 09-148 Modulus Tracking for Fatigue loading to .5Nf

Figure 36 is the time vs. %creep strain for Test #3. It can be noted looking at this plot that creep after fatigue had a significantly smaller region of primary creep of about 1.3%. The time to 5% creep strain was also significantly longer, taking 72.5 hours to reach 5%, but as the specimen neared 5% creep strain, the strain rate begins to increase and the specimen transitions from a secondary creep behavior to a tertiary creep behavior. This is further evidence that damage processes are occurring during the fatigue cycling that result in a transition to tertiary creep that begins before the specimen from test #2, since tertiary creep occurs as a result of the growth of voids in the material. As a result of this transition to tertiary creep, it can be seen that the specimen with the prior fatigue loading most likely would have ruptured before the specimen that was only subjected to creep loading had the specimens been allowed to proceed to creep to rupture.

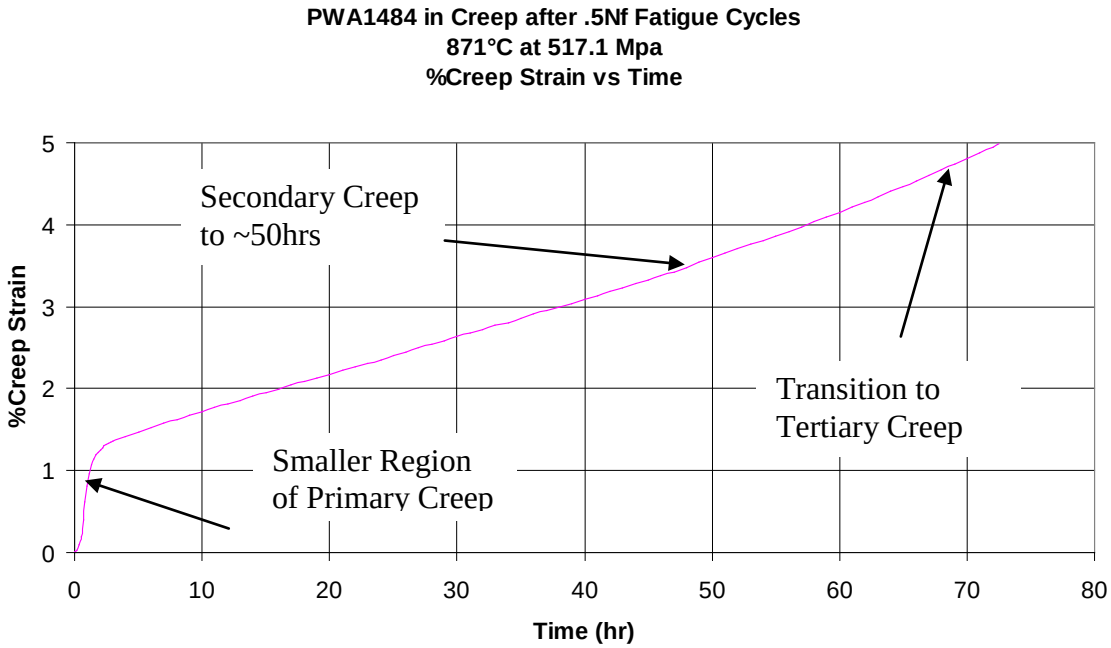

Figure 36: Test #3: 09-148 Creep After .5Nf Fatigue Cycles

The smaller region of primary creep strain and longer secondary creep is illustrated in Figure 37 which is a plot of the % creep strain vs. the creep strain rate. The tertiary creep regime is also evident as the %creep strain reaches 5% because of the increasing strain rate of the specimen compared to the constant secondary strain rate.

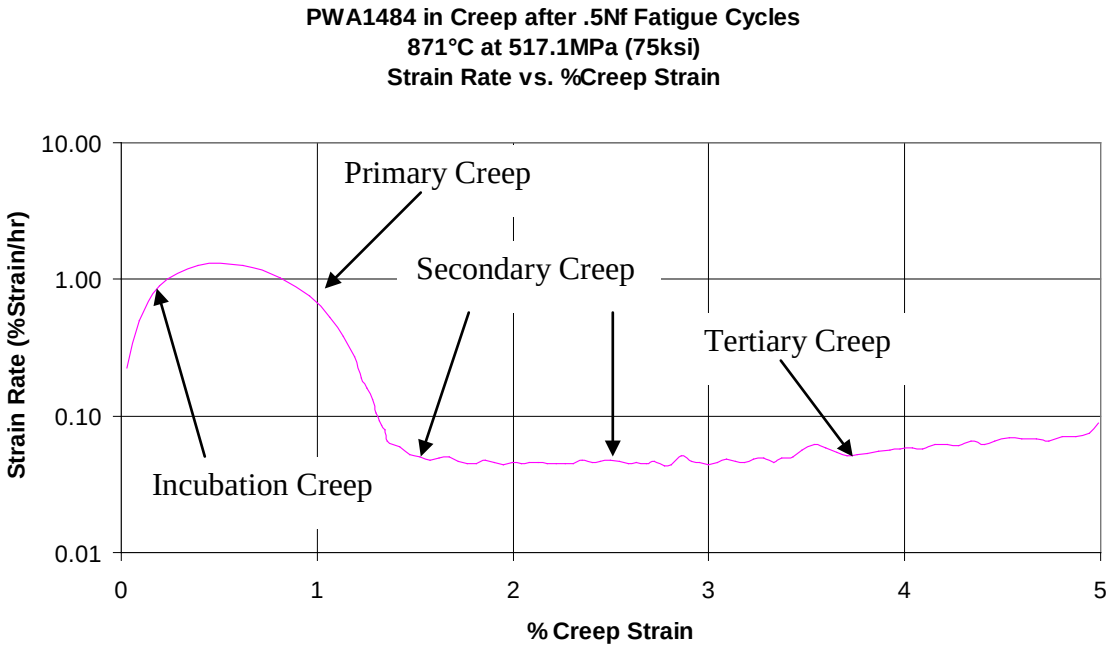

Figure 37: Test #3: 09-148 %Creep Strain vs. %Strain Rate

Test #4 was a creep test to 2.5% that was then transitioned to fatigue loading and cycled to failure, using specimen 09-149. The specimen reached 2.5% creep strain in 1.2 hours, and failed in fatigue at 115,251 cycles. Figure 38 is a plot of %creep strain vs. time. In this Figure, one can note that the initial incubation creep region was present, the specimen did not reach secondary creep, and that the creep behavior of this specimen is nearly identical to the specimen from Test #2.

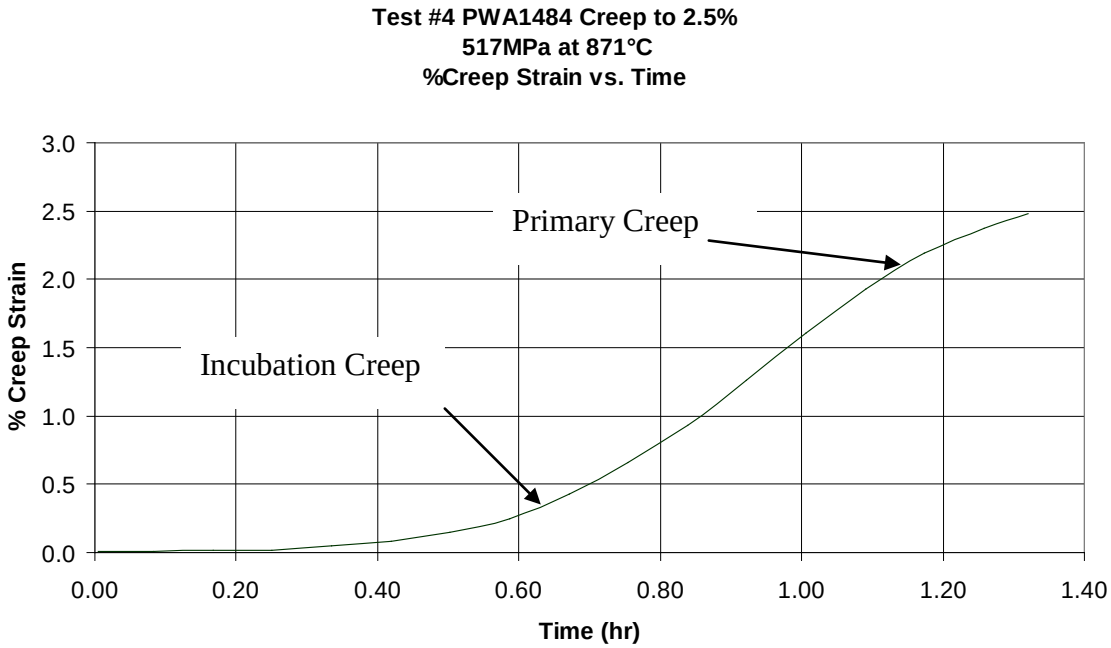

Figure 38: Test #4: 09-149, Creep Strain to 2.5% Before Fatigue Loading

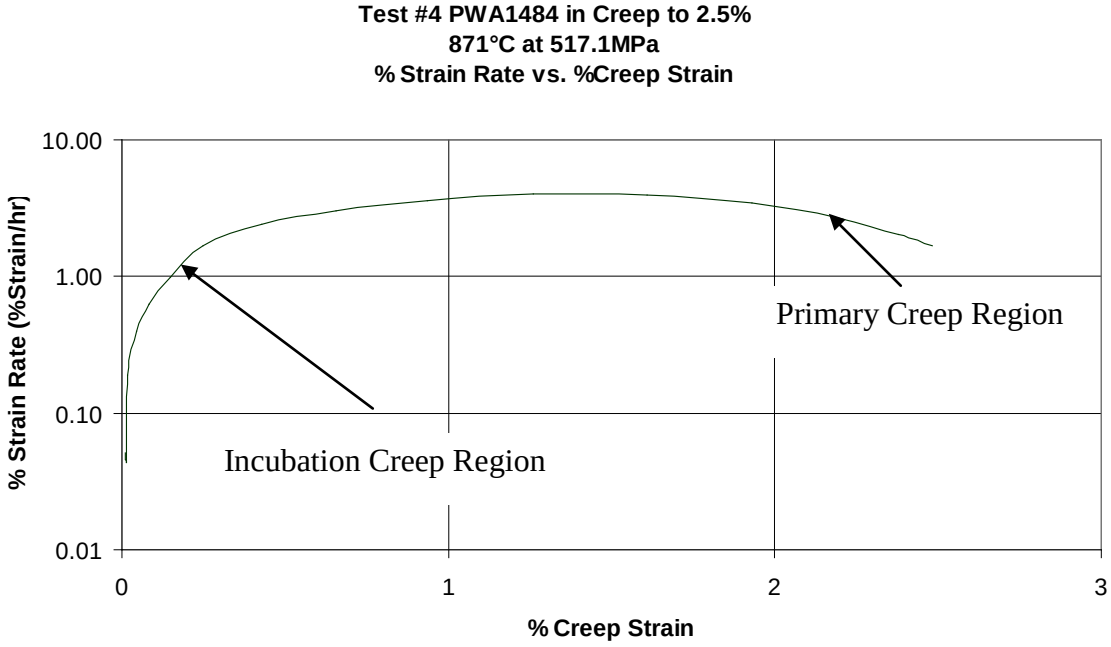

Figure 39: Test #4: 09-149 %Strain Rate vs. %Creep Strain

Figure 40 shows the modulus vs. fatigue cycles. The fatigue behavior of the specimen from Test #4 progressed in the same manner as the previous fatigue tests with the only difference being the modulus evolution at the beginning of the test. It can be observed that the modulus begins at lower level than the fatigue specimens that did not undergo prior creep, Test #4 exhibits an initial hardening followed by a faster decline of 4GPa between 200 and 1000 cycles. Disregarding the lower initial modulus and the rapid decline of the modulus in between 200 and 1000 cycles, the modulus of elasticity vs. # of cycles curve displays the same shape and overall behavior as the other four fatigue specimens. This indicates that there was not a large amount of microstructural damage accumulated during the initial creep to 2.5% creep strain. This follows with previous research done on PWA1484 that has established that primary and secondary creep are dislocation driven processes, and damage does not play a major role until the tertiary creep regime [14]. With this being the case, a change in crystal orientation is the most likely cause for the decrease in the modulus prior to 10,000 cycles. It is well known that a slight change in crystal orientation of PWA1484 will have a large effect on the modulus of elasticity of the material [1]. The initial creeping of the material served to move the crystal orientation closer to a <001> orientation, causing the initial lowering of the modulus of elasticity during fatigue. After this initial lowering of the modulus, the fatigue proceeded in a normal fashion, with much of the fatigue damage occurring after 20,000 cycles.

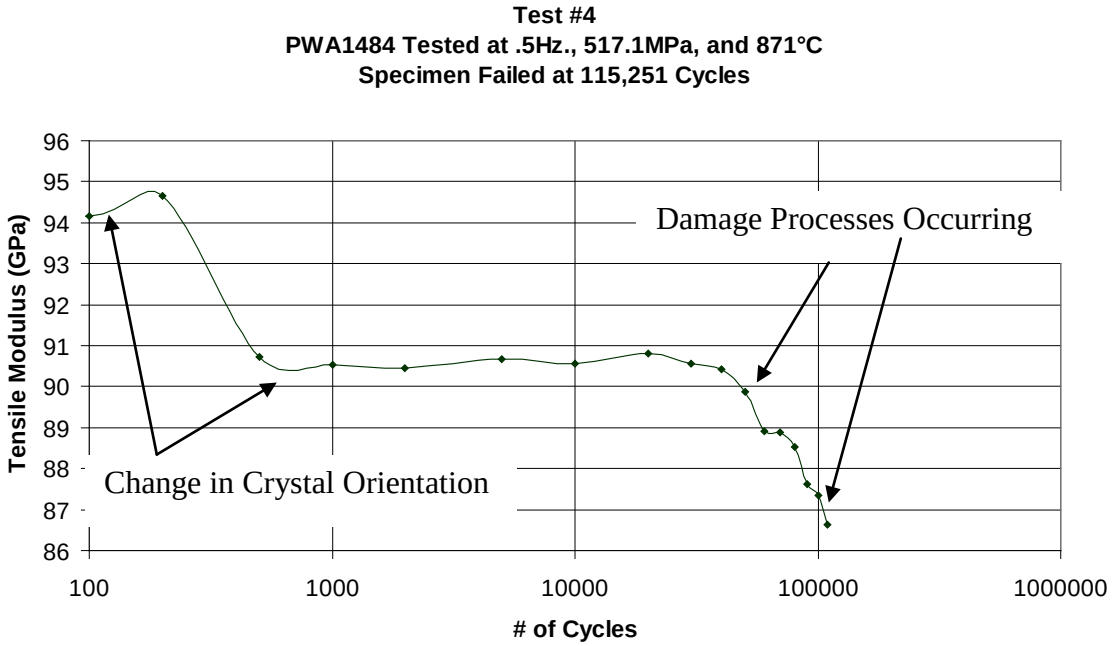

Figure 40: Test #4: 09-149 Fatigue after 2.5% Creep Strain

Two additional tests were run to supplement the data gained from tests 1-4. To assess plate to plate creep variability, an additional creep test was conducted on specimen 09-146 from the A2LPT plate. This test was conducted in pure creep to 5% creep strain at 517MPa and 871°C. To further establish the effect of prior fatigue on creep behavior, an additional fatigue then creep test was conducted on specimen 09-152 that involved fatiguing the specimen to ~.25N_f then transitioning to pure creep to 5% creep strain. Figure 41 is a comparison of the %creep strain vs. time for test number 2, the creep test to 5% creep strain, and test number 3, the fatigue to .5 N_f then creep to 5% creep strain, the additional creep test on specimen 09-146, and the additional test of fatigue to .25N_f then creep to 5% creep strain on specimen 09-152. Note the large difference in primary creep strain and the uniform secondary creep strain rate of the four specimens.

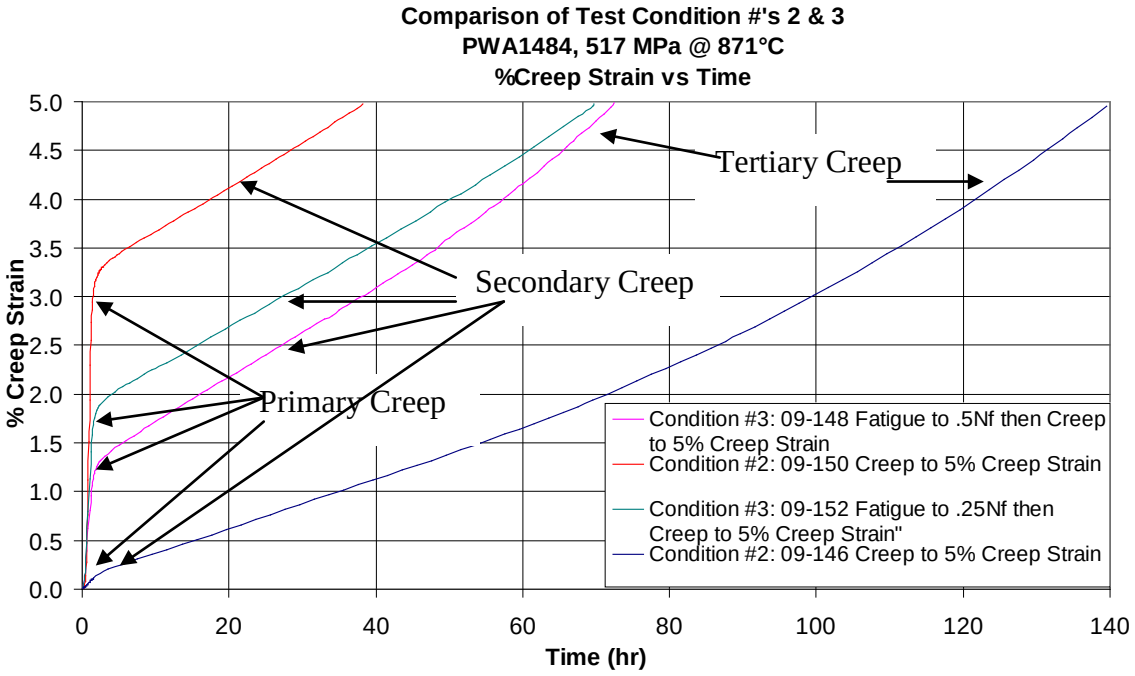

Figure 41: Comparison of Test #2 and #3, Time vs. %Creep Strain

The reason for this plate to plate variation of primary creep is not completely understood. One reason could have been the larger size of the gamma prime precipitates, indicating lower coherency at the gamma/gamma prime interface, and slightly wider gamma channels that were present in the A2LPT plate as compared to the Z175T plate [22].

Figure number 42 is a plot of modulus tracking for each fatigue specimen. Through examination of these plots it can be seen that the fatigue life of all of the fatigue specimens cycled to failure (not test #3) was centered around 10^5 cycles to failure. It can also be seen that the softening before failure was consistently close to 5GPa. Test #4 exhibited a lower starting modulus and a sharp drop in modulus by cycle 1000. The results indicate that prior creep resulting in a %creep strain of 2.5% does not significantly

impact the fatigue performance of PWA1484, as fatigue scatter is usually a factor of 2 in most materials.

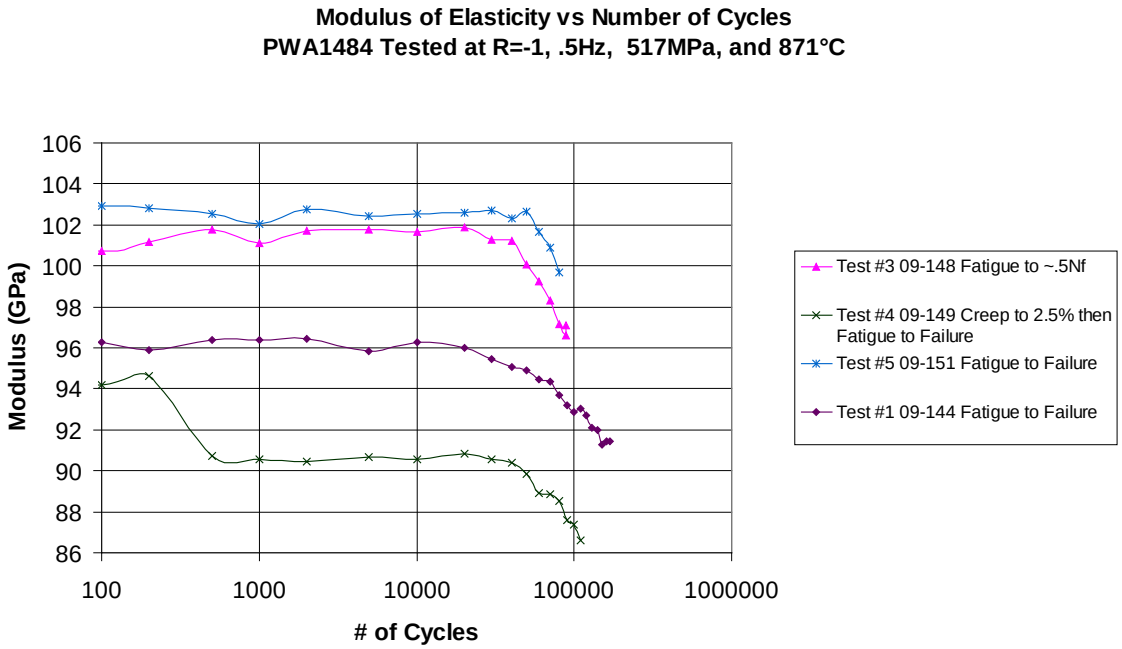

Figure 42: Modulus of Elasticity vs. Number of Cycles for Each Fatigue Experiment

5.4 Post-Test Microstructure Analysis

After each test was completed, a sample from the test specimen was cut from the specimen and mounted in a conductive thermosetting plastic and polished for scanning electron microscope image analysis. For the creep specimens that did not fracture during testing, a cylinder of material was cut from the center of the specimen. The cylinder of material was then sectioned in such a way that allowed analysis of the specimen along the axis that was parallel to the applied stress and the axis that was perpendicular to the applied stress. For the fatigue specimens that fractured during testing, a cylinder of

material was taken out just below the fracture surface and sectioned so that analysis could be performed on the axis parallel to the applied stress and the axis perpendicular to the applied stress. The way that the specimens were sectioned is illustrated in Figure 43.

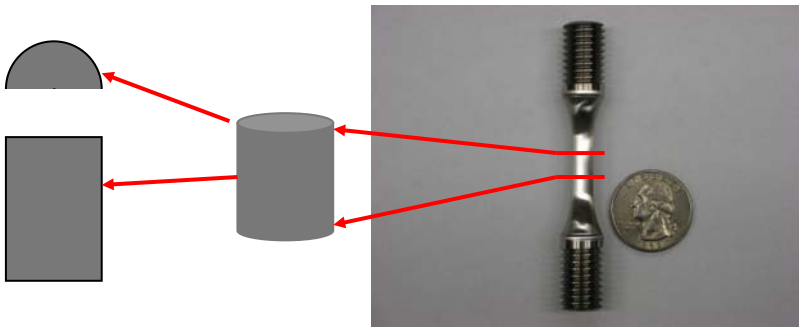

Figure 43: Illustration of Material Extraction for SEM Analysis

During our discussion of the morphology of the gamma prime microstructure of the material during testing, we will use terminology to describe the shape of the gamma prime particles that is illustrated in figure 44 from work performed by Grosdidier [21].

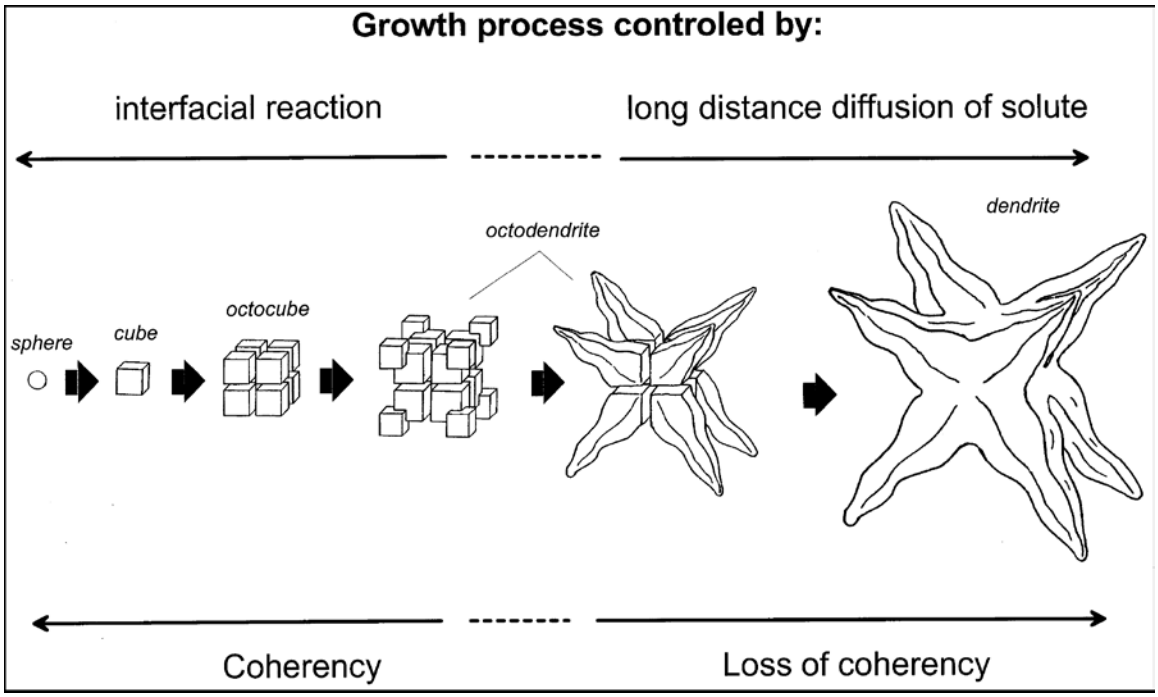

Figure 44: Description of Growth and Coherency of Gamma Prime Particles [21]

5.4.1 Test #1: Fatigue to Failure SEM Analysis

The microstructure after fatigue to failure exhibited growth of the gamma prime precipitates that could be viewed both parallel and perpendicular to the applied stress axis. Figure 45 is an image of the post-test microstructure perpendicular to the stress axis of a specimen cycled in fatigue until failure. Comparison of this figure to the pre-test microstructure figure above, it can be seen that there has been significant growth in the size of the gamma prime precipitates. The precipitates also appear to have a more rounded shape overall, with some of them growing into an octodendrite shape, indicating a loss of coherency of the gamma prime precipitates [21]. This loss of coherency and change of shape of the gamma prime precipitates is an indication of damage occurring during fatigue loading.

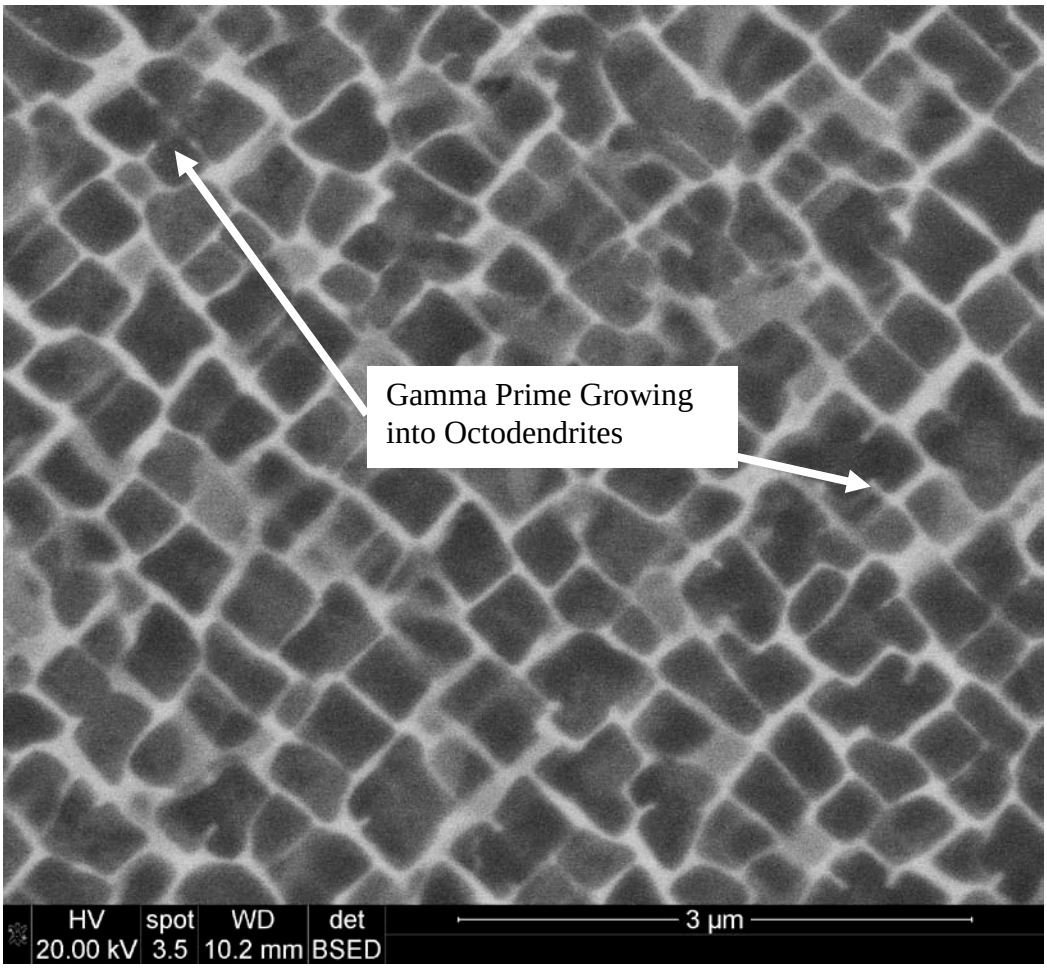

Figure 45: Test #1 Post-Test Microstructure, Perpendicular to Stress Axis

In Figure 46 the microstructure is viewed parallel to the axis of applied stress. Here we see the same growth and loss of coherency of the gamma prime precipitates. It does not appear that there is a preferential type of coarsening that is occurring as some of the precipitates seem to be growing perpendicular to the applied stress and others appear to be growing parallel to the applied stress.

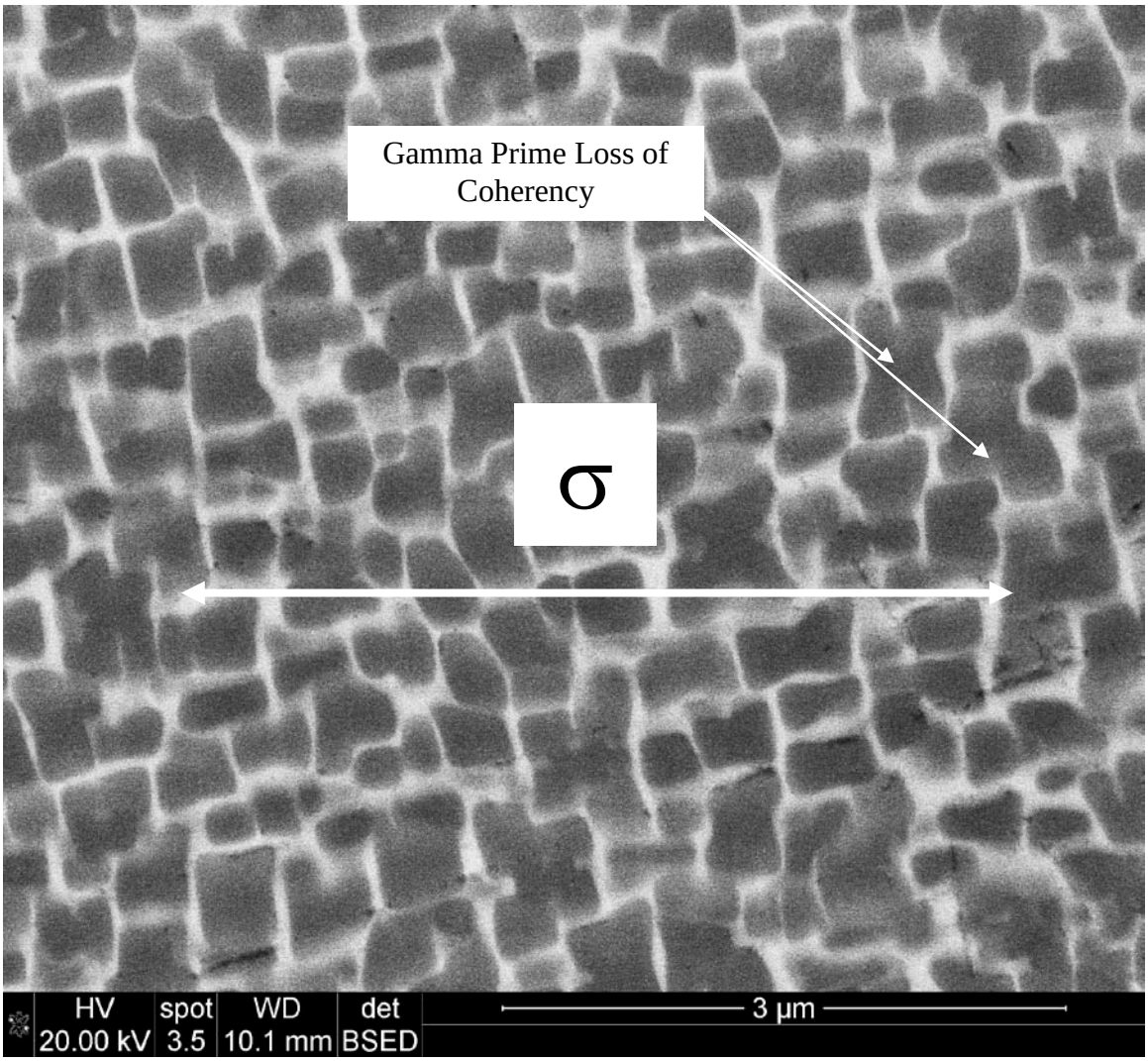

Figure 46: Test #1 Post-Test Microstructure, Parallel to the Applied Stress Axis

Figure 47 is also of the microstructure that is parallel to the direction of the applied stress from material taken from just below the fracture surface of the specimen. Figure 47 shows similar coarsening and loss of coherency of the gamma prime precipitates.

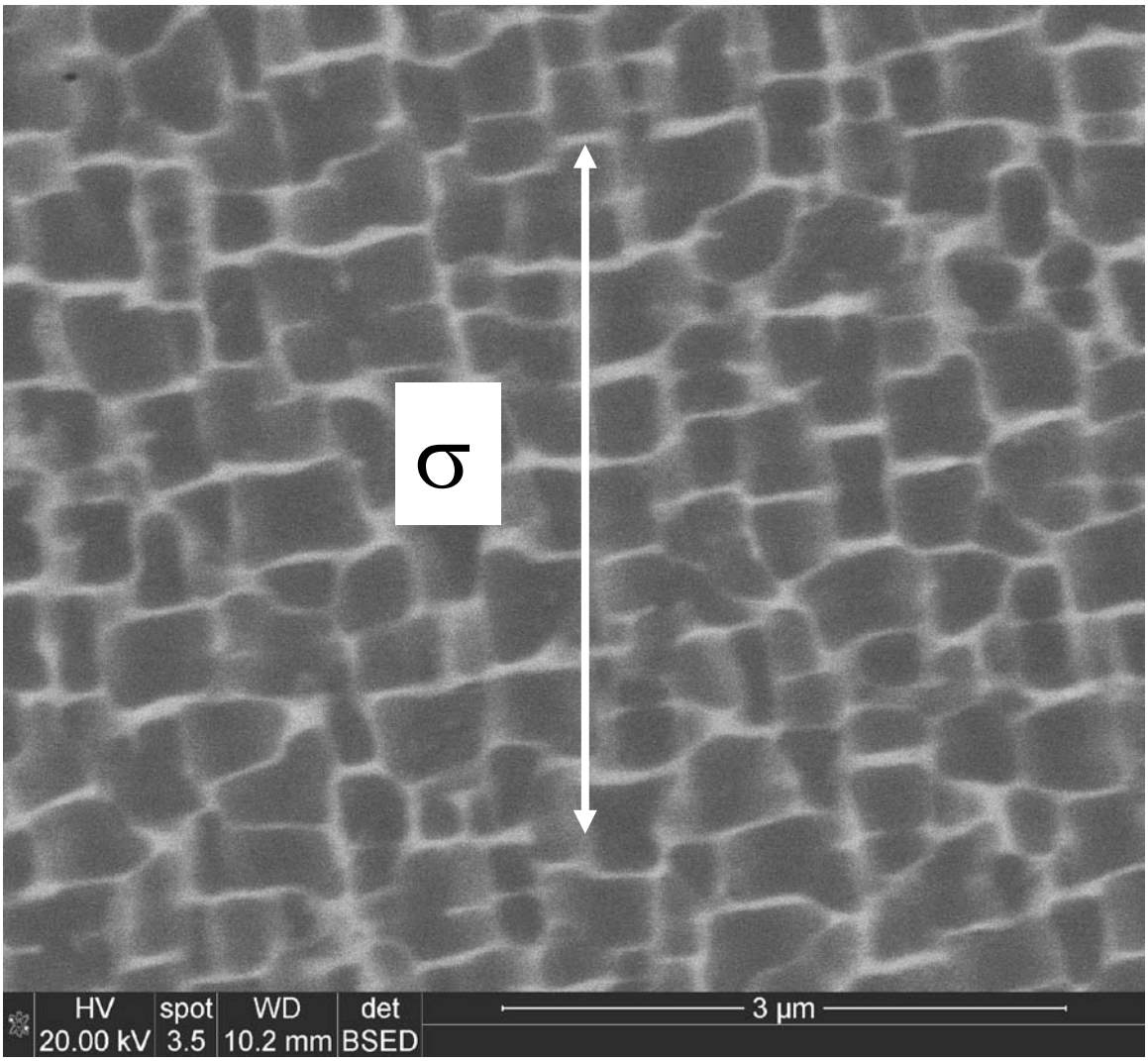

Figure 47: Test #1 Post-Test Microstructure, Parallel to the Applied Stress Axis

Post test measurements were taken of the gamma prime precipitates using Image Pro software. The post test measurements confirmed the slight growth of the gamma prime precipitates. Figure number 48 is a plot of the normal distribution of the gamma prime precipitates after Test #1 plotted with the pre-test gamma prime size distribution.

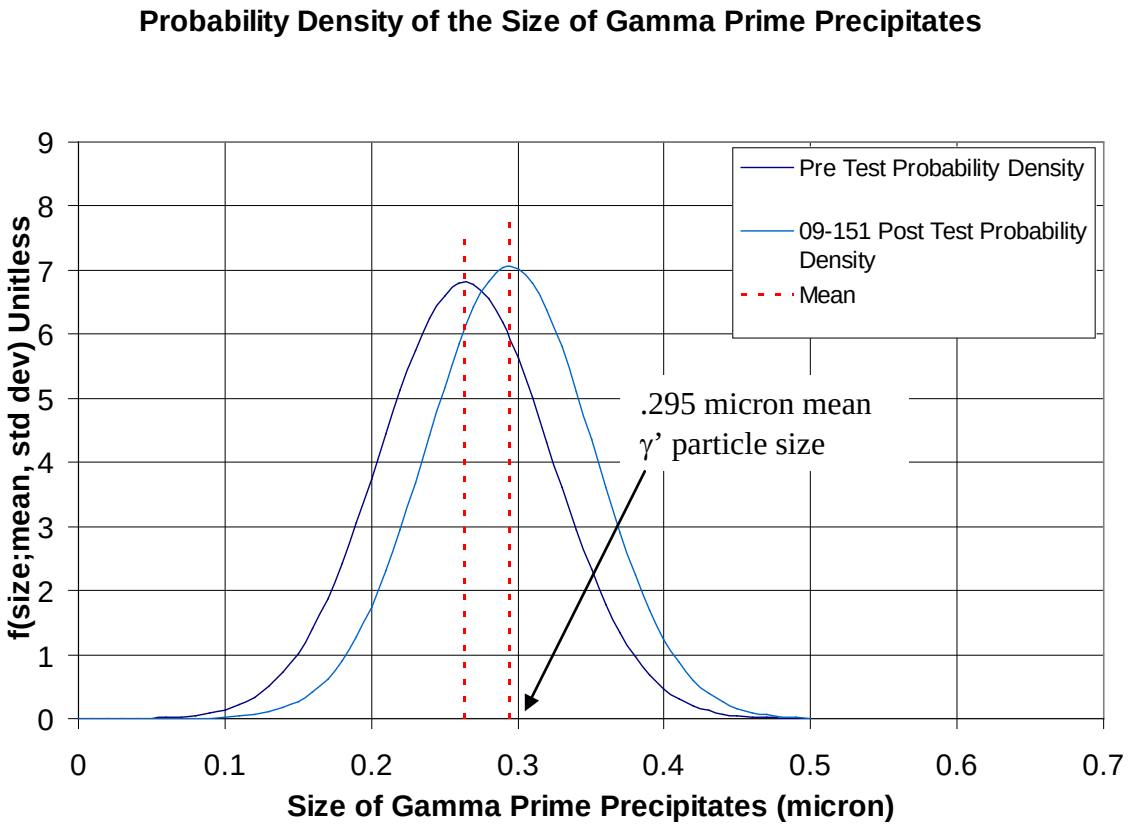

Figure 48: 09-151 Post-Test Distribution of Gamma Prime Size

5.4.2 Test#2: Creep to 5% Creep Strain Post test Microstructure Analysis

Figure 49 is an image that is perpendicular to the applied stress axis shows coarsening behavior that is similar to Test #1. We see that there has been growth of the gamma prime precipitates, and precipitate loss of coherency.

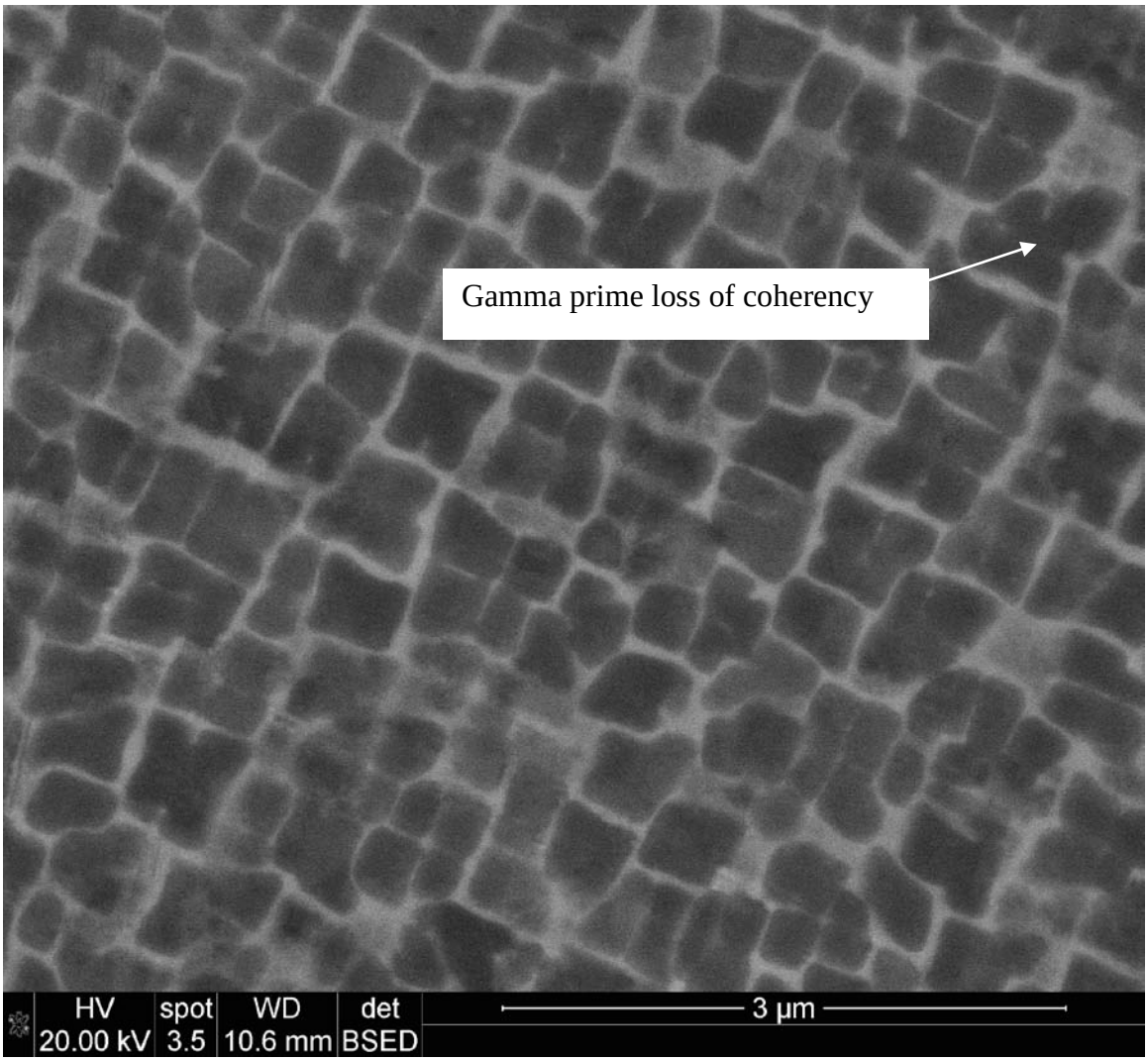

Figure 49: Test #2, Post-Test Microstructure Perpendicular to Applied Stress Axis

Figure 50 is an image of the structure parallel to the applied stress that shows microstructure that displays the same type of gamma prime changes. One difference in the view parallel to the applied stress is that the damage to the gamma prime precipitates is more pronounced with a large percentage of the precipitates having non-cuboidal shapes and many of the precipitates beginning to coalesce into even larger precipitates.

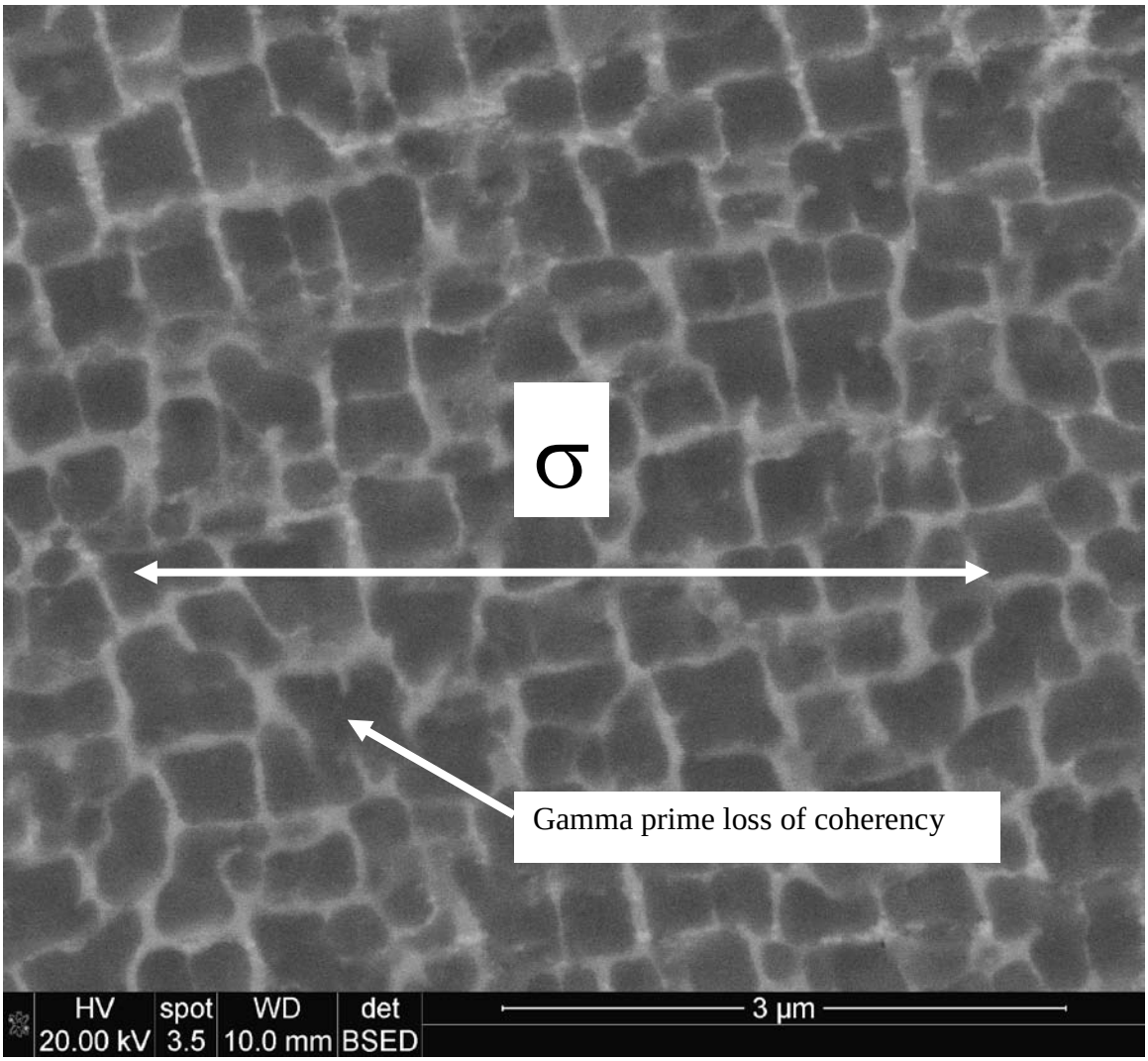

Figure 50: Test #2-Post Test Microstructure Parallel to Applied Stress Axis

The growth of the gamma prime precipitates in Test #2 was very noticeable and is illustrated in Figure #51, the post test gamma prime size distribution. From figure #51 it can also be seen that the normal distribution is larger, representing a less uniform size of gamma prime precipitates.

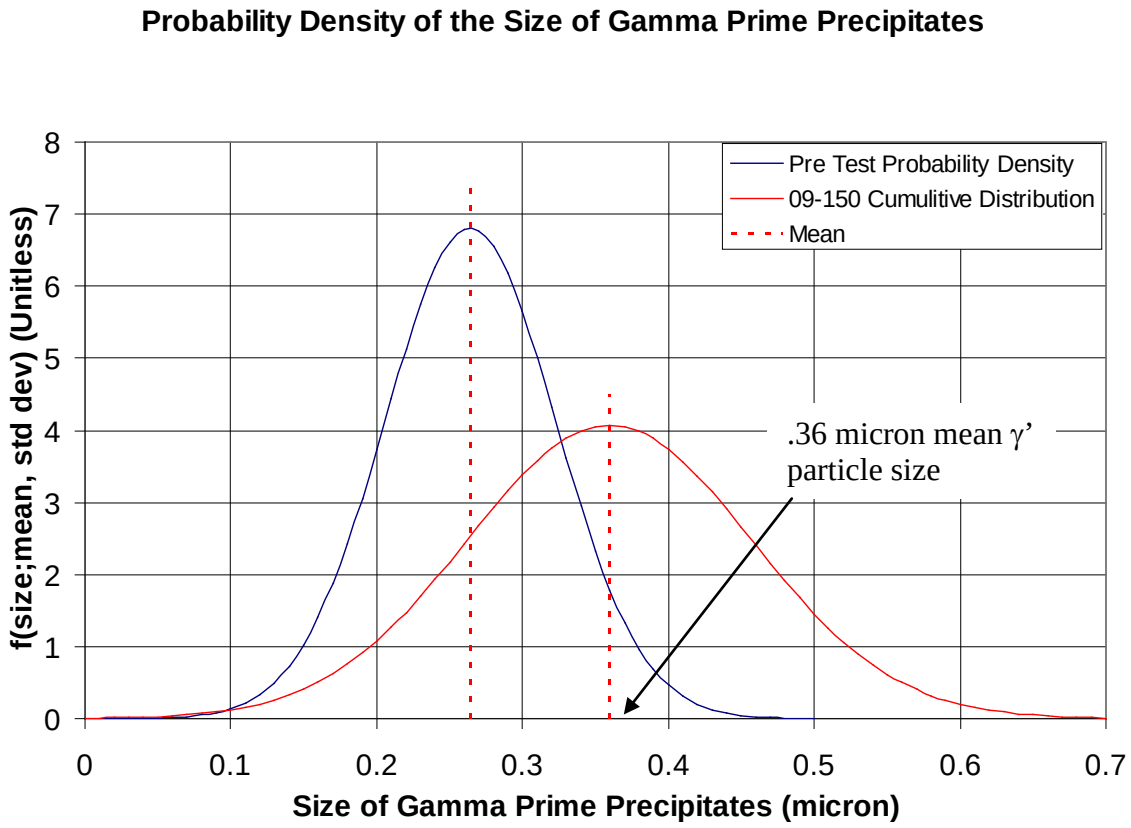

Figure 51: 09-150 Post-Test Distribution of Gamma Prime Size

5.4.3 Test#3: Fatigue to ~.5N_f Cycles then Creep to 5% Creep Strain Post-test Microstructure Analysis

Figure 52 is an image that is perpendicular to the applied stress. The gamma prime precipitates have increased in size and taken on a rounded shape with each precipitate aligned in a random way with its neighbors.

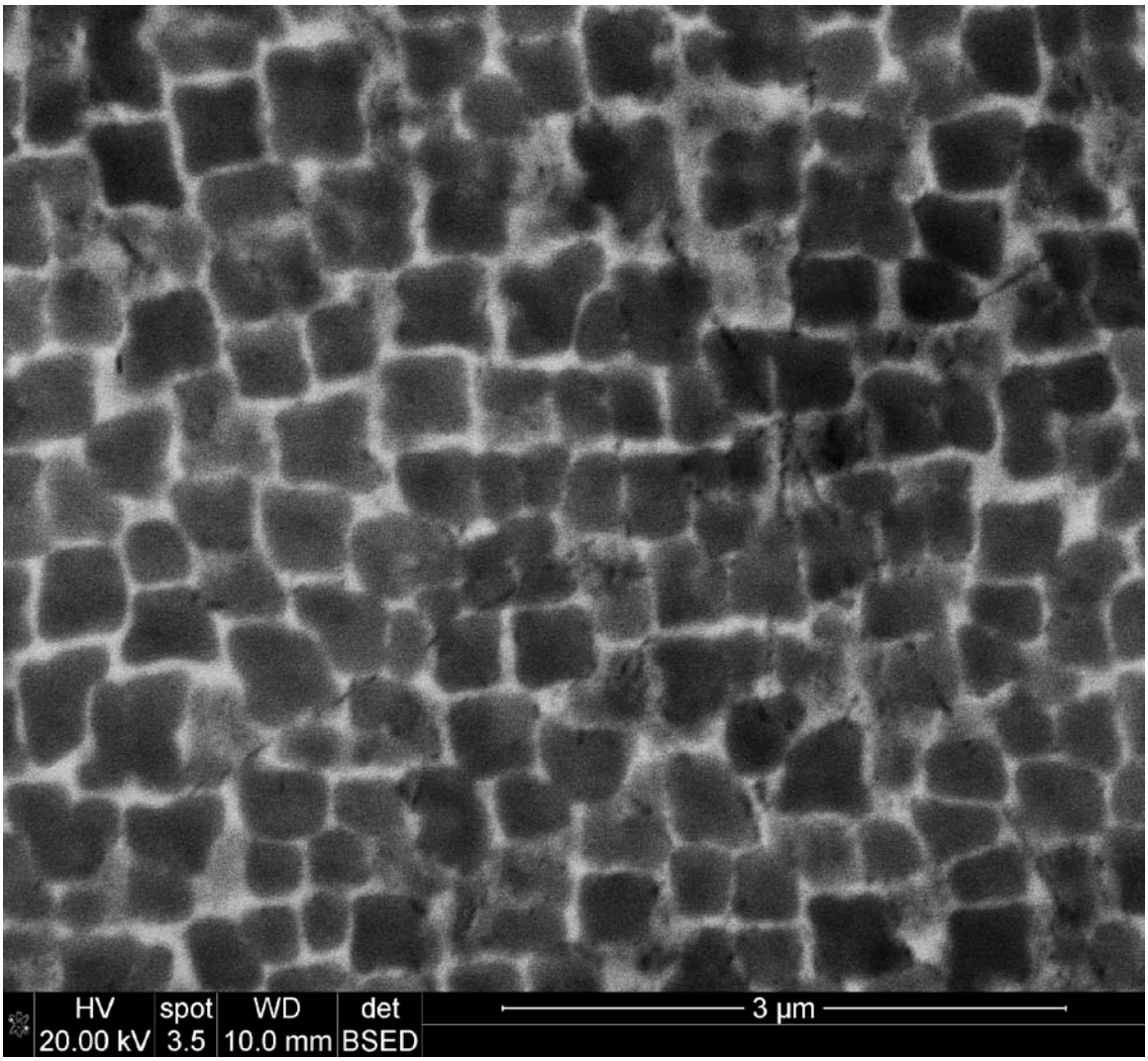

Figure 52: Test #3 Post-Test Microstructure Perpendicular to the Stress Axis

Figure 53 is an image of the microstructure parallel to the applied stress axis. From this point of view one can see obvious shape changes in the gamma prime precipitates. Some of the precipitates are coalescing and appear to be in the beginning stages of forming plate type rafts. Almost all of the gamma prime precipitates are showing a loss of coherency. This preliminary rafting behavior did not occur in Test #2 that was the creep only test.

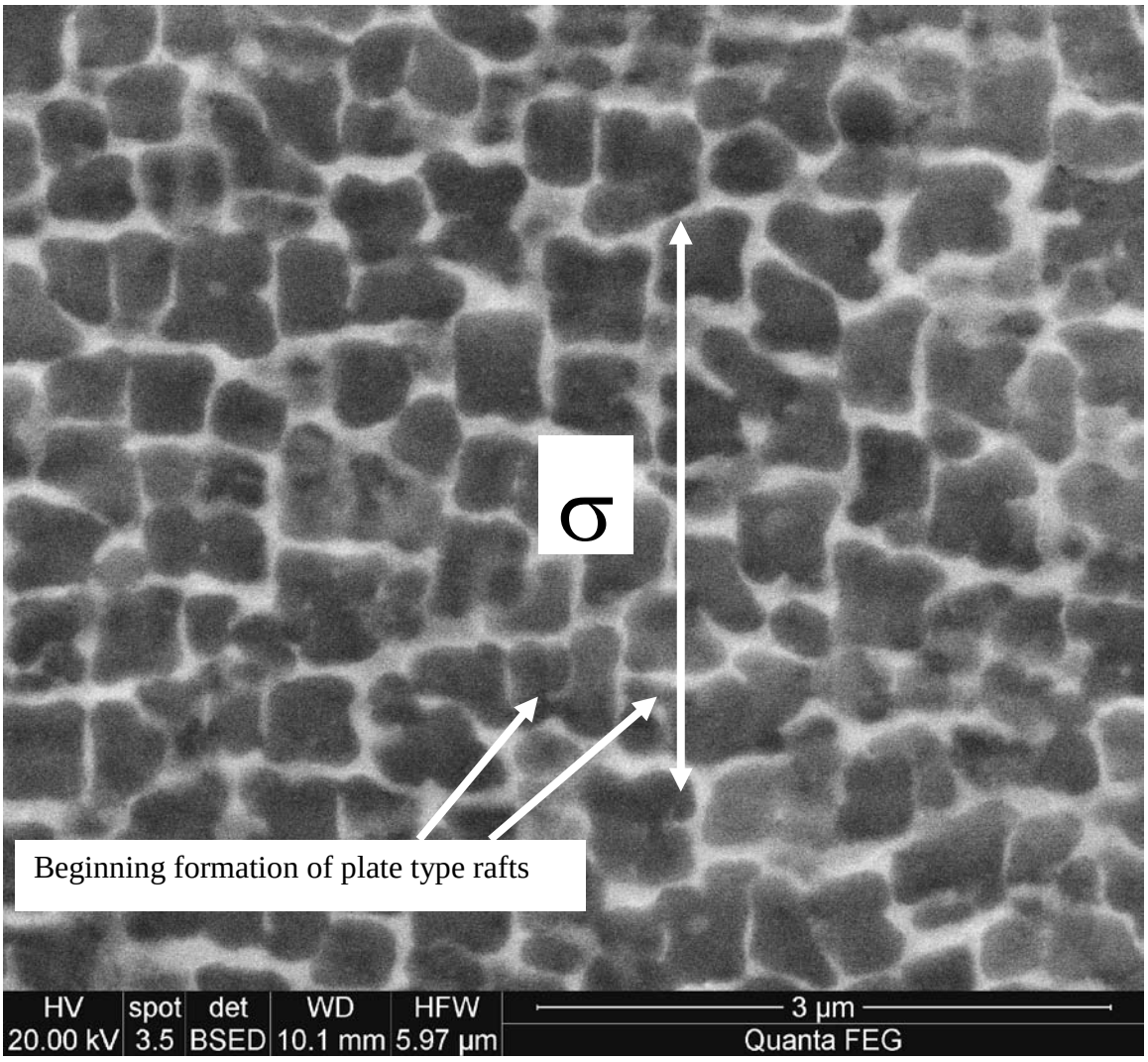

Figure 53: Test #3 Post-Test Microstructure Parallel to Applied Stress

The increase in gamma prime precipitate size is again visible on the plot of the normal distribution of the gamma prime precipitate size which is shown in Figure 54.

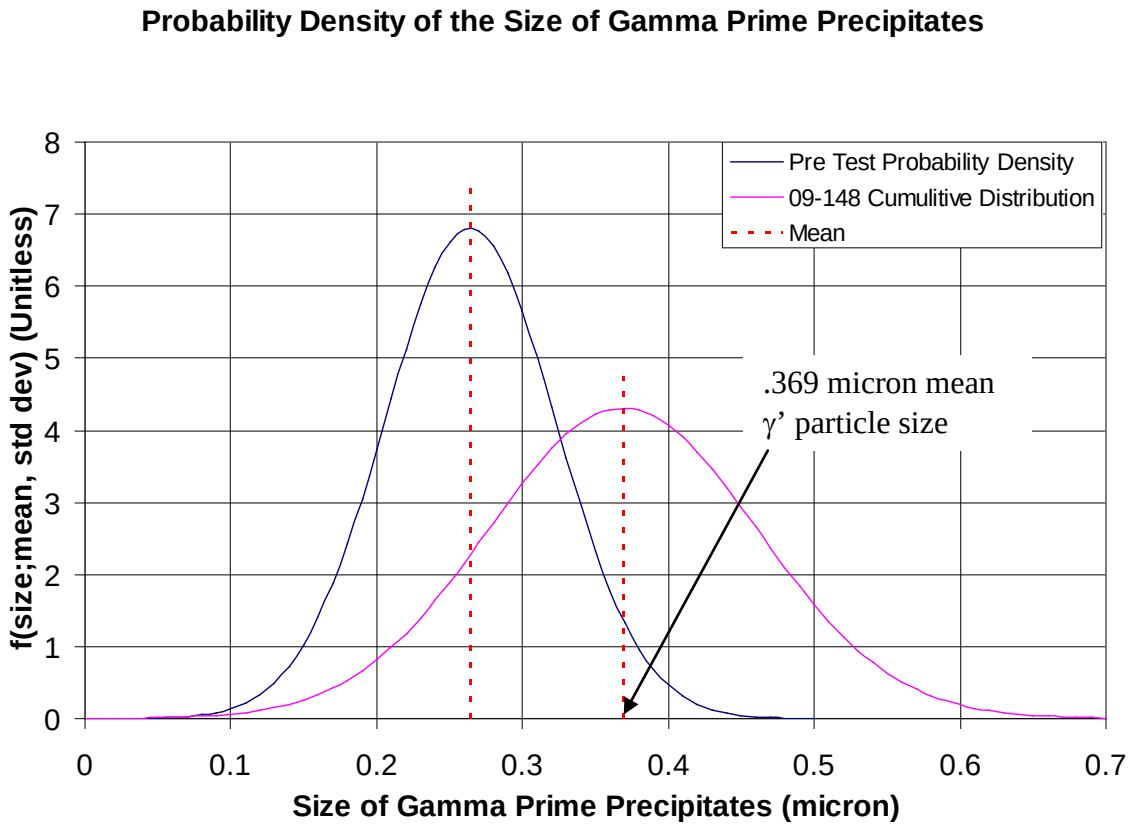

Figure 54: 09-148 Post-Test Distribution of Gamma Prime Size

5.4.4 Test #4 Creep to 2.5% Creep Strain then Fatigue to Failure Post-Test Microstructure Analysis

Figure 55 is an image perpendicular to the applied stress axis. The gamma prime precipitates are significantly larger than the pre-test microstructure and also exhibit a loss of coherency as well as a reduction in the number of aligned octocubes.

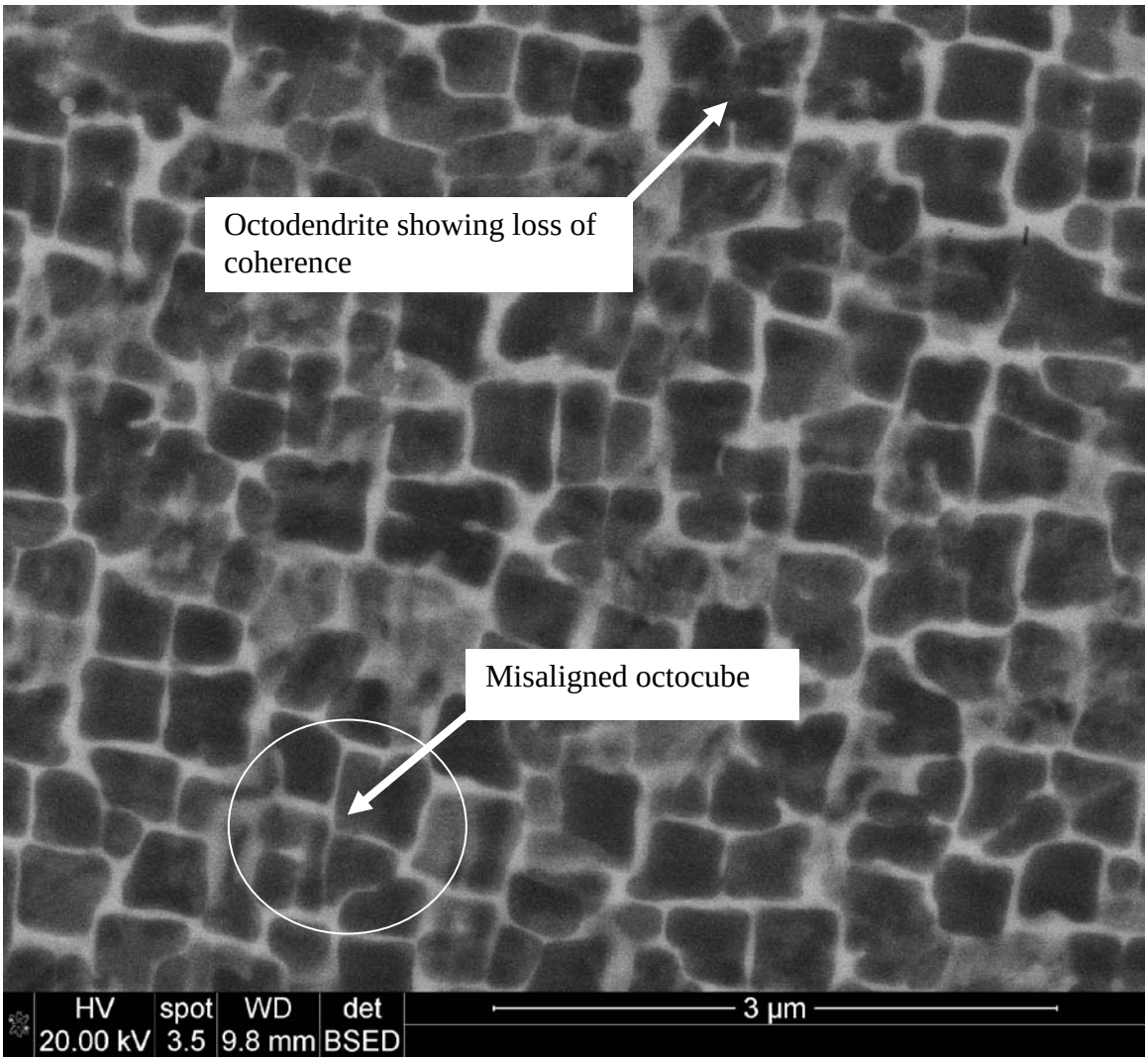

Figure 55: Test #4 Post-Test Microstructure Perpendicular to Applied Stress

Figure 56 is a view of the post-test microstructure that is parallel to the applied stress axis. The gamma prime precipitates exhibit an abundance of octodendrite structures, as well as general misalignment of the precipitates, and loss of coherency. The gamma prime precipitates do not appear to be coalescing as much as the tests that involved creep strains of 5%.

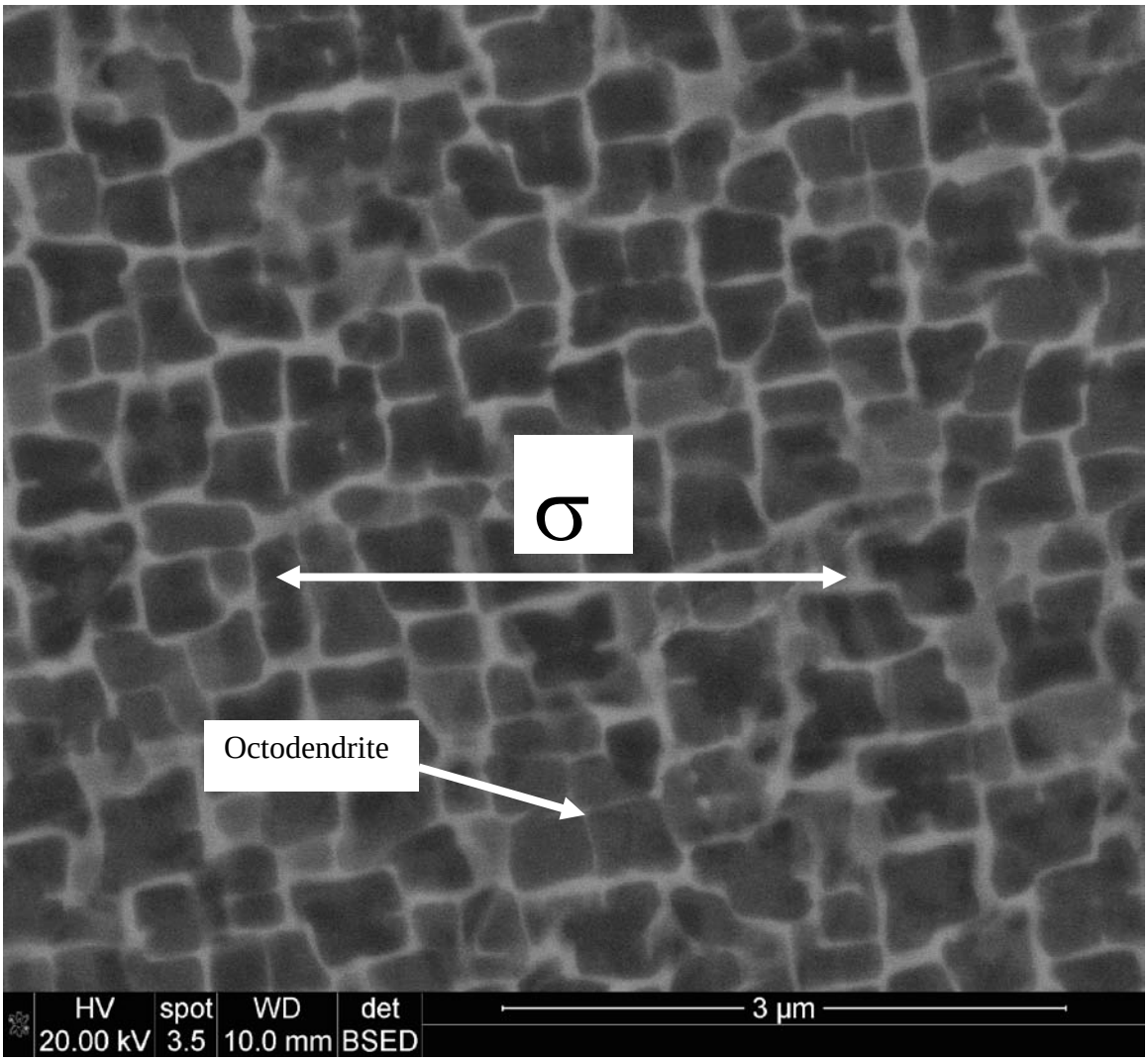

Figure 56: Test #4 Post-Test Microstructure Parallel to Applied Stress

The increase in average gamma prime precipitate size can be seen in Figure 57. This increase in gamma prime precipitate size is similar to the behavior seen in Test #2.

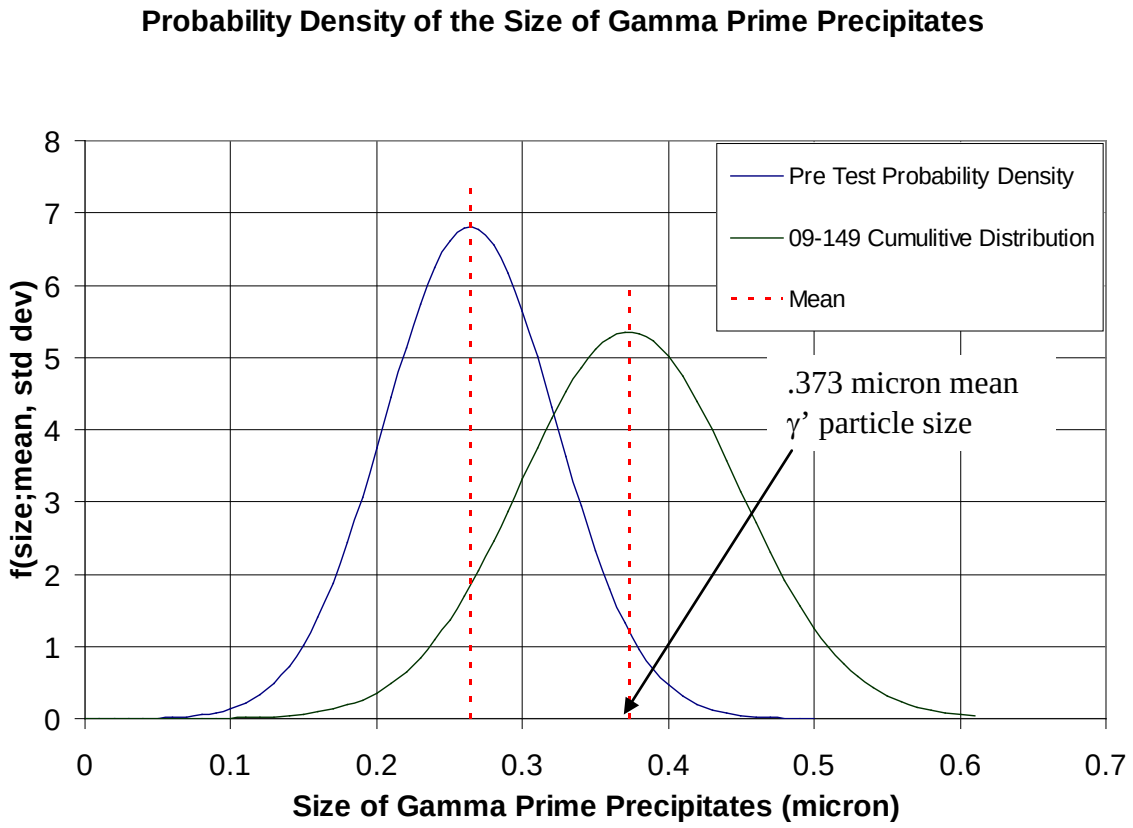

Figure 57: 09-149 Post-Test Distribution of Gamma Prime Size

Figure 58 is a comparison chart of the pre-test gamma prime precipitate size and the post-test gamma prime precipitate sizes of test numbers 1-4. It is evident that a test profile that included creep deformation results in a larger increase in gamma prime precipitate size and a larger normal distribution of gamma prime precipitate sizes.

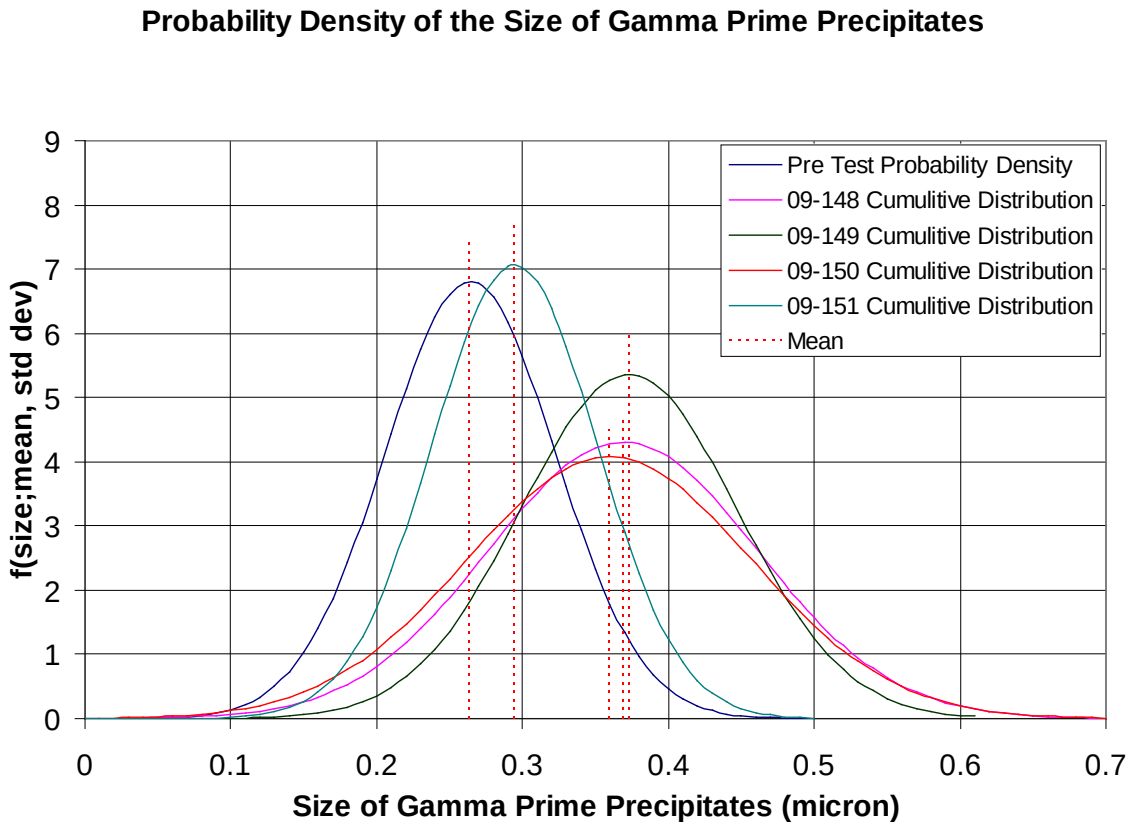

Figure 58: Comparison of Pre- and Post-Test Gamma Prime Size Distribution

5.4.5 Summary of Microstructural Observations

Each specimen displayed an increase in size of the gamma prime precipitates and the gamma channels in between the precipitates, with damage being apparent in the gamma prime precipitates that showed changes in shape as well as an increase in size. Test #3, fatigue to ~.5N_f then creep to 5% creep strain showed the most obvious shape changes in the gamma prime precipitates, indicating a large amount of damage. Test #3 also displayed the beginning stages of gamma prime plate type rafts being formed in the material. These results show that there was damage caused by prior fatigue loading, and

even though Test #3 took longer to reach 5% creep strain than Test #2, the post-test microstructure shows more damage in the specimen from Test #3. This gives support to the theory that the specimen from Test #3 would have ruptured before the specimen from Test #2. Test #4 showed post-test microstructure that was similar to the fatigue only microstructure of Test #1. While not conclusive, this seems to indicate that the prior creep strain to 2.5% did not cause large amounts of damage to the microstructure.

5.5 High Temperature Aging Effects

Not all of the size increase of the gamma prime precipitates can be attributed to fatigue or creep damage processes. Additionally, the reduction of the amount of primary creep that was seen in Test #3 cannot all be attributed to prior fatigue loading. Recent research by Wilson and Fuchs involving the effect of aging of PWA1484 at 871°C produced interesting results about gamma prime evolution during high temperature aging [22]. They found that aging PWA1484 for 32 hours at a temperature of 871°C resulted in a significant decrease of primary creep strain during creep. Wilson and Fuchs stated that a decrease in the coherency of the gamma prime precipitates was one of the causes for the decrease in primary creep strain [22]. A decrease in coherency of the gamma prime precipitates resulted in it being more difficult for dislocations to shear the gamma prime precipitates resulting in shorter glide paths for the dislocations before they interact with other dislocations [22]. This corresponds well to the difference in the primary creep strains displayed by the A and Z slabs of material, with the A slab having much lower levels of primary creep strain as compared to the Z slab which had .3% and 3.25%

primary creep strains respectively. A second reason put forward by Wilson and Fuchs was that the coarsening of the gamma prime precipitates during high temperature aging resulted in wider gamma channels between the gamma prime precipitates. This would make it more energetically favorable for the dislocations to travel through the matrix as opposed to shearing the gamma prime precipitates [22]. This can also be seen in the pre-test microstructure of the A and Z slabs with the A slab having wider gamma channels between the gamma prime precipitates.

5.6 Numerical Data Analysis

In order to test the possibility of a linear summation of prior creep damage to fatigue cycling and prior fatigue damage to creep deformation to 5% creep strain, the model proposed by Wright et al. was utilized as discussed in Chapter Two [12]. This research did not perform enough testing at different stress levels and temperatures to develop a new model to describe creep and fatigue interaction. Instead, we will attempt to fit our data into this existing model and attempt to gain insights of when the prior loading condition of the material will cause changes in the performance that cause the model to be inadequate to describe our results. Damage terms were calculated for each test using Equations (33-44) from Chapter Two and the results are shown in Tables 4 and 5.

Table 4: Damage Calculations for Testing to Failure

Specimen Number	Test Condition	Predicted Nf	Actual Nf	Fatigue Damage	Fatigue Rupture Damage	Creep Damage	Total Damage
09-144	Fatigue to Failure	126,214	176,824	1.40	0.13	N/A	1.53

09-149	Creep to 2.5% +Fatigue to Failure	126,214	115,251	0.91	0.09	0.01	1.01
09-151	Fatigue to Failure	126,214	90,076	0.71	0.06	N/A	0.78

By looking at Table 4 we can see that a combined Walker fatigue and Larsen-Miller rupture model reasonably represents two of the tests, but under predicts the cycles to failure of specimen number 09-144. This under prediction is the result of scatter in the fatigue data used to solve for the power law constants in Equation (38). One test is not statistically significant, but these experiments seem to indicate that prior creep deformation at or below 2.5% creep strain does not have a large impact on the fatigue behavior and creep-fatigue interaction during fatigue loading at these test conditions can be represented well with a linear damage summation because of how small a percentage of damage that is caused by creep during fully reversed loading conditions. The damage predictions for the specimens whose end state was 5% creep strain is represented in Table 5. Because of the large amount of primary creep observed in specimens from the Z175T plate of material, the predicted time to 5% creep strain was base lined to be the time to 5% creep strain of specimen 09-150. The damage terms could then be calculated in the same manner as described in equations (41-44).

Table 5: Damage Calculations for Tests Ending in 5% Creep

Specimen Number	Test Condition	Predicted T5% (hrs)	Actual Time (hrs)	Fatigue Damage	Fatigue Rupture Damage	Creep Damage	Total Damage
09-148	Fatigue to .5Nf + Creep to 5%	38.20	72.50	0.70	0.14	1.90	2.74
09-150	Creep to 5% Creep Strain	N/A	38.20	N/A	N/A	N/A	N/A
09-152	Fatigue to .25Nf + Creep to 5%	38.20	69.68	0.35	0.07	1.82	2.25

Examining these calculations we can see that a linear summation of damage does not represent fatigue then creep loading scenarios very accurately. There are several reasons for this. The most apparent reason is the change in the amount of primary creep that occurs as a result of prior fatigue loading. This reduction of primary creep is not accounted for in these damage summations, and since the secondary creep rate is not affected by prior fatigue loading, the time to 5% creep strain is changed significantly. The second reason is the effect of high temperature aging that has been shown to cause a reduction in the amount of primary creep.

5.7 Summary

For the temperature and stress regime in which primary creep is a factor for PWA1484, prior fatigue loading results in lower primary creep, but also does damage to the material and will cause tertiary behavior to appear earlier during creep loading of PWA1484. This damage that is done by the prior fatigue loading will cause the gamma prime microstructure to lose coherence more rapidly and results in the beginning of formation of plate type rafts in the gamma prime microstructure during subsequent creep loading.

Prior creep deformation to levels at or below 2.5% creep strain did not have a large effect on the fatigue behavior of these experiments. The modulus of the material was lowered after prior creep deformation, but it is believed that this was a result of a change in the crystallographic orientation of the specimen during creep that brought the specimen closer to the <001> plane, thus lowering the elastic modulus. During the subsequent fatigue loading, the specimen outperformed one of the specimens that were

tested in fatigue only to failure. One of the reasons for this result could be that the specimen from Test #4 was still in the primary creep region when it reached 2.5% creep strain. From this we know that dislocations are the dominant factor in deformation and damage mechanisms do not yet play a major role. This resulted in average fatigue performance of the specimen in Test #4. Additionally, the post-test microstructure of Test #4 was very similar to the fatigue only post-test microstructure of Test #1. This indicates a fatigue dominated damage process. The effects of high temperature aging were also present during testing, resulting in a loss of coherence of the gamma prime precipitates and most likely contributing to the reduction in primary creep during Test #3 [22]. Further testing needs to be performed to distinguish the reduction in primary creep that occurs as a result of prior fatigue from the reduction in primary creep that occurs as a result of high temperature aging.

VI. Conclusions and Recommendations

6.1 Chapter Overview

This Chapter will discuss the conclusions from this research and suggest means of furthering research on the topic of creep and fatigue interaction of PWA1484.

6.2 Conclusions of Research

1.) Prior fatigue affects the future creep performance of PWA1484.
    a. A reduction in primary creep was observed as a result of prior fatigue cycling at 871°C and a max stress of 517MPa.
    b. The reduction in primary creep was proportional to the number of prior fatigue cycles with ~.5N_f cycles producing a greater reduction in primary creep than ~.25N_f.
    c. Prior fatigue cycling did not affect the secondary strain rate of PWA1484 during this research regardless of the number of prior fatigue cycles applied to the specimen.
2.) The benefits of a reduction in primary creep that is caused by prior fatigue loading is offset at least to some degree by an earlier transition of the creep behavior to the tertiary creep regime.
    a. Prior fatigue cycling to .5N_f resulted in the onset of tertiary creep at 3% creep strain. The specimen that was tested in creep only displayed a secondary creep behavior up to 5%.
    b. Earlier tertiary creep behavior would most likely result in a reduction in the creep rupture life of the specimen.

c. Prior fatigue cycling to $.25N_f$ resulted in the onset of tertiary creep at 4% creep strain.
d. The onset of tertiary creep behavior indicates that a specimen cycled at elastic stresses develops microstructural damage that contributes to an earlier transition to a damage dominant tertiary creep regime.
e. Because prior fatigue changes the primary and tertiary creep behavior of the specimen, a linear summation of fatigue and creep damage that is based on a power law relationship for fatigue damage and Larsen-Miller estimations of creep performance to 5% creep strain does not give a good representation of creep life to 5% creep.
f. A model that relates prior fatigue cycling to primary creep and also models the damage done by fatigue cycling that can be used to predict when tertiary creep will begin will be required to represent this behavior.

3.) Prior creep to creep strains at or below 2.5% creep strain had very little effect on the fatigue performance of PWA1484 in this research.
    a. At 871°C and 517MPa, the specimens of PWA1484 used in this research were still in the primary creep regime at 2.5% creep strain and mobile dislocations are the main factor in creep deformation.
    b. Prior creep deformation at or below 2.5% causes rupture damage that is small and can be added to the subsequent fatigue damage linearly.

4.) Pre-test gamma prime precipitate size and gamma channel width may have an effect on the primary creep behavior of PWA1484.

    a. Creep tests performed on specimens from the A2LPT slab of material displayed a relatively small region of primary creep of .5% as compared to the 3.5% primary creep strain behavior exhibited by the creep specimen from the Z175T slab of material.

    b. Pre-test microstructural images of the two slabs of material showed that the A2LPT microstructure had gamma prime particles that were nominally .34 microns. The Z175T slab microstructure was made up of smaller .26 micron particles with narrow gamma matrix channels in between the precipitates.

5.) High temperature aging could be another factor that has an effect on the amount of primary creep and the morphology of the gamma prime precipitates in the microstructure of PWA1484.

    a. High temperature aging also occurred during fatigue cycling of testing that included fatigue followed by creep. The post-test microstructure included larger gamma prime precipitates that were less coherent than the pre-test microstructure. Post-test microstructural measurements revealed an increase in the nominal area of the gamma prime precipitates.

    b. Some of the reduction in primary creep could have been due to high temperature aging as demonstrated in previous research [22].

6.3 Recommendations for Future Research

Future research should focus on new ways to describe fatigue and creep interaction PWA1484 using thermodynamic methods such as internal energy and work. This will be in line with the current creep model for PWA1484 as developed by Seetharaman and Staroselsky at Pratt and Whitney. If the reduction in the amount of primary creep, or the changes in the coherency of the gamma prime precipitates can be described through work done on the material or a description of the internal energy change of the material, this could be integrated into the existing PWA1484 models. High temperature aging effects should also be given additional consideration. One method would be to expose PWA1484 to varying amounts of time at 871°C, and then perform creep tests to collect data on the primary creep behavior of the aged specimens. This would build on the work already begun by Wilson and Fuchs [22]. One final area that may help to get a more pure representation of the effect that prior fatigue loading has on PWA1484 is to perform the same style of testing as was performed in this research, but use different stress levels and build an archive of testing data from multi-part tests that could be used to develop higher fidelity models.

6.4 Summary

This testing has only scratched the surface of the research that needs to be done in this area. The high cost of these materials and the constant effort to become more efficient demands that the modeling of the behavior of these materials become more accurate so that the maximum safe life can be utilized from these components.

Knowledge of microstructural behavior, as well as test data will be two keys to making this possible.

Bibliography

1. Reed, Roger C. *The Superalloys: Fundamentals and Applications.* New York: Cambridge University Press, 2006.

2. Dowling, Norman E. *Mechanical Behavior of Materials.* New Jersey: Prentice-Hall Inc., 1999.

3. Cetel, A.D. and Duhl, D.N. "Second-Generation Nickel-Base Single Crystal Superalloy," *Superalloys 1988,* The Metallurgical Society, 235-244 (1988).

4. Nathal, M.V. and Ebert, L.J. "Gamma Prime Shape Changes During Creep of a Nickel-Base Superalloy," *Scripta METALLURGICA,* 17: 1151-1154 (1983).

5. Mughrabi, Hael. "Gamma/Gamma Prime Rafting and its Effect on the Creep and Fatigue Behavior of Monocrystalline Superalloys," *The Johannes Weertman Symposium,* The Minerals, Metals, and Materials Society, 267-278 (1996).

6. Eshelby, J.D."Elastic Inclusions and Inhomogeneities," *Progress in Solid Mechanics Vol II:* 89-139 (1961).

7. Volkl, R., Glatzel, U., and Feller-Kniepmeier, M. "Measurement of the Lattice Misfit in the Single Crystal Nickel Bases Superalloys CMSX-4, SRR99, and SC16 by Convergent Beam Electron Diffraction," *Acta Mater,* Vol. 46, No. 12: 4395-4404 (1998).

8. MacLachlan, D.W. and Knowles, D.M. "Creep-Behavior Modeling of the Single Crystal Superalloy CMSX-4," *Metallurgical and Materials Transactions A,* 31A: 1401-1411 (2000).

9. Ott, M. and Mughrabi, H. "Dependence of the High Temperature Low Cycle Fatigue Behavior of the Monocrystalline Nickel Based Superalloys CMSX-4 and CMSX-6 on the Gamma/Gamma Prime Morphology," *Materials Science and Engineering,* A272: 24-30 (1999).

10. Sakaguchi, M. and Okazaki, M. "Fatigue Life Evaluation of a Single Crystal Ni-Base Superalloy, Accompanying with Change of Microstructure Morphology," *International Journal of Fatigue,* 29: 1959-1965 (2007).

11. Shames, Irving H. and Cozzarelli, Francis A. Elastic and Inelastic Stress Analysis. Taylor and Francis Group, Philadelphia, Pa. 1997.

12. Wright, P.K., Jain, M., and Cameron, D. “High Cycle Fatigue in a Single Crystal Superalloy: Time Dependence at Elevated Temperature,” *Superalloys 2004: 657-666 (2004).*

13. Smith, William F. Principles of Materials Science and Engineering. The McGraw-Hill Companies, Inc, New York, Ny. 1999.

14. Gullickson, J., Needleman, A., Staroselsky, A., Cassenti, B. “Boundary Damage Effects on the Evolution of Creep Strain,” *Modeling and Simulation in Materials Science and Engineering: 1-14 (2008).*

15. Ko, H.S., Paik, K.W., Park, L.J., Kim, Y.G., Tundermann, J.H. “Influence of Rhenium on the Microstructures and Mechanical Properties of a Mechanically Alloyed, Oxide Dispersion Strengthened, Nickel-Base Superalloy,” *Journal of Materials Science 33: 3361-3370 (1998).*

16. Image of Pratt and Whitney F-100 Engine. http://www.pw.utc.com/StaticFiles. 2 March 2009.

17. Campbell, F.C. Manufacturing Technology for Aerospace Structural Materials. Elsevier Inc., San Diego, CA. 2006.

18. Nathal, M.V. “Effect of Initial Gamma Prime Size on the Elevated Temperature Creep Properties of Single Crystal Nickel Base Superalloys,” *Metallurgical Transactions A 18A: 1961-1970 (1987).*

19. Chaboche, J.L., and Gallerneau, F. “An Overview of the Damage Approach of Durability Modeling at Elevated Temperature,” *Fatigue and Fracture of Engineering Materials and Structures 24: 405-418 (2001).*

20. Chen, L., Jiang, J., Fan, Z., Chen, X., Yang, T. “A New Model for Life Prediction of Fatigue-Creep Interaction,” *International Journal of Fatigue 29: 615-619 (2006).*

21. Grosdidier, T., Hazotte, A., and Simon, A. “Precipitation and Dissolution Processes in Gamma/Gamma’ Single Crystal Nickel-Based Superalloys,” *Materials Science and Engineering A256: 183-196 (1998).*

22. Wilson, B.C. and Fuchs, G.E. “The Effect of Composition, Misfit, and Heat Treatment on the Primary Creep Behavior of Single Crystal Nickel Base Superalloys PWA 1480 and PWA1484,” *Superalloys 2008: 149-158 (2008).*

23. Air Force Research Laboratory. *Advanced High Cycle Fatigue Life Assurance Methodologies.* Materials and Manufacturing Directorate: Air Force Research Laboratory, WPAFB, OH. 2004.

24. MacKay, R.A. and Ebert, L.J. “The Development of γ-γ’ Lamellar Structures in a Nickel-Base Superalloy During Elevated Temperature Mechanical Testing,” *Metallurgical Transactions A 16A: 1969-1982 (1985).*

25. Private Communications with Dr. Bob Wright from AFRL Propulsion Directorate. January 2008.

26. Seetharaman, V. Unpublished Pratt and Whitney Test Data. February 2009.

REPORT DOCUMENTATION PAGE

Form Approved
OMB No. 074-0188

1. REPORT DATE *(DD-MM-YYYY)*	**2. REPORT TYPE**	**3. DATES COVERED** *(From – To)*
26-03-2009	Master's Thesis	April 2008 – March 2009

4. TITLE AND SUBTITLE

Creep and Fatigue Interaction Characteristics of PWA1484

5a. CONTRACT NUMBER

5b. GRANT NUMBER

5c. PROGRAM ELEMENT NUMBER

6. AUTHOR(S)

Pierce, Christian J., Captain, USAF

5d. PROJECT NUMBER

5e. TASK NUMBER

5f. WORK UNIT NUMBER

7. PERFORMING ORGANIZATION NAMES(S) AND ADDRESS(S)

Air Force Institute of Technology
Graduate School of Engineering and Management (AFIT/EN)
2950 Hobson Way, Building 640
WPAFB OH 45433-8865

8. PERFORMING ORGANIZATION REPORT NUMBER

AFIT/GMS/ENY/09-M02

9. SPONSORING/MONITORING AGENCY NAME(S) AND ADDRESS(ES)

Dr. Tommy George
AFRL Turbine Engine Fatigue Facility (AFRL/RZTS)
Building 252, Room 20
WPAFB, OH 45433-7251

10. SPONSOR/MONITOR'S ACRONYM(S)

11. SPONSOR/MONITOR'S REPORT NUMBER(S)

12. DISTRIBUTION/AVAILABILITY STATEMENT

APPROVED FOR PUBLIC RELEASE; DISTRIBUTION UNLIMITED.

13. SUPPLEMENTARY NOTES

14. ABSTRACT

One of the main methods for predicting the service life of jet engine turbine blades is through creep analysis. A sample of the turbine blade material will be mechanically tested to characterize its creep performance. This characterization will be used to determine safe operating conditions for the material. While methods for modeling creep behavior are generally well developed, this constant load creep testing does not fully represent the loading conditions present in a jet engine due to cyclic loading caused by the mission profile and throttle movements. As the industry seeks to become more accurate in physics based modeling of materials that are used in turbine blades, incorporation of these cyclic loads into the characterization of turbine blade materials is needed. It will be important to understand what effect pre-existing creep will have on fatigue life and what effect pre-existing fatigue loading will have on creep life. This research gives microstructural observations as well as data analysis of samples of PWA1484 tested at 871°C in creep-fatigue environment. This research resulted in the conclusion that prior fatigue cycling results in a non-linear reduction in the amount of primary creep, and an earlier transition to tertiary creep in PWA1484.

15. SUBJECT TERMS

Single Crystal Superalloy, High Cycle Fatigue, Creep

16. SECURITY CLASSIFICATION OF:			**17. LIMITATION OF ABSTRACT**	**18. NUMBER OF PAGES**	**19a. NAME OF RESPONSIBLE PERSON**
a. REPORT	**b. ABSTRACT**	**c. THIS PAGE**			Dr. Anthony Palazotto, AFIT/ENY
U	**U**	**U**	**UU**	121	**19b. TELEPHONE NUMBER** *(Include area code)* (937) 255-3636, ext 4599 (emailname@afit.edu)

Standard Form 298 (Rev. 8-98)
Prescribed by ANSI Std. Z39-18